UNIVERSITÀ DEGLI STUDI DI PALERMO

Dottorato di Ricerca in Energia e Tecnologie della Informazione
Dipartimento di Ingegneria
SSD: ING-IND-33 Sistemi Elettrici per l´Energia

GRID STABILITY IMPROVEMENT BY RES-BASED GENERATORS AND BATTERY ENERGY STORAGE SYSTEMS IN SMALL ISLANDS

IL DOTTORE
MILAGROS AMPARO NAVARRO NAVIA

IL COORDINATORE
PROF. MAURIZIO CELLURA

IL TUTOR
PROF. SALVATORE FAVUZZA

IL CO-TUTOR
PROF. GAETANO ZIZZO

CICLO XXXIII
ANNO CONSEGUIMENTO TITOLO 2021

Dedicated to …

My parents, Amparo Navia and Ancizar Navarro

My husband, Ettore Caruso

My brother, Cristian Navarro Navia

GRID STABILITY IMPROVEMENT BY RES-BASED GENERATORS AND BATTERY ENERGY STORAGE SYSTEMS IN SMALL ISLANDS
MILAGROS AMPARO NAVARRO NAVIA
Engineering Department
University of Palermo

Abstract

The integration of Renewable Energy Sources (RES) with power electronics interface to the grid, without the back-up of rotating inertia, endangers frequency stability. This issue becomes particularly critical in isolated power systems, like those of small islands not supplied by the main grid, in the case of high shares of production from unpredictable renewables such as photovoltaic and wind sources. Consequently, to preserve the security and the reliability of these systems, it is necessary to adopt new frequency adjustments mechanisms. In this context, the thesis investigates the transition toward an economically and technically feasible generating system based on RES, to achieve specific decarbonisation targets in two Italian small islands, proposing solutions for preserving grid stability.

The optimal energy mix characterised by the lowest Levelized Cost of Energy is evaluated for both Lampedusa and Pantelleria islands (two Italian islands in the Mediterranean Sea), and then a frequency stability analysis is performed showing that, in some operating conditions, the island power systems are no more stable due to the inertia reduction caused by RES.

Two solutions are hence proposed: the use of suitable Voltage Source Converters (VSC) for RES interface based on a Virtual Synchronous Machine (VSM) coupled to a traditional Cascaded Current Control (CCC) and the use of Battery Energy Storage System (BESS) able to provide virtual inertia (VI) response.

The first aim of the thesis is to show how much important is to consider stability issues in the decarbonisation process of small islands. The second aim is to propose feasible solutions for facing this issue.

The thesis's main contribution is the novelty of the proposed study, based on real data provided by the two small island utilities and analysing real scenarios of RES penetration in the two grids. The study results provide precious information for fostering the transition of the two islands towards green smart grid structures.

Keywords

Renewable Energy; Grid Stability; Mediterranean Sea; Sea Wave; LCoE; Inertial Response; Voltage Source Converters; Virtual Synchronous Machine; Battery Energy Storage Systems.

Acknowledgements

I would like to thank the following people, without whom I would not have been able to complete this research.

My sincere gratitude goes to my primary supervisor Prof. Salvatore Favuzza, who encouraged me. I would also like to thank my supervisor Prof. Gaetano Zizzo who patiently guided me and taught me everything I know about this research. Also, I would like to thank my supervisor during the period abroad Prof. Massimo Bongiorno and Prof. Eleonora Riva Sanseverino for her unconditional support.

I would also like to thank the help provided by the technical, administrative, support staff in the Engineering Department of the Universitá degli Study di Palermo and colleagues at the room Francesco Montana, Giuseppe Sciumé, Enrico Telaretti and Rossano Musca, who have supported me for the three years of study. Also, I am grateful to Domenico Curto for supporting me and working on several projects together.

Finally, I would like to thank my in-laws, Francesca Leone and Paolo Caruso, *per avermi sostenuto nella mia permanenza a Palemo*. My parents, Amparo Navia y Alonso Navarro *que desde el comienzo del percurso me dieron fortaleza y positivismo para seguir adelante*. My brother Cristian Navarro for listening to me and giving me advice with the English language of the documents and papers that I make and my husband Ettore Caruso, for having signed up for the doctorate course, supporting me and above all for having always believed in me.

Contents

List of Figures

List of Tables

List of Acronyms

Sigle	Description
AG	Lampedusa
BESS	Battery Energy Storage System
CCC	Cascaded Current Control
CPP	Conventional Power Plant
CC	Current Control
DFIG	Doubly-Fed Induction Generator
DPC	Direct Power Control
DSO	Distribution System Operator
ENTSO-E	European Network of Transmission System Operators for Electricity
ESS	Energy Storage System
FCR	Frequency Containment Reserve
FRU	Fast Reserve Unit
FSM	Frequency Sensitive Mode
GIS	Geographic Information System
GIE	Grid Impedance Estimator
IR	Inertia Response
IRENA	International Renewable Energy Agency
LCoE	Levelized Cost of Electricity
LFSM-U	Limited Frequency Sensitive Mode-Under
LFSM-O	Limited Frequency Sensitive Mode-Over
MV	Medium Voltage
NSPL	Non-Synchronous Penetration Level
NUP	National Unique Price
PCC	Point Common Coupling
PLL	Phase-Locked Loop
PVP	Photovoltaic Panels
PFR	Primary Frequency Response
PSC	Power Synchronisation Control
RC	Reference Control
RES	Renewable Energy Source
RoCoF	Rate of Change of Frequency
RON	Italian acronym of Rete Ondametrica Nazionale
SC	Swing Control
SFR	Secondary Frequency Response
SG	Synchronous Generator
SoC	State of Charge
SPC	Synchronous Power Controller
SCR	Short Circuit Ratio
TFR	Tertiary Frequency Response
TLCC	Total Life Cycle Cost
TP	Pantelleria
TSO	Transmission System Operator
VI	Virtual Inertia
VSC	Voltage Source Converter
VSM	Virtual Synchronous Machine
VISMA	Virtual Synchronous Machine
WEC	Wave Energy Converter

Chapter 1

Premise to the work

1.1. Introduction

In the race to improve world energy sustainability, the European Union (EU) promotes the installation of new distributed generating systems supplied by Renewable Energy Sources (RES), introducing incentives to simplify their spreading and diffusion [1]. Thanks to RES, reduced pollutants and greenhouse gas emissions are obtained due to both a lower use of fossil fuels and better management of local natural resources [2], [3].

A recent IRENA report shows that, in less than 20 years, the installed power from RES worldwide is practically tripled, from 753.95 GW in 2000 to 2350.76 GW in 2018. RES are concentrated mainly in Asia (1023.5 GW, 43.54%), Europe (536.4 GW, 22.82%) and North America (366.5 GW, 15.59%) [4]. However, huge investments are still required for a significant energy transition from fossil fuels to RES [5].

Despite the spreading of RES around the world, several small islands not supplied by the main grid are still totally or almost totally supplied by local power plants based on fossil fuels [6]-[7]. Considering the Small Islands Developing States (SIDS), the electricity demand to supply all these communities is estimated equal to 52690 GWh/year and currently is mainly covered by diesel generators [8].

In addition, small islands show several peculiarities in the energy sector [9], [10]:

- the presence of electrical grids not connected to the mainland;
- high seasonal variation in inhabitants (especially in touristic destinations);
- annual growth of energy demand (especially in developing countries);
- limited utilisation of RES (especially for the preservation of the landscape);
- high fuel cost due to the need to import it from the mainland or far foreign Countries;
- limited freshwater reserves, so desalination plants sometimes are required [11].

To increase the energy independence from fossil fuels in small island, several projects have been promoted, proposing specific energy mixes according to local availabilities, such as Samsø (Denmark) [12], Faroe Islands [13], Cozumel Island (Mexico) [14], Canary Islands (Spain) [15], [16], Azores (Portugal) [17], [18], Maldives [7] and Reunion Island (France) [19].

The literature exploring RES penetration in small islands is mainly focused on commercial technologies such as wind plants and photovoltaic (PV) systems. E.g., Notton reported statistics on the electricity generation in several French islands (located in different parts of the world), considering installing power plants supplied by wind and solar sources [20].

Kougias et al. investigated a potential energy mix based on solar, wind, fossil fuel and a battery storage system to supply several small Greek islands (Rhodes, Lesvos, Chios, Karpathos and Patmos) in the Aegean Sea, close to Turkey [21].

Geothermal, hydropower and biomass are sometimes considered to improve the energy sector's sustainability [22].

Sea wave energy potential has also been investigated in the last decade, thanks to several peculiarities, such as the great regularity and huge availability, especially in small islands where the energy demand is limited, e.g., in [23], the energy production and the performance characteristics of three wave energy converters are estimated for two Italian locations. In [24], the authors estimate wave energy potential in Sicily (Italy). In [25], a high-resolution wave atlas for nearshore energy production at the Aegean Sea is provided, while in [26] the wave resource around Menorca island (Spain) is assessed. Several solutions have been proposed, but still, no consolidated technologies are commercially available. In [9], [27] four-wave converters (Wave Star, Oyster, Wave Dragon and Archimedes Wave Swing) are compared, assuming the Sicilian coast as a case study while in [9], [27] two Pelamis farm configurations are considered in the Portuguese coast.

To improve the energy sustainability of about 20 Italian small islands, the Italian Government has recently issued two decrees promoting the introduction of RES and realising projects able to affect the final uses' energy efficiency. In detail, the Italian Ministry of Economic Development issued Decree February 14, 2017, fixing the amount of RES devices to install in 20 small islands by December 31, 2020 [28]. The Decree establishes a fund of 15 M€ for the realisation of projects devoted at lowering the primary energy consumption of final users in small islands [29]. The energy goals are modulated according to annual electricity production.

In this context, various methods have been presented in the literature to find an optimal energy mix and reach the objective of decarbonizing small islands. As, e.g., in [30], the authors consider five indicators for assessing renewable energy integration in the Beijing-Tianjin-Hebei Region. The author believes the importance of flexible resources for integrating renewables and evaluating both technical and economic indicators. In [31] a GIS-based approach is presented, based on the elaboration of queried maps and tables with percentages of electricity consumptions covered by local RES, identifying the most critical and suitable areas for installing new RES plants in Lazio. In [18], Pico and Faial islands' RES potential is characterised by modelling some scenarios with EnergyPLAN.

In this thesis, to achieve the Italian Government's goal for small islands, a method for finding the optimal renewable energy mix, composed of solar, wind and sea wave energy is applied. Commercial technologies are considered to exploit solar and wind sources, while innovative technology is presented in a sea wave case. The method is applied to Lampedusa and Pantelleria islands, located in the Mediterranean Sea, and considers the stability issue.

In this thesis, a complete approach is adopted concerning the other methods, considering three phases. At first, a preliminary choice of the optimal energy mix to install, based on the Levelized Cost of Electricity (LCoE) calculation, is done. Subsequently, a dynamic analysis in the presence of the identified energy mix in various operating conditions for assessing the technical feasibility of the installation of RES plants from the point of view of grid security is performed. Finally, some solutions based on new control methods for static converters interfacing RES and Battery Energy Storage Systems (BESS) to the grid are proposed.

Indeed, the analyses of RES penetration to Pantelleria and Lampedusa islands, that are presented in this thesis show clearly how the electricity production by RES requires to face new challenges in smart grids related to remote control, stability, and power quality. As an example of how RES interfaced to the grid by static converter poses new challenges, it is possible to refer to a technical report recently issued by IEEE discussing two new forms of stability, including converter-driven stability resonance stability [32].

For a better understanding of what happens in the presence of high shares of RES in weak isolated systems, it is necessary to consider the role of Conventional Power Plants (CPP) with

Synchronous Generators (SGs) in the current power system architecture [33]. SGs can generate reactive power for voltage regulation [34] and have overload capacity but, in particular, SGs provide rotational inertia, which is indicative of kinetic energy stored in the machines used during a frequency transient [35],[36], [37].

Regarding this last point, it is worth underlying that all Transmission System Operators (TSO) worldwide indicate the disappearance of rotational inertia as a significant element able to impact angle stability. By reducing the power system inertia, the rotors of electrical machines accelerate faster and reach the limit of angular stability faster, generating more rapid dynamics. Another effect of low Inertial Response (IR) is that the frequency produces more significant oscillation, i.e., the power system is more sensitive to disturbances, presenting a reduction in damping. Still, the Rate of Change of Frequency (RoCoF) increases [38] and so the maximum frequency deviation (to the frequency nadir). From the operational point of view, the consequences of reducing inertia with increasing nadir produce problems in frequency safety, causing the activation of the emergency frequency protection mechanism as under-frequency load shedding [39], [40], [41].

Many industrialised countries have defined rotational inertia problems since mid-2008 and have tried to monitor system inertia. From the operational point of view to know the minimum inertia, there are several techniques. Table 1.1 shows a summary of the different mechanisms for estimating the IR.

Table 1.1. IR Methods.

Method	Input Data			
	EMS	f	Ap	Application
Continuos signal - Ambient [42]	-	x	x	In Retrospect
Continuos signal - Stimulated	-	x	-	In Retrospect
Event-driven - System [35]	-	x	-	Real-time
Event-driven - Regional [35]	-	x	x	Real-time
Unit commitment [36], [43]	x	-	-	Real-time

To increase system inertia, it is necessary to have recourse to new mechanisms as virtual inertia from static converters. In order to preserve their stability during disturbances, grids must include RES generators using smart converters that must measure, process, and emit a response that imitates that of SG.

For doing this, different control strategies have been proposed in the literature, for both grid following and grid forming grid-connected converters [44].

The traditional grid follower converters are used mainly in PV inverters. They are followers because they need a grid synchronization reference signal coming from a Phase Locked Loop (PLL) [45], [46]. Their control, classically, is a Cascaded Current Control (CCC) [47], [48], [49], [50].

On the other hand, the concept changes when using the grid forming converters able to generate voltage and frequency signals without using a PLL. The literature on-grid forming converters is extensive [51] because they use different control schemes e.g., Virtual Synchronous Machine (VSM) [52], Power Synchronization Control (PSC) [53] and Direct Power Control (DPC) [54], [55]. Table 1.2 summarizes the main methods for the emulation of the VSM.

A second strategy to increase system inertia is to include the grid suitably controlled Battery Energy Storage Systems (BESS). The BESS allows participating in the power regulation,

guaranteeing an improvement in grid stability and continuity of the island's electricity service [56].
This second strategy appears as the preferred by the owner of the distributed generators since, using BESS, it is unnecessary to maintain a power reserve for an inertial response from RES sources, that will cause a reduction in the owner’s profit.

Table 1.2. Grid Forming methods.

Grid Forming- Methods	
Synchronous generator model-based	Synchronverters [57]
	Virtual Synchronous Machine (VISMA) [58]
	Kawasaki Heavy Industries Labs Topology
Swing equation-based	Synchronous Power Controller (SPC) [59]
Frequency power response based	Virtual Synchronous Generator VSM [48]
	Droop based approach
	Virtual oscillator converter [60]

1.2. Purpose of the thesis and main contributions

In this context, this thesis has the aim to investigate the impact, in terms of frequency stability, of static converter interfaced-RES generators on small islands not supplied by the main grid and to discuss possible solutions for improving system security. The thesis presents two cases of studies related to the islands of Lampedusa and Pantelleria in the Mediterranean Sea.

The main contributions of the thesis are the following:

- an accurate estimation of the system inertia of the two islands is done using real data provided by the local utilities and considering typical summer and winter load profiles and SG schedules both in the presence and in the absence of RES. This part of the study allows to discover unsecure working condition, from the point of view of frequency stability, in the current situation and future scenarios;
- the optimal energy mix that allows achieving the decarbonization targets in the two islands while minimizing the Levelized Cost of the Investment (LCoI) is assessed and verified from the point of view of system stability, highlighting how grid issues must be considered as system constraints in such kind of problems;
- two control schemes are applied to VSC for interfacing RES to the grid and they are tested in the case of both strong and weak grids for assessing the tuning of the control parameters. The VSM structure is finally analysed coupled with CCC, and its effectiveness is demonstrated both in steady-state and during a severe fault in weak grids;
- a sizing strategy of BESS for providing virtual inertia is proposed for small islands and applied to one of the two islands under different production and imbalances hypotheses. Economical consideration of the BESS sizing is provided;
- the novelty of the proposed study based on real data provided by the two small island utilities and analyzing real RES penetration scenarios in the two grids. The study results provide precious information for fostering the transition of the two islands towards green smart grid structures.

  Finally, the thesis has been developed within the framework of various research projects involving the Engineering Department of the University of Palermo and concerning energy efficiency and RES penetration in small islands:
- collaboration agreement between the Engineering Department of the University of Palermo and ENEA, the Italian National Agency for New Technologies, Energy and

- Sustainable Economic Development: “Analisi sperimentale e numerica di tecnologie solar driven per la climatizzazione e la produzione di ACS e di sistemi ICT per il controllo e la riduzione dei carichi elettrici nelle isole minori non connesse alla RTN” (Coordinator: Prof. Marco Beccali);
- collaboration agreement between the Engineering Department of the University of Palermo and ENEA, the Italian National Agency for New Technologies, Energy and Sustainable Economic Development: Studio di fattibilità di soluzioni per l’efficientamento energetico delle Isole Minori”, Research Project 1.5 “Tecnologie, tecniche e materiali per l’efficienza energetica ed il risparmio di energia negli usi finali elettrici degli edifici nuovi ed esistenti” (Coordinator: Prof. Gaetano Zizzo);
- research project “BLORIN – BLOCKCHAIN PER LA GESTIONE DECENTRATA DELLE RINNOVABILI”, PO FESR Sicilia 2014/2020 – Action 1.1.5 “Sostegno all’avanzamento tecnologico delle imprese attraverso il finanziamento di linee pilota e azioni di validazione precoce dei prodotti e di dimostrazione su larga scala”, (Coordinator: Prof. Eleonora Riva Sanseverino).

1.3. Structure of the thesis

The thesis is organised into nine Chapters.

1. The present Chapter 1 describes the background information, motivation, and thesis contribution.
2. Chapter 2 briefly analyses frequency adjustment mechanisms and introduce the concept of RoCoF, frequency nadir, Frequency Containment Reserve (FCR) and system inertia, referring, in particular, to the Italian Grid Code for distribution systems.
3. Chapter 3 describes the generating and distribution systems of Lampedusa and Pantelleria islands, providing all data necessary for the further elaborations detail of two isolated power systems and proposing a method for evaluating system inertia based on real data.
4. Chapter 4 analyses the inertial response of the two islands in the presence of generation from RES, proposing a methodology for such an analysis and calculating in various scenarios the maximum allowed imbalance between generation and demand and the frequency nadir.
5. Chapter 5 deals with a technical and economic methodology for assessing the optimal RES mix for a small island while preserving the system stability. The methodology shows that a simple, economical evaluation of the RES mix can lead to stability issues in some cases.
6. Chapter 6 proposes suitable control strategies for allowing higher RES penetration thanks to the provision of damping and virtual inertia. Various control strategies are analysed as a function of the Short Circuit Ratio, both steady-stable and during fault conditions.
7. Chapter 7 applies the VSM+CCC control strategies to the case study of Lampedusa, assuming a severe fault in the grid and showing how this kind of control is suitable for improving system stability also in the presence of high shares of RES.
8. Chapter 8 proposes a methodology for calculating the BESS size for providing virtual inertia to the small island.
9. Finally, Chapter 9 contains the conclusion of the thesis.

1.4. List of Publications

The present section reports a list of the publications produced during the PhD.

Articles in Journals indexed by Scopus

I. D. Curto, S. Favuzza, V. Franzitta, R. Musca, M. A. Navarro Navia, G. Zizzo, “Evaluation of the optimal renewable electricity mix for Lampedusa island: The adoption of a technical and economical methodology”, Journal of Cleaner Production, vol. 263, 2020, article number 121404. ISSN: 0959-6526, DOI: 10.1016/j.jclepro.2020.121404.

Conference Proceedings indexed by Scopus

II. D. Curto, S. Favuzza, R. Musca, M. Navarro Navia, G. Zizzo, “Control Structures Implementation to Allow High Penetration of a VSC within an Isolated Power System” in the First International Conference on Electrical Energy and Power Engineering (ICEEPE 2020), 27 - 28 October 2020, Penang (Malaysia).

III. J. A. Sa'ed, D. Curto, S. Favuzza, R. Musca, M. Navarro Navia, G. Zizzo, “A Simulation Analysis of VSM Control for RES plants in a Small Mediterranean Island”, 2020 IEEE International Conference on Environment and Electrical Engineering and 2020 IEEE Industrial and Commercial Power Systems Europe (EEEIC / I&CPS Europe), 9-12 June 2020, Madrid (Spain), DOI: 10.1109/EEEIC/ICPSEurope49358.2020.9160501.

IV. S. Favuzza, M. S. Navarro Navia, R. Musca, E. Riva Sanseverino, G. Zizzo, B. Doan Van, N. Nguyen Quang. “Impact of RES Penetration on the Frequency Dynamics of the 500 kV Vietnamese Power System”, 2019 8th International Conference on Renewable Energy Research and Applications (ICRERA), 3-6 November 2019, Brasov (Romania), -DOI: 10.1109/ICRERA47325.2019.8996862

V. S. Favuzza, M. G. Ippolito, R. Musca, M. Navarro Navia, E. Riva Sanseverino, G. Zizzo, M. Bongiorno. “An Analysis of the Inertial Response of Small Isolated Power Systems in Presence of Generation from Renewable Energy Sources”, 2018 IEEE 4th International Forum on Research and Technology for Society and Industry (RTSI), pp. 1-6, 10-13 September 2018, Palermo (Italy), DOI: 10.1109/RTSI.2018.8548401.

VI. S. Favuzza, M. G. Ippolito, R. Musca, M. Navarro Navia, E. Riva Sanseverino, G. Zizzo, M. Bongiorno. “System Stability of a Small Island's Network with Different Levels of Wind Power Penetration”, 2018 IEEE 4th International Forum on Research and Technology for Society and Industry (RTSI), pp. 1-6, 10-13 September 2018, Palermo (Italy), DOI: 10.1109/RTSI.2018.8548355.

Articles submitted for consideration in Journals Indexed by Scopus under revision

VII. J. A. Sa'ed, D. Curto, S. Favuzza, R. Musca, M. Navarro Navia, G. Zizzo, “Virtual Synchronous Machine Control of RES plants in a Small Mediterranean Island”, IEEE Transactions on Industry Application (submitted on November 10, 2020).

VIII. D. Curto, S. Favuzza, V. Franzitta, M. Navarro Navia, E. Telaretti, G. Zizzo, “Grid Stability Improvement in the presence of Renewable Electricity Mix Methodology Using Synthetic Inertia by BESS – Part I”. Energy (submitted on January 15, 2020).

Articles in development

IX. D. Curto, S. Favuzza, V. Franzitta, M. Navarro Navia, E. Telaretti, G. Zizzo, “Grid Stability Improvement in the presence of Renewable Electricity Mix Methodology Using Synthetic Inertia by BESS – Part II”. Energy, Elsevier (In progress).

Chapter 2

Frequency adjustments mechanisms

2.1. Introduction

This Chapter introduces the problem of the frequency adjustments mechanisms in power system, analysing the technical requirements from the Italian Grid Codes for distribution systems [61], [62] and introducing the concept that will be used in the present thesis for assessing the stability of small islands in the presence of high shares of Renewable Energy Sources (RES) interconnected by static converters.

2.2. Grid services and frequency regulation

Active users connected to the power grid must control and operate their generators in order to provide the grid services listed in Table 2.1.

Table 2.1: Grid services, according to CEI Standard 0-16.

Reference Service	Synchronous Generators (SG)	Conventional asynchronous generator	Full converter Wind plant	Wind Doubly Fed Induction Generator (DFIG)	Static generators
Insensitivity to voltage variations	X	X	X	X	X
Participation in voltage control	X	X $P_{SG} \geq 6$ MW	X	X	X
Frequency regulation	X	X	X	X	X
Support for voltage during a short circuit	-	-	X	X	X
Participation in defence plans	X $P_n \geq 100\text{kW}$	X $P_n \geq 100\text{kW}$	X	X	X

Frequency regulation is an essential service for ensuring the correct operation of an electric power system. The typical operating frequency ranges of standard Conventional Power Plants (CPP) is 47.5 Hz $\leq$ f $\leq$ 51.5 Hz. Distributed generation in Italy is built and programmed to provide frequency regulation, but the service is not active today. The frequency is linked to the rotation speed of the SG that are active in the power station. Frequency must be kept the most constant possible, trying to guarantee a balance between electricity production and load. In case of an instantaneous power imbalance, the frequency could have a transient in over-frequency if the inequality is an excess of electricity production, or under-frequency if it is a generated power deficit. Transient stability problems are often associated with inadequacies in power system component responses, poor coordination of control and protection equipment or insufficient generation reserve, producing sudden frequency deviations from the nominal value [63],[64]. Table 2.2 shows the frequency responses of CPPs to systems contingencies.

Table 2.2: The frequency response.

Response	Stage	Impact	Origin
Transition	Electromagnetic energy release	Maintain synchronism.	The magnetic field of synchronous
	Inertial response (IR)	Slow down ROCOF	Kinetic energy from the rotor
1	Primary frequency control PFR	Bring frequency to the steady-state level	Frequency responsive reserve
2	Automatic generation control SFR and TFR	Bring frequency back to its nominal value	Contingency reserve

During the first instants from the contingency (approximately in the first 3 seconds), the kinetic energy stored in the rotors of the SG contrasts the frequency variation due to the mechanical and electromagnetic torques unbalance, limiting, in this way, the frequency nadir and the Rate of Change of Frequency (RoCoF) in the case of lack of generation. After this stage, the Primary Frequency Response (PFR) process limits the steady-state frequency error that the Secondary Frequency Response (SFR) process removed in about 30 min. Finally, the Tertiary Frequency Response (TFR) restores the capacity reserve of the system. The primary frequency regulation service today is provided by conventional production units of considerable sizes that reserve 10% of its nominal power as the minimum safety value that guarantees continuity to the electrical system. It is a mandatory service rewarded based on the regulatory energy provided, following the resolution 231/2013/R/EEL. The representation of the different frequency response indicators with a disturbance is shown in Figure 2.1 [65].

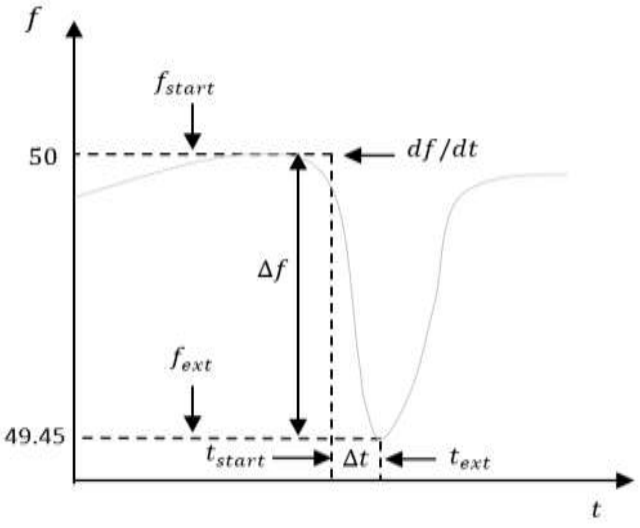

Figure 2.1: Frequency response indicators.

In Figure 2.1 is:

- f_{start} is the frequency at that time;
- $f_{extreme}$ is the minimum instantaneous frequency during a disturbance;
- t_{start} is the minimum instantaneous time occurred during a disturbance;
- $t_{extreme}$ is the start time occurred during a disturbance;
- Δf is the difference between the minimum or maximum instantaneous frequency deviation and the frequency at the start of the disturbance;
- $\frac{df}{dt}$ is the RoCof [3];
- Δt is the time to reach the maximum frequency deviation.

During the PFR, the active power injection is managed in three ways:

- regulation around the nominal frequency denominated as Frequency Sensitive Mode (FSM) for small frequency variations;
- under-frequency regulation denominated as Limited Frequency Sensitive Mode at under frequency LFSM-U for large variations below the nominal frequency;
- over-frequency regulation denominated as Limited Frequency Sensitive Mode at over frequency LFSM-O for large variations above the nominal frequency.

Figure 2.2 shows the types of frequency regulations [37].

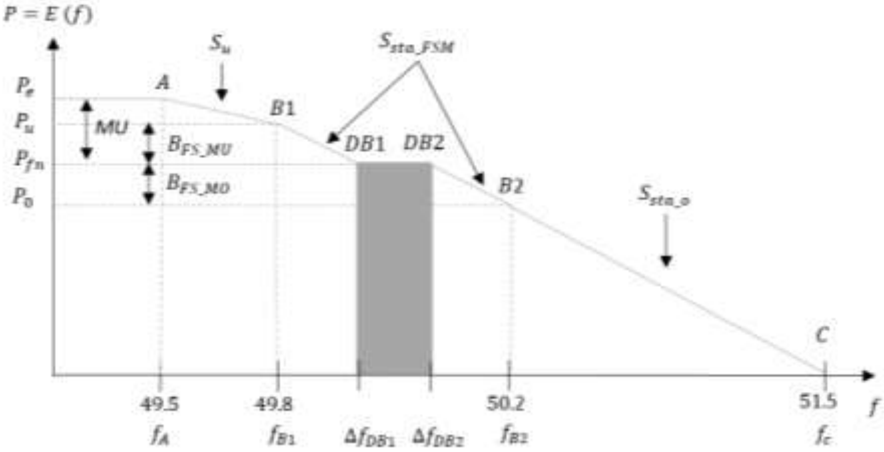

Figure 2.2: Characteristic curve P = E (f).

where:

- P_e represents the maximum active power that can be supplied by the generating unit;
- P_{fn} represents the active power supplied in the dead band area around the rated frequency f_n, between fB_1 and fB_2;
- P_u represents the maximum active power reached during the under frequency transient;
- S_{sta_u} represents the under frequency statism between points A and B1,
- S_{sta_o} represents the over-frequency statism between points B2 and C;
- S_{sta_FSM} represents the statism around the nominal frequency value between points B1-DB1 and DB2-B2M
- B_{FS_MU} represents the under-frequency power regulation band through FSM mode;
- B_{FS_MO} represents the over-frequency power regulation band through FSM mode;
- MU represents the permissible increase margin to make an under-frequency adjustment;
- f_{B1} represents the frequency limit of the LFSM-U regulation mode;
- f_{B2} represents the frequency limit of the LFSM-O regulation mode;

- f_A represents the lower frequency limit of the operating range defined by the standard;
- f_C represents the upper-frequency limit of the operating range defined by the standard;
- the interval $\Delta f_{B1} - \Delta f_{B2}$ represents the lower and upper-frequency limit of the dead band.

Statism is defined, according to art. 2 points 23 of EU Regulation 2016/631 as the "Ratio between a permanent change in frequency and the resulting permanent change in the active power produced, expressed in percentage terms. The change in frequency is expressed concerning the rated frequency. In contrast, the change in active power is expressed concerning the maximum power or adequate active power when the relevant threshold is reached. "
Table 2.3. shows the numerical values for points A, B1, B2 and C.

Table 2.3: Response frequency.

Point	P/P_e	f [Hz]	
A	1	f_A	49.5
B_1	0.985	f_{B1}	49.8
B_2	0.985	f_{B2}	50.2
C	0.5÷0	f_C	51.5
DB1-DB2	0.985	Δf_{B1}-Δf_{B2}	50±0.5

Figure 2.3 shows the correlation of frequency response and active power.

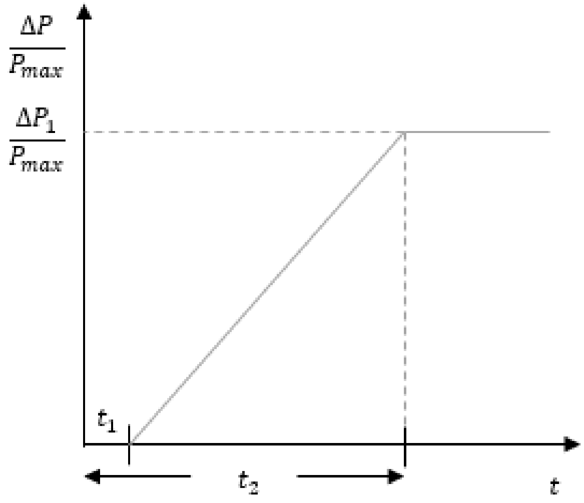

Figure 2.3: Active power response.

t_1 represents the initial response delay and t_2 represents the total activation time. Table 2.4 summarizes the response characteristics of the power plants above 10 MW in Italy (source Standard CEI 0-16).

Table 2.4: Response characteristics of power plants.

Parameter	Generation parks			
	PV	Wind	Hydroelectric	Thermoelectric
Statism	4%	4%	4%	5%
Amplitude of the response $\Delta P/P_{max}$	10%	10%	10%	8%
Complete activate time t2	2s	10s	30s	30s

2.3. System Inertia

The loss of SG for including new static generators in the grid has a negative impact on the stability of the electric power system. Two factors are mainly affected by this change: the IR of the system and the protection schemes. The IR is an intrinsic property of the rotating machines and can be calculated as:

$$H = \frac{J\omega_0^2}{2A_n} \tag{2.1}$$

where J represents the moment of inertia of the rotor of the SG expressed in $kg.m^2$, A_n is the rated apparet power of the SG and ω_0 represents the rated angular velocity in rad/s.
Typical values of H_i are reported in Table 2.5. In the case of RES generators interfaced with static converters *H=0s*.

Table 2.5: Typical inertia values.

Type of Generation Unit	H [s]
Thermal unit	4.0 to 10.0
Diesel unit	1.0 to 2.0
Wind	0
Solar	0
Hydraulic unit	2.0 to 4.0

The inertia provides a measure of the ability of the entire electric power system to resist sudden changes in the balance between electricity demand and electricity production. IR, together with PFC, enhances system stability by reducing the RoCoF and the nadir (minimum value) of the frequency.
The inertial of the whole power system to which more generators (SGs and RES generators) are connected can be calculated according to [36], [66] and [67] as

$$H_{sys} = \frac{\sum_1^g H_i \, . \, A_{n,SG,i}}{\sum_1^g A_{n,SG,i} + \sum_1^r A_{n,RES,i}} \tag{2.2}$$

The RoCof is the time derivative of the frequency and is an essential measurement for assessing the behaviour of the system [39]. In the presence of more generator, the RoCof, following a disturbance $\Delta P_{imbalance}$ is:

$$RoCoF = \left.\frac{df}{dt}\right|_{t=0+} = \frac{\Delta P_{imbalance} \cdot f_0}{2. \sum_{i=1}^{n} H_i \,.\, A_{n,SG,i}} \tag{2.3}$$

where f_o is the frequency of the system when the disturbance occurs, usually assumed equal to the rated frequency.

The product between the rated power and the inertia constant of an SG is the kinetic energy of the rotor $E_{k-i} = H_i \,.\, A_{n,SG,i}$. In [68], [69], [70] is calculated the total kinetic energy of the system by the following proposed equation:

$$E_{k-sys} = \sum_{i=1}^{n} E_{k-i} \tag{2.4}$$

where $A_{n,SG,i}$ is the rated power of the i-th SG and $A_{n,RES,i}$ is the rated power of the i-th RES generator.

The RoCof can be expressed considering the total kinetic energy of the system as:

$$RoCoF = \left.\frac{df}{dt}\right|_{t=0+} = \frac{\Delta P_{imbalance} \cdot f_0}{2. E_{k-sys}} \tag{2.5}$$

The continuity of the electric service during the first moments after a disturbance can generate sudden changes in frequency, voltage and power angle that could vary depending on the rapid inertial response. Therefore, a low IR value and low values of the kinetic energy may not be able to cope with a contingency.

Imposed a limit to the RoCoF ($RoCoF_{max}$) and considering the maximum disturbance that con occur in a grid, it is possible to estimate the minimum value of the inertia constant that can be accepted in a system as:

$$H_{Sys,min} = \frac{\Delta P_{imbalance} \cdot f_0}{2. P_{load} \cdot RoCoF_{max}} \tag{2.6}$$

The minimum inertia can be used for estimating the maximum RoCoF during the first moments of an incident using the following relation:

$$RoCoF_{max} = \frac{\Delta P_{imbalance} f_0}{P_{load} H_{min}} \tag{2.7}$$

Table 2.6: Limits of RoCoF.

Reference	Limits of RoCoF
Photovoltaic	2 Hz/s
Wind	4 Hz/s
CPP	Short circuit powers
	Moving averages: e.g., 2 Hz/s for transferring average 500 ms window, 1.5 Hz/s with 1-second window, and 1.25 Hz/s for 2 s window.
	Creating a frequency-time profile

The utility evaluates the limitations of RoCoF, considering the characteristics of the system based on the disturbances in frequencies generated by failures in lines or blackouts. On average, based on literature, ENTSO-E documents suggest the limits proposed in Table 2.6 [33].

2.4. Frequency nadir

For assessing the frequency nadir, the authors of [81] presented a simplified formula that can be useful for a preliminary evaluation of the maximum frequency deviation to compare different scenarios:

$$\Delta f_{max} = \frac{\Delta P_{imbalance}}{D} \cdot \left(e^{\frac{DT_d}{2H_{sys}}} - 1 \right) \tag{2.8}$$

where D is the load frequency dependence and T_d is the time constant for the governors responding with FCR. Frequency nadir is essential data since the minimum frequency values reached during a disturbance depends on the disconnection of the distributed generators of the system.

2.5. Conclusion

The Chapter has introduced to the reader the issue of frequency regulation focusing on the inertial response from classical and futuristics stations. The main characteristics of IR have been presented, followed by concepts that will be used in the rest of this thesis. In the next chapter, the characteristics of the grids of two small islands will be presented.

Chapter 3

Analysis of the Generating and Distribution systems and of the Inertial Response of two small islands

3.1. Introduction

This Chapter deals with the examination of the effects on the total system inertia constant and kinetic energy in small islands not supplied by the main grid of the Mediterranean sea. Initially, the characteristics of the power systems of Lampedusa and Pantelleria islands are presented. Then, a simple method to evaluate the variation of the IR of the system is applied to the two islands and the effects of such variations are assessed using typical load profiles during typical summer and winter weeks. Then, the dynamic response of the small islands' frequency adjustment systems is simulated considering the states with maximum and minimum inertia in the case of loss of generation and a failure in a line.

3.2. The generation system

The present thesis uses as case studies two small islands of the Mediterranean Sea: Pantelleria (TP) and Lampedusa (AG), located between Sicily and North Africa and whose power systems are totally isolated from the main national grid of Italy [71]. The current electricity production systems of both islands are mainly based on diesel fuel thermal power plants with suitable control systems in order to guarantee a secure and reliable grid operation. Each island has eight diesel generators with different rated power: Lampedusa has a total installed power of 22.5 MVA, while Pantelleria has a total installed power of 24.5 MVA. Figure 3.1. shows the rated power of each of the eight generators of the two islands.

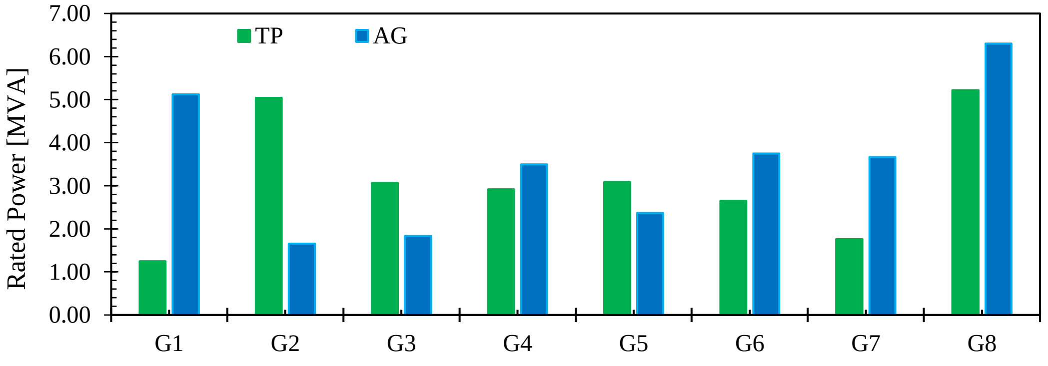

Figure 3.1. Rated power of the eight generators of Lampedusa (AG) and Pantelleria (TP).

In both islands, the diesel SGs are located in a unique power station supplying the 10 kV Medium Voltage (MV) grid of the island. The structure of the local MV grids is reported in Appendix A. In terms of electricity production cost, the isolated power systems are characterized by a higher price with respect to the mainland due to the following reasons:

- the local power plant is significantly oversized to have enough backup power in the case of failure;
- the energy demand varies considerably during the year, with a considerable reduction during winter;
- the cost of fuel transportation from the mainland;
- the cost of maintenance of the eight diesel generators.

The average cost of electricity production is about six times higher than the national cost. For this reason, the liberalisation of the Italian energy sector in 2009 recognises an incentive to cover the higher costs for electricity production in the isolated power system. This incentive was introduced in the electricity bills, denominated as UC4 (now collapsed inside the incentive Arim). In this way, who lives in small islands purchases electricity at the same price as the mainland. It is estimated that this incentive generates an income of 70 M€/year, of which about 13 M€/y for Lampedusa and 9 M€/y for Pantelleria.

On the other hand, the power plants are responsible for SO2, NOx and dust emissions: for this reason, they must be eliminated or renewed by 1st January 2030. This obligation derives by the Directive 2015/2193/EU, and in the next years, it will lead to more and more installations of new power plants based on RES.

RES production may prove practical for small power needs in isolated places. Still, it should be used for maximum flexibility in conjunction with other power generation methods to ensure continuity.

The diesel oil consumption and generators average specific fuel consumption during the year 2018 for Pantelleria, and during the year 2016 for Lampedusa are reported in Figure 3.2 where is emphasised the similar power consumption, with the highest electricity demand in both islands in summer as a consequence of the continuous flow of tourists. The significant variation in electricity production between summer and winter is a typical situation in small islands whose touristic flows have a substantial impact on the energy demand.

Regarding the capacity of the power plant, as in many Italian small islands, the generating system is oversized mainly compared to the average demand. The annual electricity production is about 36.2 GWh (2016) for Lampedusa and 36.5 GWh (2018) for Pantelleria. In general, the electricity production yearly in the two islands has an approximate summer peak in August of 4.6 GWh [72], while the minimum is 2.5 GWh in winter as is shown in Figure 3.3.

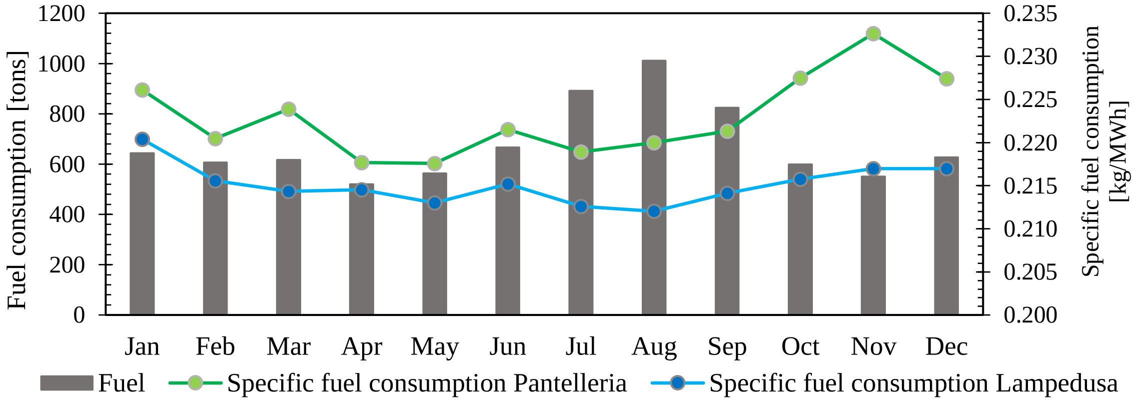

Figure 3.2. Monthly electricity production and corresponding fuel consumption.

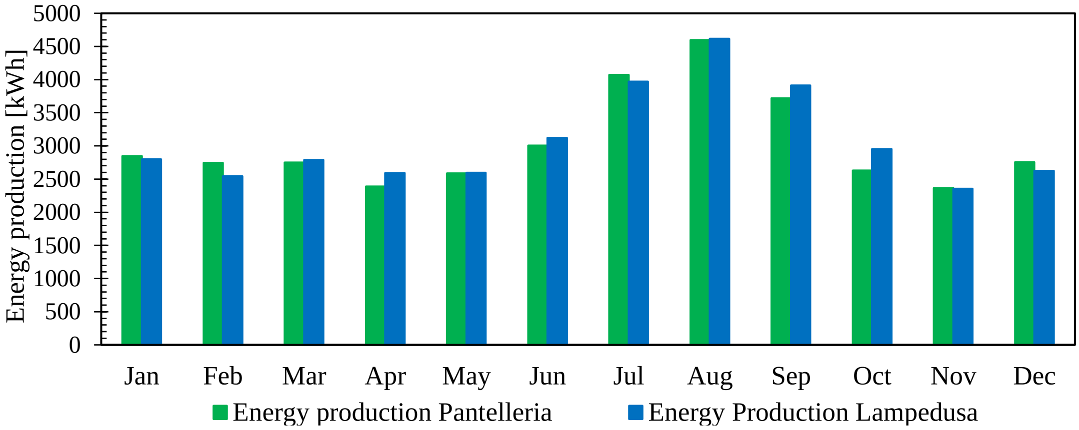

Figure 3.3. Monthly energy production.

3.3. Load profiles

The load profiles for the year 2017 are provided by the local utilities: S.MED.E. Pantelleria S.p.A. (Palermo, Italy) and SELIS Lampedusa S.p.A. (Palermo, Italy). Both companies are vertically integrated, providing electricity production, distribution, and supply. Nevertheless, Pantelleria had some renewable plants installed within the island, whose installation was recently pushed by Ministry Decree 14th February 2017 [73], [74]. The profiles in Figure 3.4 represent the typical daily profiles of the islands.

Figure 3.4 reveals the following aspects: the first is a confirmation of the higher demand in Summer, the second is the similarity of the power load of the two islands during all year.

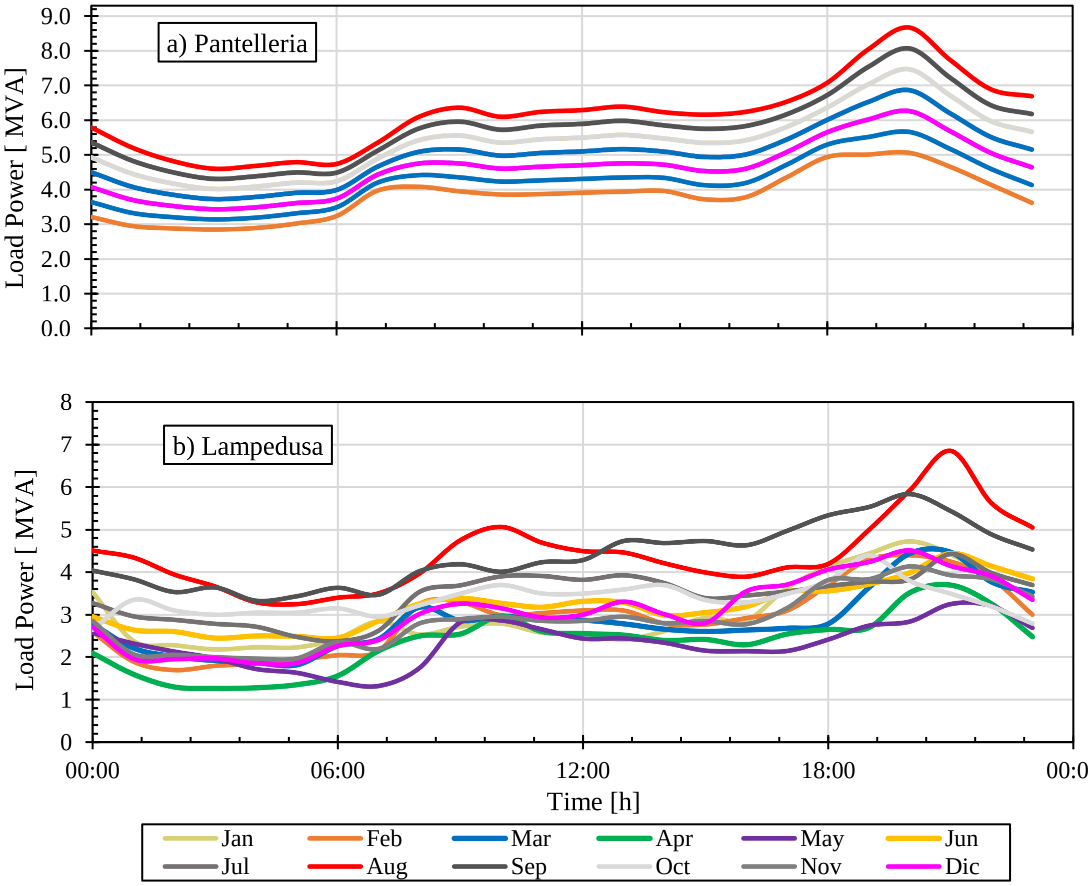

Figure 3.4. Typical daily load profile of Pantelleria and Lampedusa.

For the stability analysis that will be presented in the following, typical summer and winter weeks have been considered and represented in Figure 3.5 for Lampedusa and Pantelleria (S-P: Summer-Pantelleria; S-L: Summer-Lampedusa; W-P: Winter-Pantelleria; W-L: Winter-Lampedusa).

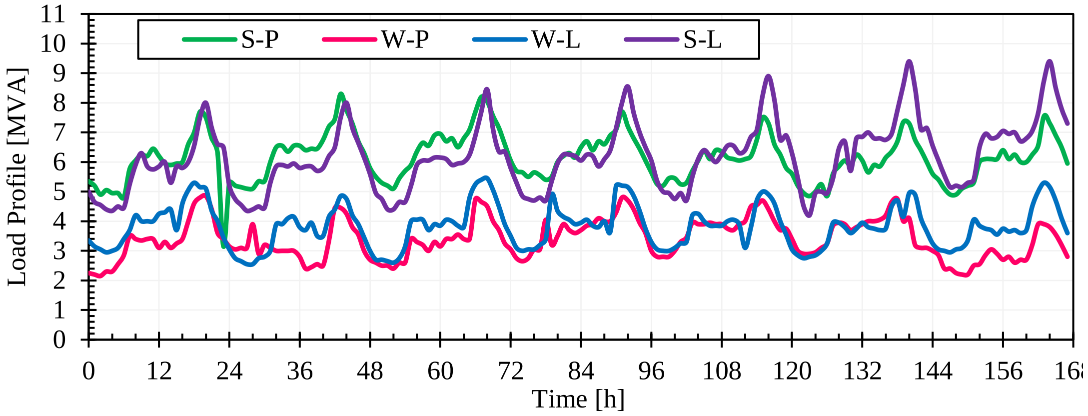

Figure 3.5. Typical load profile during a week in Winter and Summer.

The analysis of the load diagrams shows that:

- during Summer, Pantelleria registers peaks of electricity production between 6.5 MVA and marginally more top than 7.5 MVA between 18:00 and 22:00;
- during Winter, Pantelleria registers peaks of electricity production between 4 MVA and marginally more top than 4.85 MVA between 18:00 and 21:00;
- during Summer, Lampedusa registers peaks of electricity production between 6.5 MVA and marginally more top than 9.4 MVA between 17:00 and 22:00;
- during Winter, Lampedusa registers electricity production peaks between 4.5 MVA and marginally more top than 5.5 MV between 17:00 and 20:00.
- the minimum load for Pantelleria is recorded during Winter at 2:00 and is about 2.15MVA. The average power is about 6.13 MVA during Summer and about 3.39 MVA during Winter;
- the minimum load for Lampedusa is registered during Winter at 3:00 and is about 3.18 MVA. The average power is about 4.78 MVA during Summer and about 3.39 MVA during Winter;

Figure 3.6 shows the operation of the SGs in the CPPs for 336 hours.

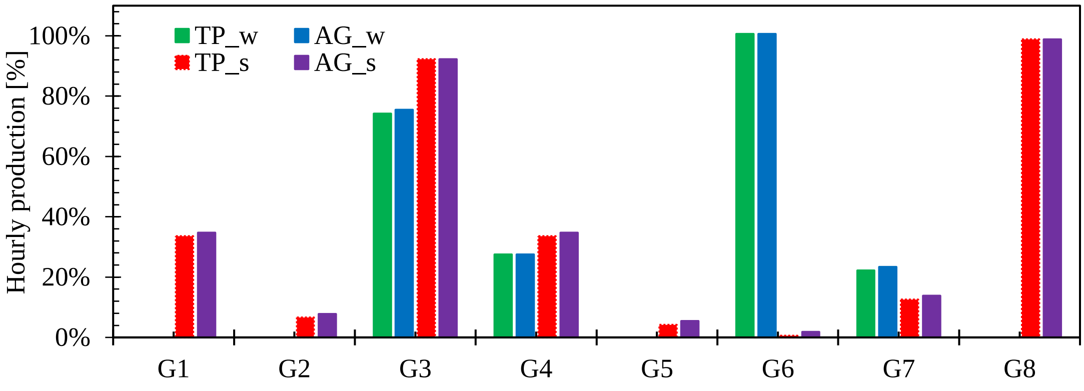

Figure 3.6. Active generators of typical load profile during a week in Winter and Summer.

The Active SG from G1 to G8 are divided into four groups as TP w (Pantelleria Winter), TP s (Pantelleria Summer), AG w (Lampedusa Winter), and AG s (Lampedusa Summer).

3.4. Inertial Response

At today, the SGs of the two islands produce most (almost the whole) of the electricity required and participate in the regulation of the active/reactive powers to obtain a regular system operation. Depending on the islands demand, it is possible to identify three electromechanical operating characteristics of the alternators:

- $P_g = P_c$, the machine will rotate with a uniform circular motion. The angular speed of the machine and the electrical pulsation are constant because the driving torque of the rotating shaft is equal to the load resisting torque;
- $P_g > P_c$, the rotor accelerates generating an over-frequency transient because the driving torque is higher than the resisting torque;
- $P_g < P_c$, the rotor slows down, generating an under-frequency transient, because the driving torque is lower than the resisting torque.

The companies that provide the energy service within the islands do not have verification of power systems security in the inertia estimation service function. In this way, Chapter 2 realises an algorithm for estimating the current IR and kinetic energy using Equations 2.2 and 2.4. Figure 3.7a shows the current IR estimation for Pantelleria and Lampedusa grids, and Figure 3.7b shows the current kinetic energy estimation from internal generators (approximately, the CPP deliver average inertia of 2.35s and maximum kinetic energy of 42.5 MWh).

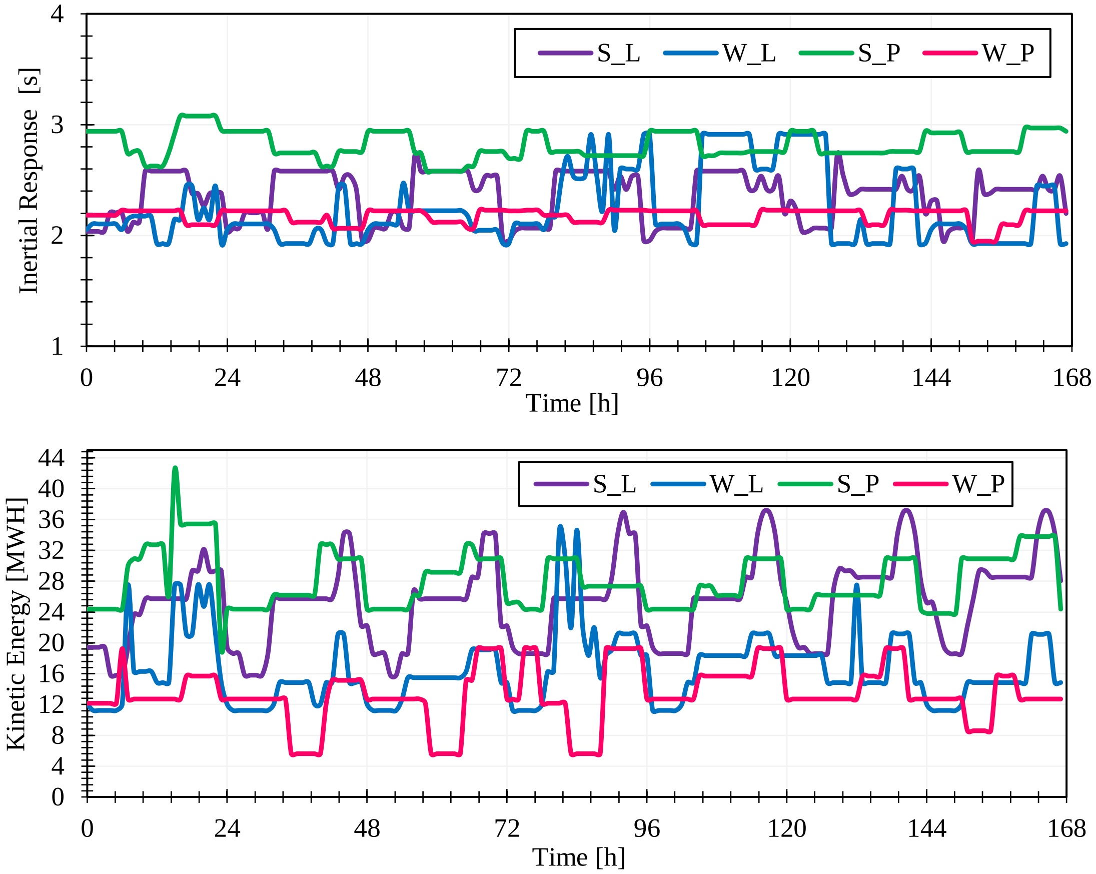

Figure 3.7. Trend estimation of a) IR and b) Kinetic Energy.

The trends in Figure 3.7 shows that:

- In Summer, Pantelleria has a minimum inertia $H_{min} = 2.58s$, with four active generators and a maximum inertia $H_{max} = 3.07s$, with three active generators. The minimum kinetic energy is $K_{min} = 19.1$ MWh and the maximum is $K_{max} = 42.5$ MWh;
- In Winter, Pantelleria has a minimum inertia $H_{min} = 1.94s$, with two active generators and a maximum inertia $H_{max} = 2.22s$, with two active generators. The inertia is similar in 70% of the hours. The minimum kinetic energy is $K_{min} = 5.62$ MWh and the maximum is $K_{max} = 19.3$ MWh;
- In Summer, Lampedusa has a minimum inertia $H_{min} = 1.95$s, with four active generators and a maximum inertia $H_{max} = 2.73$s, with two active generators;
- In Winter, Lampedusa has a minimum inertia $H_{min} = 1.93$s, with three active generators and a maximum inertia $H_{max} = 3.07$s, with one active SG;

3.5. Transient behaviour of the isolated power system

The present section shows an example of how the system response differs with the season. The dynamic behaviour of the isolated power system is shown for two cases with the highest load during a Summer and Winter week in Lampedusa island. A simulation has been done implementing the networks in Appendix A in NEPLAN environment. For these simulations, two different incidents were considered:

- Incident f_0: a line fault occurs at t = 5 s and lasts 2 s;
- Incident Less_G3: a generator is switched off at t = 5 s and then is switched on after 2 s.

Figure 3.8 a and b show the trends in the two cases. Both cases create a sudden drop in frequency before the governor control stabilizes the grid frequency at a steady-state value. Then, the frequency is driven back to its standard value by the automatic generation control.

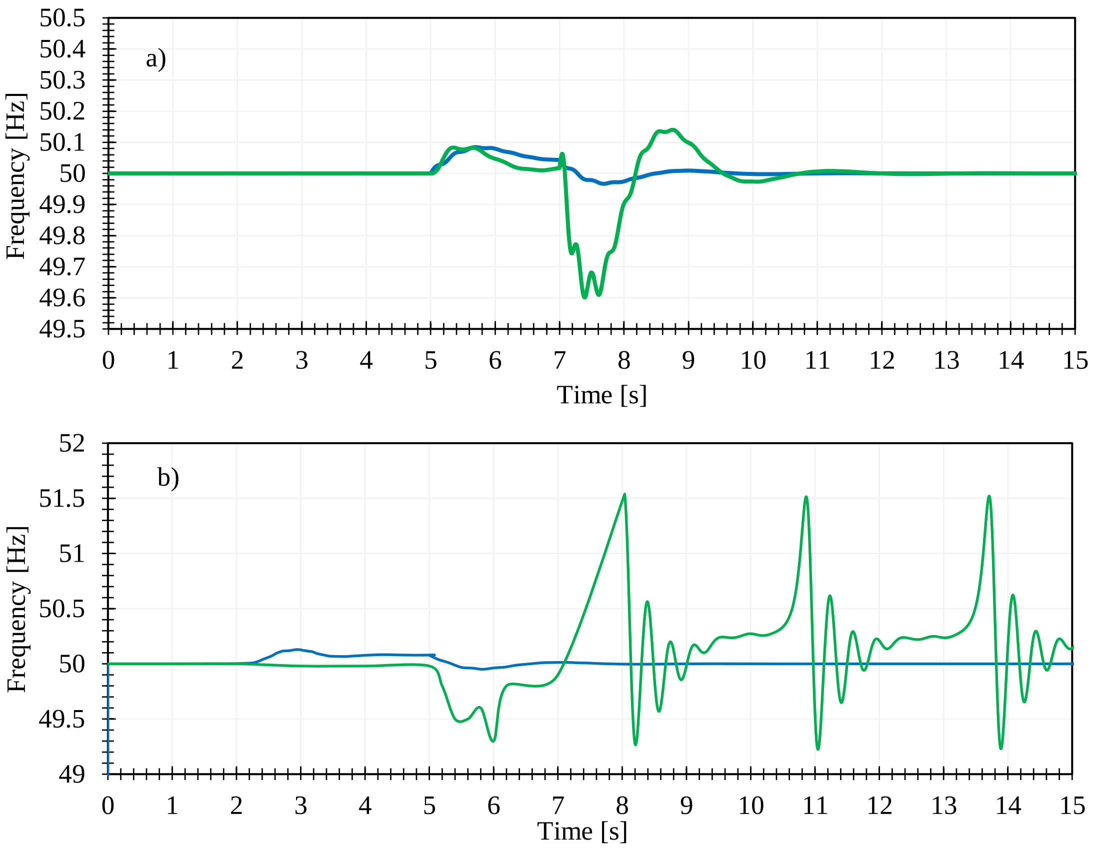

Figure 3.8. Frequency response for two incidents within Lampedusa grid: a) Incident f_0; b) Incident Less_G3. Blue line: Summer; Green line: Winter.

In Table 3.1 are reported the parameters that characterise the dynamic behaviour of the system in the two examined cases.

Table 3.1. Response parameters.

Case		Nadir	Zenith	Δt	T_r^*	f_∞
a	Summer	49.96	50.07	7.6	9.03	49.997
	Winter	49.60	50.13	7.38	10.78	49.998
b	Summer	49.95	50.12	10.5	11.81	49.968
	Winter	49.45	51.58	6	Instability	Instability

f_∞ represents the value in Hz at the steady-state after the disturbance, T_r^* represents the settling time, that is the period for establishing the response within the tolerance range of the set value. The frequency Zenith represents the maximum positive excursion of the frequency from the steady-state value.

3.6. Conclusion

In this Chapter, the characteristics of the isolated grid of Lampedusa and Pantelleria were presented. Then, the inertial response of the island was calculated considering the electricity production data per hour and the different behaviour in summer and winter was shown considering two disturbances. This part of the thesis is propedeutic to the successive study on RES penetration and frequency control in small islands. In the next chapter, the effects of RES-based generators interfaced with static converters to the grid on the system inertia will be discussed.

Chapter 4

Analysis of the inertial response in the presence of generation from RES

4.1. Introduction

RES is posing critical issues related to the mining of power systems stability due to the reduction of the generation by conventional power plants and the subsequent decrement of the inertial response during the system's contingencies. Consequently, for preserving the security and the reliability of the system, it is necessary to have recourse to new frequency adjustments mechanisms. This issue is particularly current in isolated power systems like those of small islands not supplied by the main grid, in the case of high shares of production from unpredictable renewables such as photovoltaic and wind sources. In this context, the present chapter deals with analysing the variation of the inertia time constant of an islanded power system of a small island in various scenarios characterized by different share of renewable energy. In particular, as an example, the power system of Lampedusa will be analyzed [36].

4.2. Premise to the analysis

The urgent need of contrasting climate changes due to the high consumption of fossil fuels has led to the development of RES-based generators as commercially viable devices for cleanly producing electric energy. RESs represent a positive social contribution in terms of clean and unlimited energy and are becoming the most feasible step to face the increase in energy demand with low or null greenhouse gases (GHG) emissions [33]. Consequently, the characteristics of the electrical power system are changing, in such a way that they require new challenges in terms of intelligent networks, remote control, stability and power quality [75].

Since the current tendency is to increase the share of photovoltaic (PV) and wind plants in the energy mix, CPPs are gradually reducing their production, but this transformation introduces new challenges for power systems transient stability. CPPs can provide a considerable amount of rotating inertia, thanks to the kinetic energy stored in SG, they contrast load and generation sudden variations and limit the frequency nadir and the maximum RoCoF.

The transition to an energy system based on RES has characteristics of variability, uncertainty and lack of synchronism that causes challenges to keep the energy system reliable and safe. Many research studies have argued that the main problem is that RES-based plants do not provide IR to system's contingencies and, for this reason, they are more inclined to favour instability [76], [77], [78]. Therefore, with the increase in the production from RES, the operating conditions will be less and less reliable, since transients due to fault or sudden reduction of generation/demand could generate stress for the remaining CPPs and increase the probability of cascade trips [79]. This issue is particularly current in power systems of small islands not supplied by the main grid, where the high shares of production from solar and wind is due to the favourable climatic conditions and by the needs of reducing air pollution due to the use of old and often not efficient diesel generators.

In this context, in the following paragraphs, the examination of the effects on the total system inertia constant of the increasing share of energy production from RES in Lampedusa is assessed. The variation during 24 hours of the inertia constant of the island's power system is evaluated considering typical generation profiles for a Summer and a Winter day for three different production shares from RES. The study aims to draw a framework of variation for the power system's IR to evaluate possible solutions for supporting CPPs during system's contingencies and enhancing system stability.

The theme is of great interest for all the utilities managing the generation and distribution grid of small islands without cable connection with the main distribution grid.

4.3. Methodology

The following steps are necessary for assessing the impact on the system inertia of high shares of RES in an isolated system:

- Step 1: since, typically, small islands are characterised by very different Summer and Winter daily load profiles, two typical daily load profiles and the related generation plans for the CPPs are considered. Each plan indicates for each hour the power produced by each SG. The daily load profiles identify the base scenario (Scenario 0).
- Step 2: the system inertia is calculated for every hour according to the procedure in Section 2.3.3.
- Step 3: the system inertia is for 24 hours for both the Summer and the Winter typical day.
- Step 4: a scenario characterised by a given share of production by RES is selected.
- Step 5: the daily generation plans are modified reducing the production from CPPs (or, eventually, switching them off) for allowing the RES plants to provide energy to the load and, in this way, a new scenario is defined.
- Step 6: Steps 2 and 3 are repeated for the new scenario.

The above-described methodology evaluates how maximum and minimum system inertia varies when a given percentage of energy production from RES is introduced in the isolated system.

4.4. Preliminary study

Figure 4.1 represents the Summer (in green) and Winter (in blue) daily load profiles of Lampedusa assumed in Scenario 0.

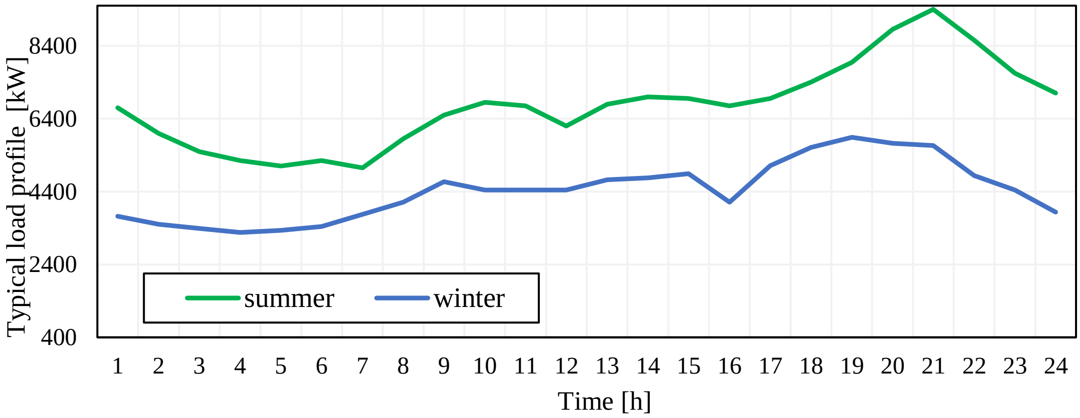

Figure 4.1. Summer and winter typical daily load profile.

Scenario 0 is characterised by a Summer peak power of 9400 kW at 9:00 p.m. and a Winter peak power of 5400 kW at 8:00 p.m. Figure 4.2 shows the trend of the system inertia during the 24 hours of the two days without RES.

For the calculation of H_{sys} uses Equation 2.6, which, can be express in the function of each hour of the day, and the data of the SGs reported in Table A.1 (Appendix).

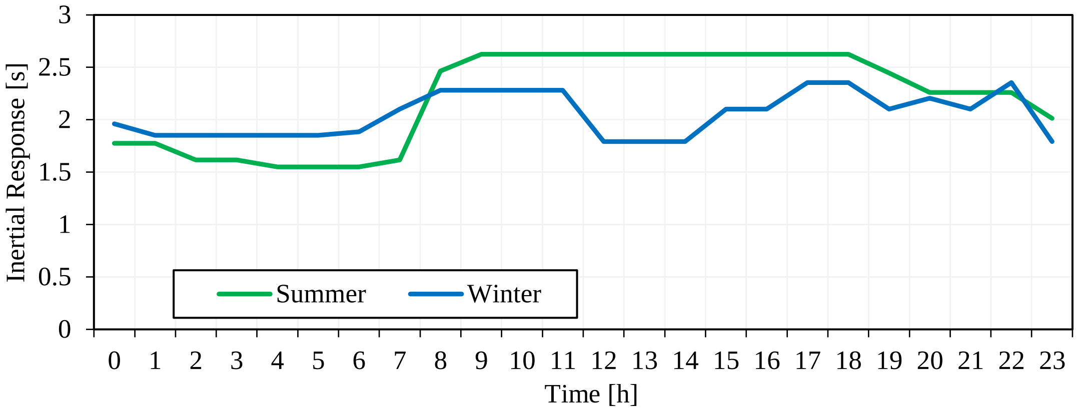

Figure 4.2. Scenario 0: System inertia variation during the day.

For analysing the effects of RES plants on the system inertia three scenarios with penetration of 20%, 50% and 70% are considered. As presented in [36], starting from Scenario 0. Then, three scenarios with a penetration of 20%, 50% and 70% from RES proposes.

- Scenario 1: The base Scenario 0 is modified by considering the generation of a certain quota of energy from RES plants during the hours of the days characterised by the highest demand. Figure 4.3 illustrates the scenario conceptually. The green area identifies the hour in which RES covers a fixed percentage of the energy production of the island. For the examined case study, it is assumed that RES plants produce between 9:00 a.m. and 3:00 p.m. In this scenario, the generation plan of the system change in those areas by reducing the power produced by the CPPs and switching off some synchronous generators; in particular, obtaining that the power generated by G8 decreases.

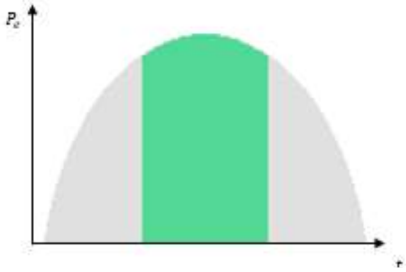

Figure 4.3. Scenario 1: conceptual description of the procedure. The RES-based generation plants produce during the highest demand hours.

- Scenario2: The base scenario 0 is modified by including a constant share of energy produced from RES in the 24 hours of the two typical days, as represented in Figure. 4.4.

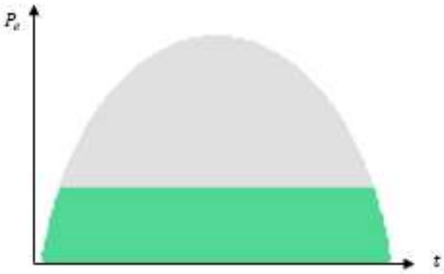

Figure 4.4. conceptual description of the procedure. The RES-based generation plants produce during the whole day with a constant share.

- Scenario3: The base scenario 0 is modified considering a percentage proportional to the power demand of the hour of the island, as shown in Figure. 4.5.

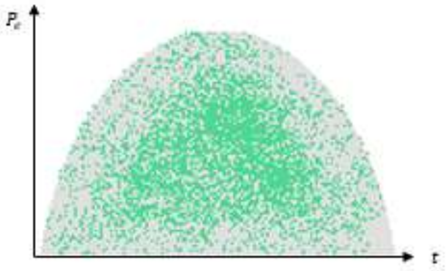

Figure 4.5. Scenario 3: conceptual description of the procedure. The RES-based generation plants produce a share of energy proportional to the hourly demand.

Figure 4.6 shows Scenario 1 (4.6a), Scenario 2 (4.6b), and Scenario 3 (4.6c) with RES 70% for Summer (yellow line) and Winter (Pink line), RES 50 % for Summer (violet line) and Winter (grey line), RES 20% for Summer (green line) and Winter (blue line).

As shown in Figures 4.6, the presence of RES considerably affects the system's inertia and, consequently, its stability. Therefore, the impact can be assessed, evaluating:

- the maximum allowed disturbance for different values of $RoCoF_{max}$ in the condition of maximum and minimum load for Summer and Winter, starting from Equation (2.6) suitably elaborated:

$$\Delta P_{imb,x} = \frac{2. E_{kin}. RoCoF_{max}}{f_0} \tag{4.1}$$

- the frequency nadir for a given disturbance (it is assumed a disturbance of 2% of the total load) using Equation (2.8).

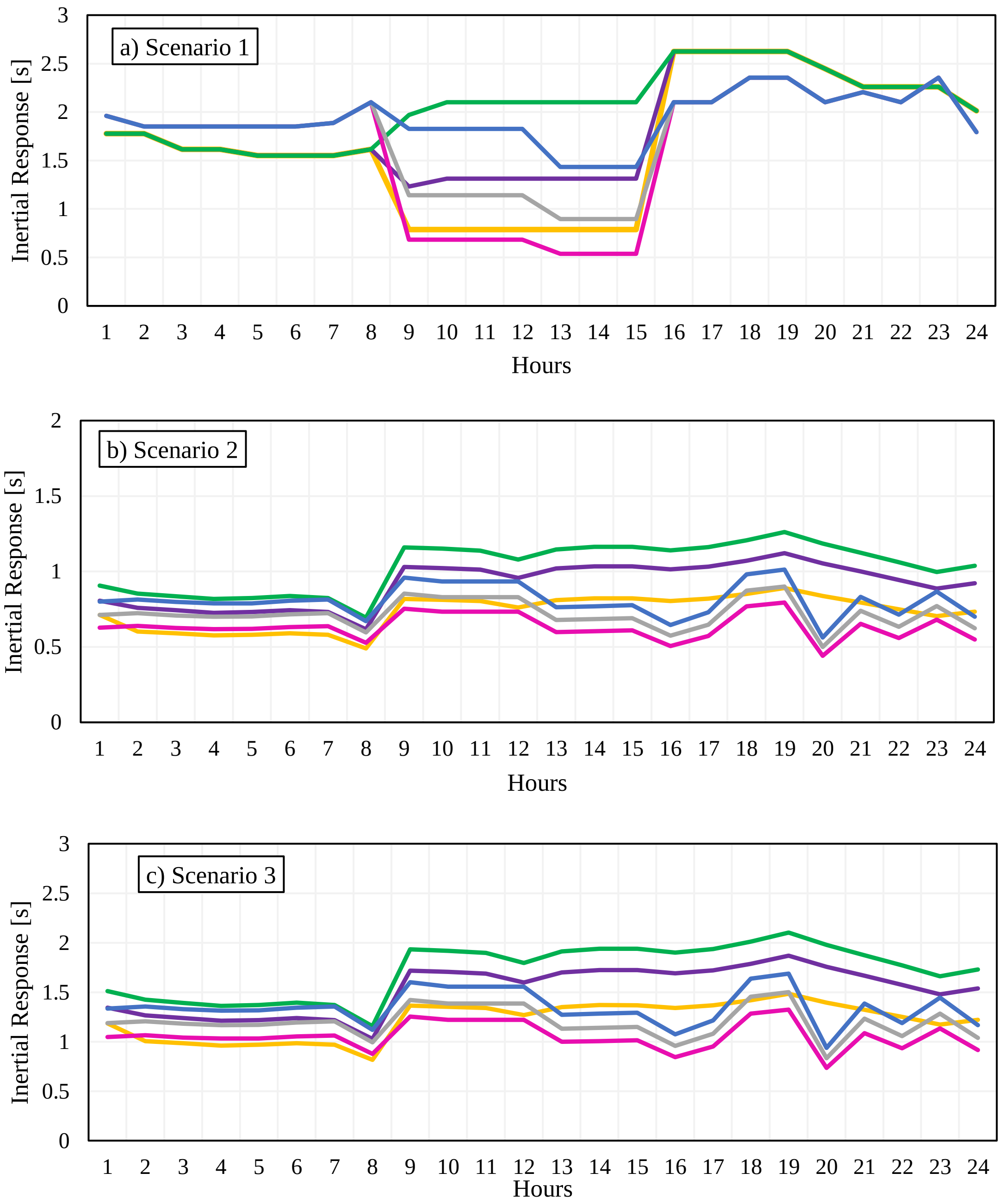

Figure 4.6. System inertia variation in the three scenarios is based on three different RES (20%, 50% and 70%).

The results of the calculation of the maximum imbalance, presented for a RES penetration of 70% (worst case), reported in Table 4.1, show how the inertia reduction severely impact on the stability of the system reducing the maximum allowed imbalance. The decline is more visible in Scenario 2, being the RES contribution present every hour of the day with the same percentage.

Table 4.2 reports the frequency nadir for the different scenarios assuming D=1.04 and T_d=10s.

Table 4.1. Maximum imbalance allowed as a function of the system inertia and RoCoF_{max}.

Season	P_{load}	H_{sys} [s]				RoCoF_{max}	ΔP_{imb}			
	[kW]	Sc.0	Sc.1	Sc.2	Sc.3	[Hz/s]	Sc.0	Sc.1	Sc.2	Sc.3
Summer (Maximum)	9400	2.26	2.26	0.79	1.32	2	18%	18%	6%	11%
						1	9%	9%	3%	5%
						0.5	5%	5%	2%	3%
Summer (Minimum)	5050	1.55	1.55	0.58	0.97	2	12%	12%	5%	8%
						1	6%	6%	2%	4%
						0.5	3%	3%	1%	2%
Winter (Maximum)	5888	2.35	2.35	0.79	1.32	2	19%	19%	6%	11%
						1	9%	9%	3%	5%
						0.5	5%	5%	2%	3%
Winter (Minimum)	3277	1.85	1.85	0.62	1.03	2	15%	15%	5%	8%
						1	7%	7%	2%	4%
						0,5	4%	4%	1%	2%

Table 4.2. Frequency nadir in different Scenarios 0, 1, 2 and 3.

Season	P_{load}	H_{sys} [s]				D	ΔP_{Imb}	f_{nadir} [Hz]			
	[p.u.]	Sc.0	Sc.1	Sc.2	Sc.3		[%]	Sc.0	Sc.1	Sc.2	Sc.3
Summer (Maximum)	0.94	2.26	2.26	0.79	1.32	1.04	2%	49.34	49.34	49.07	49.17
Summer (Minimum)	0.505	1.55	1.55	0.58	0.97	1.04	2%	49.22	49.22	49.05	49.10
Winter (Maximus)	0.5888	2.35	2.35	0.79	1.32	1.04	2%	49.36	49.36	49.07	49.17
Winter (Minimum)	0.3277	1.85	1.85	0.62	1.03	1.04	2%	49.27	49.27	49.05	49.12

4.5. Conclusion

Based on the results presented in this chapter, it is possible to conclude that the penetration of a large share of RES generation in a small isolated system can easily compromise the stability of the system. An accurate study of the threats for the system's security must be done considering all the possible operating conditions (variable with seasons and load demand) and the ways the RES generation can impact on the work programme of the existing diesel units. The system inertia is a good indicator of the proximity of the system to a hazardous operating point.

For improving, the reliability of the generating system, the next chapters involve suitable control systems able to provide PFC and synthetic IR [66], [74].

Chapter 5

Evaluation of the optimal renewable electricity mix: the adoption of a technical and economic methodology

5.1. Introduction

Starting from the results of the previous chapter, this chapter shows how important is considering stability issues in studies evaluating the optimal renewable energy mix in isolated power systems and, in particular, in small islands. Firstly, a mathematical model is proposed to find the optimal energy mix to satisfy a fixed share of annual electricity production from RES. Commercial technologies are adopted considering the importance of flexible resources for the integration of RES and evaluating technical and economic indicators, such as the LCoE. Initially, a GIS-based model is created through maps and tables with percentages of electricity consumptions covered by local RES, identifying the most critical and suitable areas for the installation of new RES plants [20]. Then, RES potential is considered by modelling some scenarios with Energy PLAN [21], and the trend of the production from RES in a typical Summer and Winter week is evaluated. Finally, the optimal scenario evaluated is verified with regards to the stability issue with some simulation performed in NEPLAN, showing that the penetration of distributed generators based on static converters in small islands can lead to instability if appropriate controls are not implemented.

5.2. Methodology

The proposed methodology is divided into three steps:

- first: the energy mix, composed of solar, wind and sea wave, is chosen, fixing the share of annual electricity production from RES equal to the target established for each island;
- second: a mathematical model is used to find the best energy blend with the lowest LCOE. This parameter, reported in Equation (5.1), represents the minimal selling price for electricity to cover the initial investment cost and the annual operative and maintenance costs of the entire electrical system [80], [81].

$$LCOE * \sum_{i=1}^{n} \frac{E_i}{(1+\tau)^i} = TLCC \tag{5.1}$$

- third: a model of the network with RES is implemented in NEPLAN and analysed in order to check the stability in the presence of static converter-interfaced RES DG.

The Total Life Cycle Cost (TLCC) is the sum of all the costs associated with the selected technology in its entire life, practically, the initial investment and the annual operative and maintenance costs of the system [82]. The term E_i represents the annual electricity production (or saving) from the power plant. Indeed, this parameter is generally referred to as a single technology and is commonly available in the literature [83]. The term τ is the monetary interest rate. In the energy scenario based on RES, considering an expected life equal to 20 years, Equation 5.1 can be adapted into Equation 5.2:

$$LCoE = \frac{\sum_{i=1}^{20} E_f c_f \left(\frac{1+\varepsilon}{1+\tau}\right)^i + C_{r,0} + \sum_{i=1}^{20} \frac{C_{r,A} + C_{f,A}}{(1+\tau)^i}}{\sum_{i=1}^{20} \frac{E_d}{(1+\tau)^i}} \tag{5.2}$$

$$E_f = E_d - \left(P_{sw} h_{e,sw} + P_w h_{e,w} + P_{pv} h_{e,pv}\right)$$
$$C_{r,0} = P_{sw} c_{sw,0} + P_w c_{w,0} + P_{pv} c_{pv,0}$$
$$C_{r,A} = P_{sw} c_{sw,A} + P_w c_{w,A} + P_{pv} c_{pv,A}$$

where:

- ε is the inflation rate for the energy sector;
- E_d represents the annual energy demand;
- E_f represents the expected annual electricity production from the existing power plant to balance the energy demand and electricity production from RES. Consequently, E_f can be expressed as the difference of the annual energy demand and the annual electricity production from sea wave ($P_{sw} h_{e,sw}$), wind ($P_w h_{e,w}$), and solar sources ($P_{pv} h_{e,pv}$). The product of the installed power gives each term from each source (P_{sw}, P_w, P_{pv}) and the annual equivalent working hours ($h_{e,sw}$, $h_{e,w}$, $h_{e,pv}$), i.e., the number of hours per year required to produce the entire annual electricity production if the system works at the rated power. This parameter depends on the chosen technologies and the local climatic conditions;
- $C_{r,0}$ represents the initial investment cost. It is the sum of the initial investment costs for sea wave $P_{sw} c_{sw,0}$, wind $P_w, c_{w,0}$ and solar $P_{pv}, c_{pv,0}$, each one expressed as the product of the installed power and the unitary cost of each technology;
- $C_{r,A}$ represents the annual operative and maintenance cost for the energy mix;
- $C_{f,A}$ represents the annual operative and maintenance cost for the existing diesel generators (except the fuel expenditure).

The solar energy source availability is expressed by the monthly average daily total solar radiation from photovoltaic panels. The annual electricity production is:

$$E_{pv} = \sum_{i=1}^{12} E_{pv,i} = \sum_{i=1}^{12} I_{T,i} S_{pv} \eta_{pv} t_{d,i} \tag{5.3}$$

where $E_{pv,i}$ represents the summing the monthly electricity production, $I_{T,i}$ represents total solar radiation, S_{pv} represents the area of photovoltaic panels, η_{pv} represents the average energy efficiency and $t_{d,i}$ represents the number of days per month. The exploitation of the solar source uses commercial silicon PVP; the selected photovoltaic panel data are given by [84].

The wind energy source can evaluate measuring the wind speed class v_j of annual electricity production. In detail, E_w is discretised in several bins per each month. Therefore, the availability of wind source is expressed indicating for each month the number of hours ($t_{j,i}$) when a wind class is measured.

$$E_w = \sum_{i=1}^{12} E_{w,i} = \sum_{i=1}^{12}\sum_{j=1}^{n} \psi(v_j)\, t_{j,i} \tag{5.3}$$

In detail, the wind speed is discretised in several bins per each month, so the availability of wind source is expressed indicating for each month the number of hours when a wind class is measured. The function $\psi(\mathrm{v})$ defines the power output of the chosen wind turbine, as a function of the wind speed. This relation and other data are available in the datasheet of the turbine builder, as reported in Appendix B [85].

The sea wave energy source by the wave power flux (φ), which is given by [86], i.e. the average power available in a unitary length of a wavefront:

$$\varphi = \frac{\rho g^2}{64\pi} H_s^2 T_e \tag{5.4}$$

introducing the significant wave height (trough to crest) $\mathrm{H_s}$, the energy period $\mathrm{T_e}$, the seawater density ρ. These data are obtained from a measuring campaign, analysing the wave spectrum [87]. The estimation of electrical energy production from E_{sw} is given by:

$$E_{sw} = \sum_{i=1}^{12} E_{sw,i} = \sum_{i=1}^{12} \varphi_i d_C \eta_{sw} \eta_{hy} t_{h,i} \tag{5.5}$$

considering the monthly average sea wave energy flux φ_i, the average electrical efficiency η_{sw} of the device, the equivalent hydraulic diameter d_C of the wave energy converter, the hydraulic efficiency η_{hy} of power take-off and the number of hours in the i-th month $t_{h,i}$. For the exploitation of sea wave, a Wave Energy Converter (WEC), in design step at the laboratories of the Engineering Department of the University of Palermo [88], has been considered.

Figure 5.1 shows the system proposed by the University Palermo, composed of two floating buoys, where the external buoy can move up and down, running the linear generators installed inside the central buoy fixed to the seabed.

The annual equivalent working hours $h_{e,sw}$, $h_{e,w}$, $h_{e,pv}$ are obtained by:

$$h_{e,pv} = \frac{E_{PV}}{P_{pv,rated}} = \frac{\sum_{i=1}^{12} I_{T,i} S_{pv} \eta_{pv} t_{d,i}}{P_{PV,rated}}$$

$$h_{e,w} = \frac{E_w}{P_{w,rated}} = \frac{1}{P_{w,rated}} \sum_{i=1}^{12}\sum_{j=1}^{m} \psi(v_j) t_{j,i} \tag{5.7}$$

$$h_{e,sw} = \frac{E_{sw}}{P_{sw,rated}} = \frac{1}{P_{sw,rated}} \sum_{i=1}^{12} \varphi_i d_C \eta_{sw} \eta_{hy} t_{h,i}$$

The following parameters are considered to study the individuation of the best energy mix for the island from an economic point of view:

- the ratio between the annual electricity production from photovoltaic / RES is a_{pv};

- the ratio between the annual electricity production from G9 and the yearly demand is r;
- the ratio between the annual electricity production from wind and the annual electricity production is a_w.

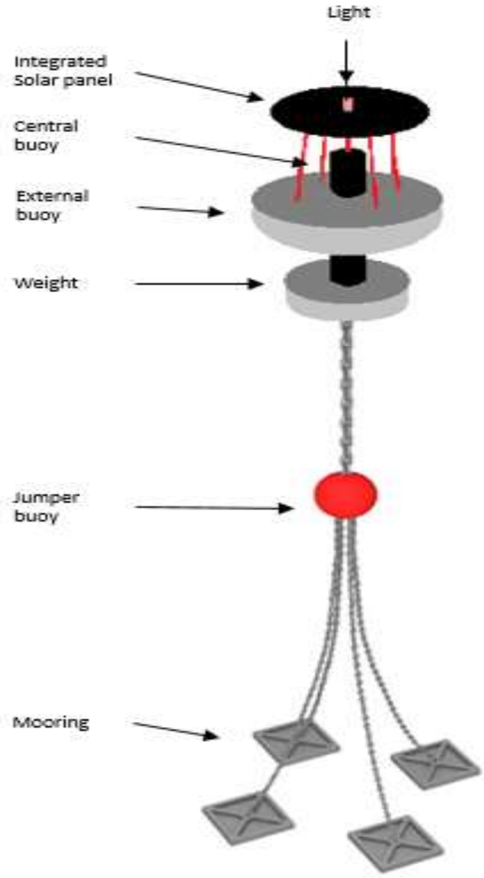

Figure 5.1: External view of the WEC.

Thus, by using the definition of r, a_{pv} and a_w and the equivalent working hours from each RES generator ($h_{e,sw}$, $h_{e,w}$ and $h_{e,pv}$), after few manipulations the LCoE is be finally evaluated by:

$$LCoE = (1-r)\frac{c_f k_1}{k_2} + r\left[\frac{1-a_{pv}-a_w}{h_{e,sw}}\left(\frac{c_{sw,0}}{k_2}+c_{sw,A}\right)+\frac{a_w}{h_{e,w}}\left(\frac{c_{w,0}}{k_2}+c_{w,A}\right)+\frac{a_{pv}}{h_{e,pv}}\left(\frac{c_{pv,0}}{k_2}+c_{pv,A}\right)\right]+\frac{C_{f,A}}{E_d} \tag{5.6}$$

$$k_1 = \sum_{i=1}^{20}\left(\frac{1+\varepsilon}{1+\tau}\right)^i$$

$$k_2 = \sum_{i=1}^{20}\frac{1}{(1+\tau)^i}$$

where:

- ε represents the inflation rate for the energy sector;
- $c_{sw,0}$, $c_{w,0}$, $c_{pv,0}$ represent the inputs of the problem being the specific costs to install;
- $c_{sw,A}$, $c_{w,A}$, $c_{pv,A}$ are the maintenance costs of all RES technologies;
- r, a_{pv} and a_w represent the annual equivalent working hours that can be evaluated only one time, per Equation 5.6; thus, these parameters are considered constant in the optimisation phase.

When fixing the share removable electricity production, two degrees of freedom are observed for the problem (a_{pv}, a_w). Thus, the economic optimisation to find the best energy mix has to be realised. The two degrees of freedom are varied in a discretised way,then the evaluation of LCOE is performed for each condition. It is essential to underline that this parameter uses the estimation of annual electricity production. Since each RES has a different trend during the year, some energy mixes could involve an hourly production trend incompatible with the network's balance. This problem is most significant during Winter when the electricity production from wind and sea wave is maximal and the energy demand minimal. To avoid this condition, the evaluation of LCOE introduces the following constraints on the renewable energy mix:

- each source must produce almost 10% of the total energy in each month to justify the adoption of this energy source;
- the total energy from RES must not exceed a specific ratio z of the monthly electricity demand, to guarantee a minimal electricity production from fossil fuels, compensating the maintenance cost of the existing power plant;
- considering the load profile during a typical summer day (highest energy demand) and winter day lowest energy demand, the difference between electricity production from RES and demand must be positive to balance the electrical grid by using the local power plant, avoiding the requirement of an ESS.

The check of RES production for monthly scale, according to:

$$E_{sw,i} + E_{w,i} + E_{pv,i} \leq zE_{d,i} \tag{5.7}$$

where z represents maximal share, is used to prevent the hourly verification of all possible mixes and reduce the computational burden.

As shown in the flow chart reported in Figure 5.2, the parameter z is evaluated with an iterative approach. It assumes firstly the value of 90% to evaluate the matrix of constrains preliminarily. Overlapping the matrix of constraints to the not constrained LCoE matrix, it is possible to identify the best condition, i.e., the RES mix corresponding to the lowest LCoE. This condition is consequently verified, considering the hourly trends of energy demand and production from RES. If the proposed energy mix exceeds the energy demand in some hours of the day, the parameter z is reduced, and consequently, the matrix of constrains is calculated again and overlapped on the not constrained LCoE matrix to find the new best energy mix. After a few iterations, the best energy is finally obtained, verifying the hourly compatibility with the local energy demand.

After the selection of the best energy mix, the grid stability analysis is finally performed.

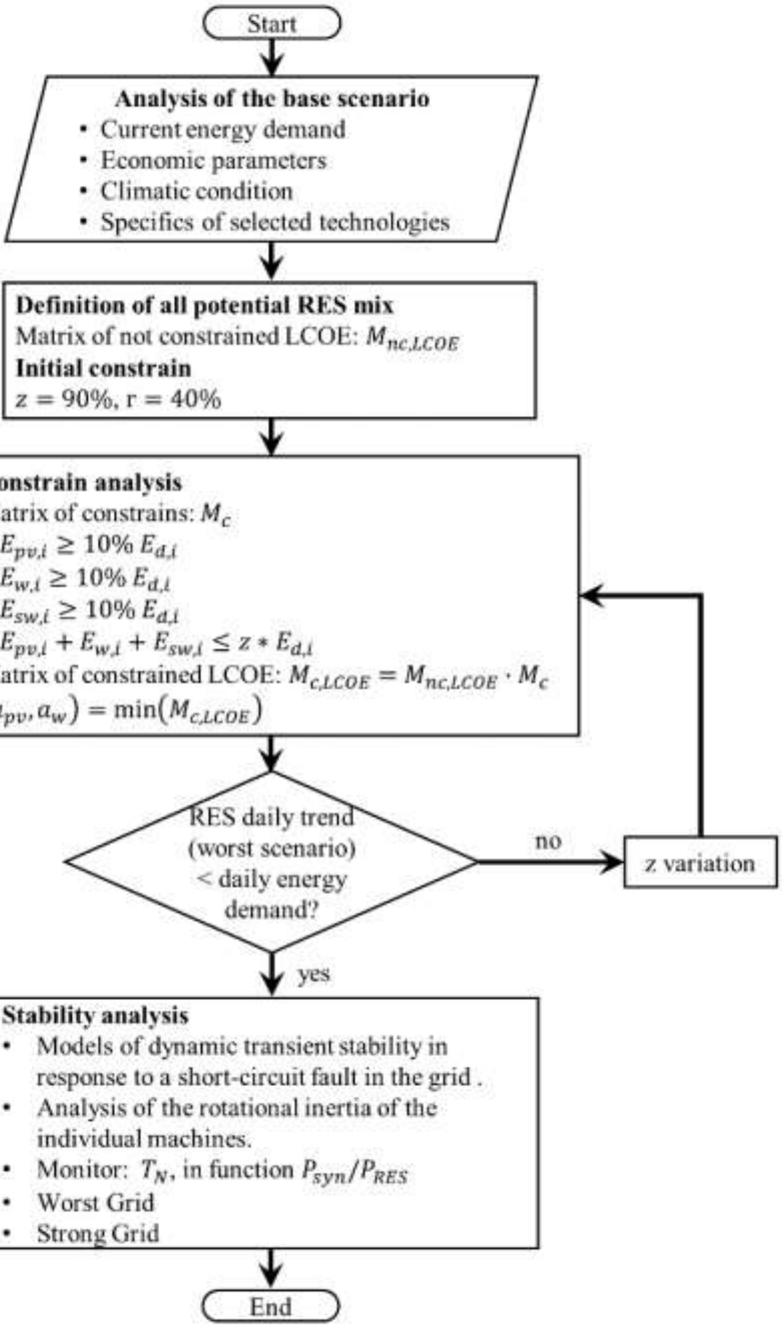

Figure 5.2. Flow chart of the methodology.

5.3. Minimization of LCOE

The RES mix are assessed by the economic parameter LCoE. The function shows three degrees of freedom: the share of electricity production from the RES mix r concerning the total energy demand, the Ratio of electricity production from photovoltaic panels a_{pv} and wind turbines a_w concerning RES production. Climatic data are evaluated by using specific GIS tools. For this analysis, only Lampedusa island is considered, as an example, since Pantelleria island has similar characteristics, assuming an annual electrical energy consumption equal to 36.8 GWh [84]. Table A.3 of Appendix A report all data.

Figure 5.3 shows the annual trend of the energy mix, considering: 9 wind speed classes by wind source (data are based on a specific weather model having a resolution of 30 km [89]).

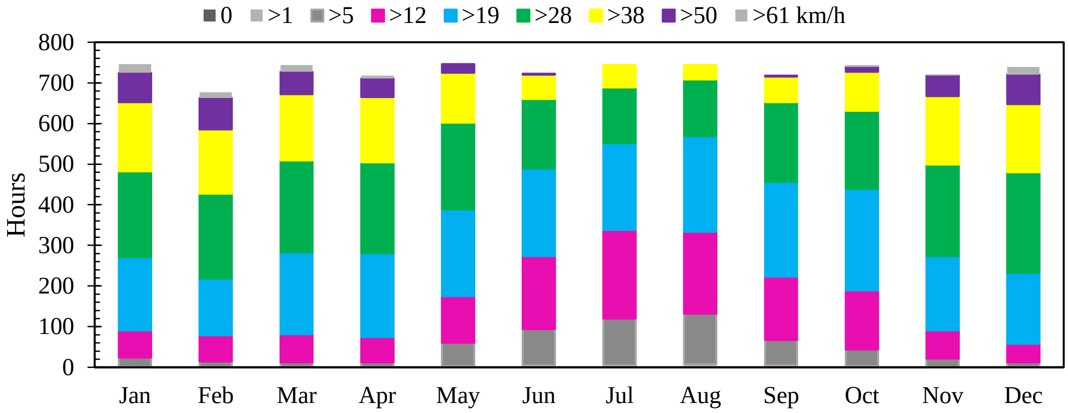

Figure 5.3. Availability of wind source by wind speed classes.

Figure 5.4 shows the sea wave-energy source, the monthly average power flux trend and the solar source is represented by the monthly average daily solar radiation on the horizontal surface and a tilted surface (31°)[90].

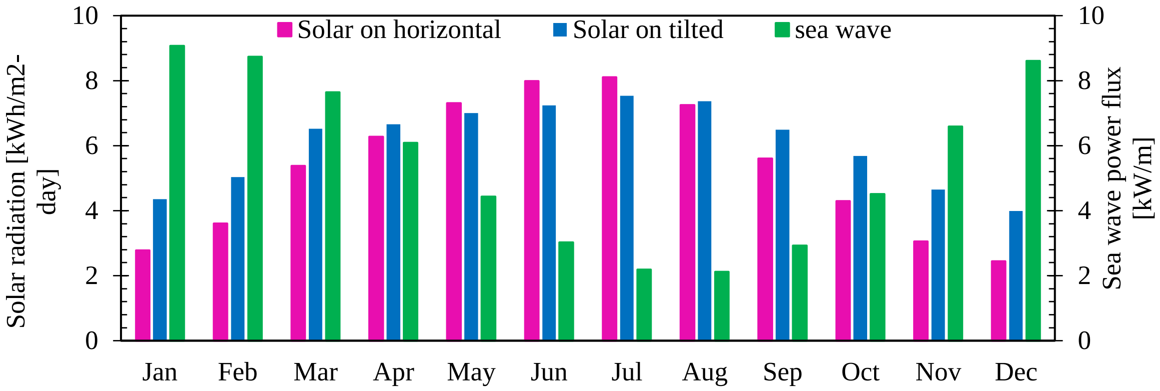

Figure 5.4. Solar radiation on the horizontal and tilted surface (31°) and sea wave power flux.

The mathematical model of CPP splits the annual costs into two parts: a term related to the fuel consumption to produce energy of each source and a term similar to fixed expenditure (worker salaries, maintenance, *etc.*).

Assuming a constant trend from Figure 3.3, the evaluation of the average price for fuel consumption has been done as the weighted average of the monthly average price of oil with a low concentration of sulfur (less than 1%) published by the Italian Ministry of Economic Development [84]. The total income of the local producer is given by the product of the annual electricity production and the total selling price of energy. Thus, the fixed costs are the difference between the total income and the estimated fuel consumption expenditure. The cost of electricity production using traditional generators is assumed equal to the sum of National Unique Price NUP [91] and the incentive established by the Italian Authority for Energy ARERA [92].

From [93] about RES, the unitary cost for the purchase and installation and the maintenance operations of each RES technology.

About sea wave, the economic parameters are obtained from the study in reference [94]. The discount rate for the energy sector has been evaluated, considering the entire data bank (from January 1996 to November 2019) on the monthly average price of oil with a low concentration of sulfur [38]. About the discount rate for money, data are available in the literature [95], [96].

Considering the climatic data by Section 5.3, the mathematical model assumes a RES share set to 40%. The remaining two free degrees of freedom are varied in a discretised way from 0 to 100%, as shown in Table 5.1, obtaining the LCoE as a function of the share of solar and wind production.

Table 5.1. LCoE (€/MWh) as a function of photovoltaic and wind Ratio (%) for 40%.

	a_{pv}																				
a_w	0	5	10	15	20	25	30	35	40	45	50	55	60	65	70	75	80	85	90	95	100
0	304	302	300	298	296	294	292	290	288	286	283	281	279	277	275	273	271	269	267	265	263
5	302	300	297	295	293	291	289	287	285	283	281	279	277	275	273	271	269	267	265	262	
10	299	297	295	293	291	289	287	285	283	281	279	276	274	272	270	268	266	264	262		
15	297	295	293	291	288	286	284	282	280	278	276	274	272	270	268	266	264	262			
20	294	292	290	288	286	284	282	280	278	276	274	272	270	267	265	263	261				
25	292	290	288	286	284	281	279	277	275	273	271	269	267	265	263	261					
30	289	287	285	283	281	279	277	275	273	271	269	267	265	263	260						
35	287	285	283	281	279	277	275	272	270	268	266	264	262	260							
40	284	282	280	278	276	274	272	270	268	266	264	262	260								
45	282	280	278	276	274	272	270	268	265	263	261	259									
50	279	277	275	273	271	269	267	265	263	261	259										
55	277	275	273	271	269	267	265	263	261	259											
60	275	273	270	268	266	264	262	260	258												
65	272	270	268	266	264	262	260	258													
70	270	268	266	263	261	259	257														
75	267	265	263	261	259	257															
80	265	263	261	259	257																
85	262	260	258	256																	
90	260	258	256																		
95	257	255																			
100	255																				

Consequently, Table 5.1 reveals the following features:

- in the case of not constrained matrix, LCoE assumes the lowest value using only the renewable energy source with high equivalent working hours and low Capex and Opex (see $a_w = 100\%$);
- sea wave is a technology in the development step. The initial investment is higher in comparison with the other two sources. Consequently, in the case $a_w = 0\%$ and $a_{pv} = 0\%$ LCoE assumes the highest value;
- the most considerable part of the amounts reported in Table 5.1 is lower than the equivalent cost for the electricity production from fossil fuel (see c_f in Appendix Table). This aspect means that the adoption of different RES mixes can reduce the sum of all costs to produce electricity in small islands in comparison with the as-is scenario;
- the change of operative and maintenance cost of the electricity production from fossil fuels does not intervene in the optimal energy mix election.

The mathematical model introduces several constraints:

- Each RES must annually produce at least 10% of the total electricity production from RES;
- The monthly share of electricity production from RES must not exceed the parameter z, to guarantee minimal electricity production from the existing power plant and balance the electrical grid. At the same time, z is calibrated to avoid the case that electricity production exceeds the electricity demand to prevent energy storage installation.

The remaining two free degrees of freedom are varied in a discretised way from 0 to 100%, as shown in **¡Error! No se encuentra el origen de la referencia.**5.2, obtaining the LCoE as a function of the share of solar and wind production.

Table 5.2. LCoE (€/MWh) as a function of photovoltaic and wind Ratio (%) for 40%.

	a_{pv}																				
a_w	0	5	10	15	20	25	30	35	40	45	50	55	60	65	70	75	80	85	90	95	100
0	0	0	0	0	0	0	0	0	0	0	0	0	0	0	0	0	0	0	0	0	0
5	0	0	0	0	0	0	0	0	0	0	0	0	0	0	0	0	0	0	0	0	
10	0	0	0	0	0	0	0	0	0	0	1	0	0	0	0	0	0	0	0		
15	0	0	0	0	0	0	0	0	0	1	1	0	0	0	0	0	0	0			
20	0	0	0	0	0	0	0	0	0	1	0	0	0	0	0	0	0				
25	0	0	0	0	0	0	0	0	1	1	0	0	0	0	0	0					
30	0	0	0	0	0	0	0	1	1	1	0	0	0	0	0						
35	0	0	0	0	0	0	0	1	1	0	0	0	0	0							
40	0	0	0	0	0	0	1	1	1	0	0	0	0								
45	0	0	0	0	0	1	1	1	0	0	0	0									
50	0	0	0	0	0	1	1	1	0	0	0										
55	0	0	0	0	0	1	1	0	0	0											
60	0	0	0	0	1	1	1	0	0												
65	0	0	0	0	1	1	0	0													
70	0	0	0	0	1	0	0														
75	0	0	0	0	0	0															
80	0	0	0	0	0																
85	0	0	0	0																	
90	0	0	0																		
95	0	0																			
100	0																				

The worst renewable energy mix scenario produces the maximal potential energy output: photovoltaic panels according to the hourly solar radiation, wind and sea wave at rated power. According to this analysis, z is evaluated equally to 0.53. Table 5.2 shows the RES mixes that satisfy all the conditions above reported, using a Boolean representation. The value one is referred to as the energy mixes that are compatible with all constraints above noted. Thus, multiplying the values reported in Table 5.1 and Table 5.2, the constrained LCoE matrix is finally obtained (see Table 5.3).

Table 5.3. Constrained LCoE matrix for 40.

	a_{pv}																				
a_w	0	5	10	15	20	25	30	35	40	45	50	55	60	65	70	75	80	85	90	95	100
0																					
5																					
10											279										
15										278	276										
20										276											
25									275	273											
30								275	273	271											
35								272	270												
40							272	270	268												
45						272	270	268													
50						269	267	265													
55						267	265														
60					266	264	262														
65					264	262															
70					261																
75																					
80																					
85																					
90																					
95																					
100																					

As shown in Table 5.3, according to all constraints, the best energy mix to cover the 40% of the annual electricity demand is composed by 70% wind, 20% solar and 10% sea wave. Consequently, the power to install for each source, considering the parameters already described above.

$$P_w = rE_d \frac{a_w}{h_{e,w}} \qquad P_{pv} = rE_d \frac{a_{pv}}{h_{e,pv}} \qquad P_{sw} = rE_d \frac{1 - a_w - a_{pv}}{h_{e,sw}} \tag{5.8}$$

Table 5.4: Proposal of the energy mix for AG.

Reference	Solar	Wind	Sea wave
Power to be installed [kW]	1509	2100	640
Rated power of the device	3	60	80
n. device	503	35	8
Annual electricity production [MWh/year]	2947.4	10463.4	1548.5

To replace the 40% of the current electricity demand, the best energy mix from an economic point of view requires the installation of 1509 kW of photovoltaic panels (subdivided into 503 small roof-integrated plants), 2100 kW of wind turbines (35 wind plants) and 640 kW of wave energy converters (8 devices). In this way, the estimated annual electricity production is equal to 2947.4 MWh/year for solar panels, 10463.4 MWh/year for wind turbines analysed and 1548.5 MWh/y for sea WECs.

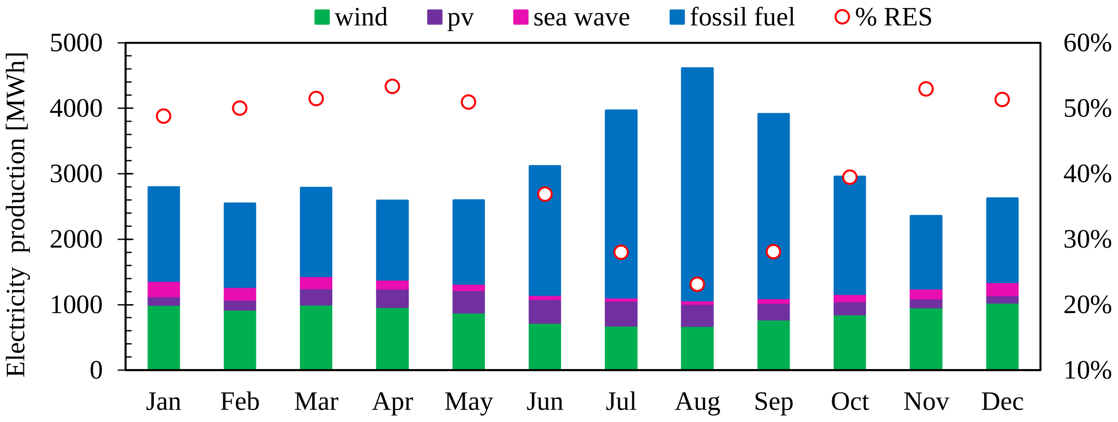

Figure 5.5. Electricity demand and potential renewable electricity production.

The energy mix can reduce the energy price to 0.260 €/kWh from the current value equal to 0.282 €/kWh (data of 2015). An avoided annual expenditure in all Italian energy bill equivalent to0.797million euros (a reduction of 7.67 % of the current spending) is estimated thanks to the decrease in electricity production from fossil fuels.

From an environmental point of view, the fuel consumption is reduced by 3170 tons of oil, corresponding to an avoided emission of 9963 tons of CO_2 per year.

Since sea wave technology is still prototypical, an alternative simulation was also investigated, removing the constraint on the minimal electricity production from this energy source. In this case, the proposed energy mix includes 40 wind turbines, producing the 80% of RES production, and 503 PVP (same value of the previous simulation); therefore, the entire sea wave electricity production should be entrusted to wind turbines. The same environmental results could be achieved. From an economic point of view, the annual avoided expenditure is equal to 0.973 million euros, due to the lower investment to accomplish this energy mix. The LCoE is consequently reduced to 0.255 €/kWh.

However, both scenarios are almost equivalent if the grid stability is investigated. Thus, although the installation of sea wave energy converters represents a suboptimal solution from an economic point of view, the first energy mix is considered in the following Section to obtain useful results for a potential installation of first pilot plants.

5.4. Grid stability analysis

Power systems security is based on frequency stability concerning the inertia and kinetic energy variation of the synchronous area for each typical hour during the year. Two scenarios are verified in this section considering two different hourly production trends from RES during a typical week in summer and winter, starting from the previous section's results. The transient stability is analyzed considering an imbalance due to the sudden load lack following a short circuit occurring at bus 65 located two kilometers from the power plant (See Figure A.1). The fault occurs at the simulation time “1 second”. The procedure performed for the study is described below:

- The typical load profiles are obtained according to two different contributions from RES defined in Scenario A and Scenario B below explained;
- For each scenario, typical summer and winter weeks are investigated, to evaluate the power system inertia at each hour, considering the contribution from RES. The inertia constant of the power system in operation is determined according to Equation (2.2). To evaluate the number of active generators, the real daily operating plan of the diesel engines provided by the utility is considered;
- Based on Equation (2.2), the hours corresponding to the maximum and minimum inertia constants of the power system are found for the winter and summer weeks. For those hours, the non-synchronous penetration level (NSPL), defined as the measure of the non-synchronous generation for the instantaneous simulated scenarios time [97], expressed in percentage according to Equation (5.11):

$$NSPL = \frac{P_w + P_{pv} + P_{sw}}{P_w + P_{pv} + P_{sw} + P_{syn}} \tag{5.91}$$

where P_{syn} is the power produced by synchronous generators.

- As introduced before, the fault is simulated at the time step $t = 1s$ in the hours when the power system inertia is maximum and minimum.

The two scenarios considered in the analysis are below reported.

Scenario A or Worst Scenario. This case study models the worst condition for the local electrical grid. The hourly electricity production trend from RES defined as P_{res} is obtained, assuming sea wave and wind power productions equal to their rated power for every hour, while PV plants produce according to the daily trend of solar radiation. The parameters considered for Scenario A are represented in three events with different penetrations of RES production to the power system:

- Event A0: P_{res} is 100% in service for every hour;

- Event A1: P_{res} is 88% in service for every hour, with the condition that must participate in the electricity production during each hour, at least one synchronous generator;
- Event A2: P_{res} is 88% in service for every hour, with the condition must participate in the electricity production during each hour as the minimum of two active synchronous generators.

The comparison between the typical load profiles (delivered by the local energy producer) and the RES penetration according to each event on the island every hour are reported in Figure 5.6.

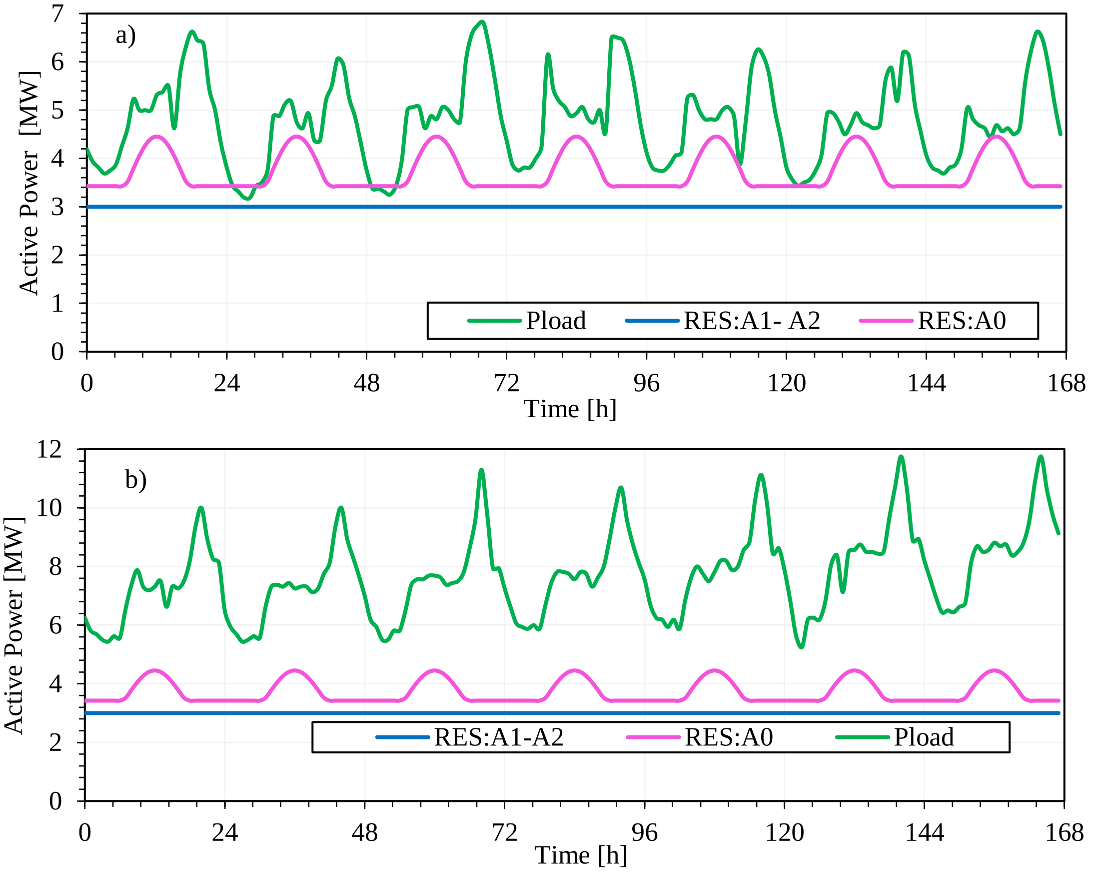

Figure 5.6. Scenario A: Typical load profile with RES penetration:
a) summer week and b) winter week.

Scenario B or Probabilistic scenario. This case study introduces a more realistic condition, evaluating the hourly energy producibility by considering the data collected in two different years about sea wave, wind and solar radiation, and assuming each source the condition that corresponds to the maximal electricity production. Scenario B use three Events with different penetrations of RES electricity production:

- Event B0: P_{res} is 100% in service every hour;
- Event B1: $P_{res} \leq 3MVA$ with the condition that must participate in the electricity production during each hour, at least one synchronous generator;
- Event B2: $P_{res} \leq 3MVA$ with the condition that must participate in the electricity production during each hour as a minimum of two active SGs.

Figure 5.7 shows the comparison between the typical load profiles (delivered by the local energy producer) and the RES penetration according to each Event on the island every hour.

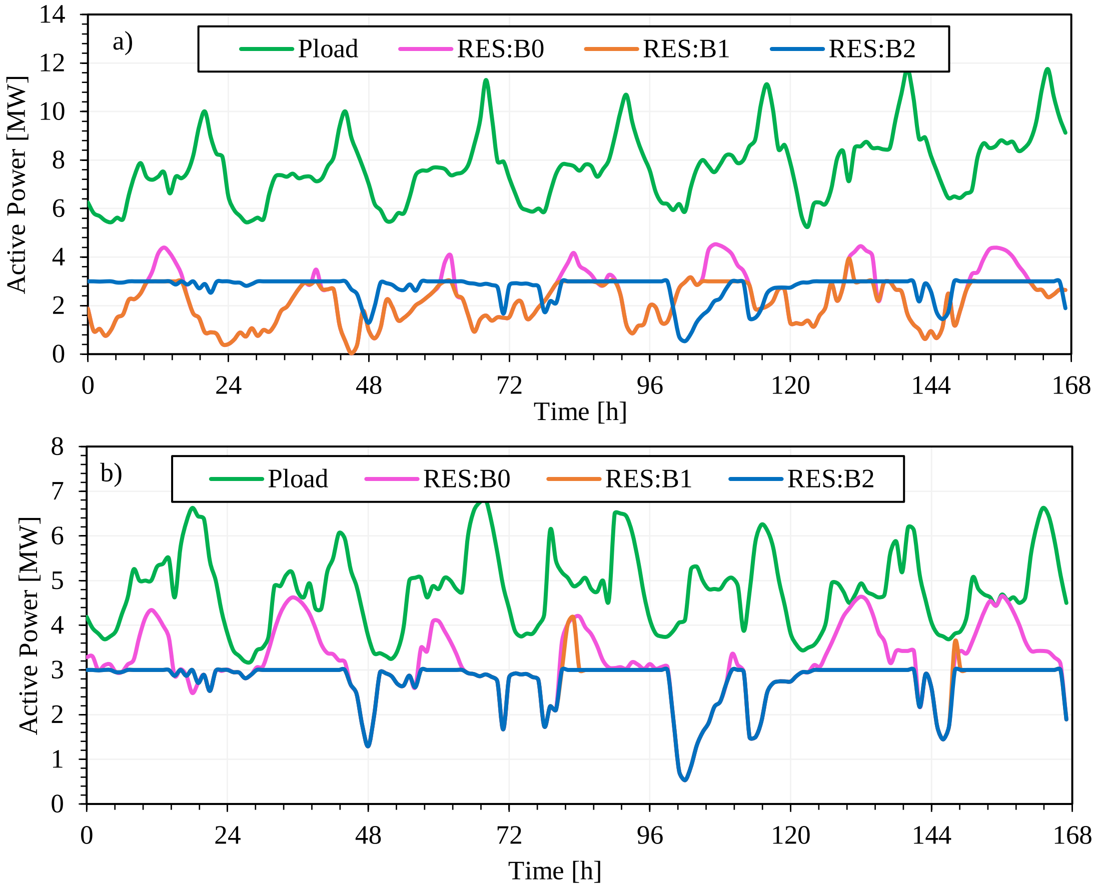

Figure 5.7. Scenario B: Typical load profile with RES penetration:
a) summer week and b) winter week.

Considering the energy produced by RES and the load profiles in Figures 5.6 and 5.7, the inertia of the system is evaluated hour by hour for the two typical weeks as shows Figure 5.815.8.
Figure 5.8 shows how the system inertia constant varies along a Summer and Winter week. In particular, the system inertia continually decreases since the production from RES increases and the number of SGs in operation decreases. Besides the number of synchronous generators in operation for each hour, the sum of the rated apparent powers of the synchronous generators influences the value of the inertia.
The trends in Figure 5.8 show that IR is between 0-2.75 s. This means that in some situations, characterized by a high share of renewables, all synchronous generators are disconnected from the grid, and the inertia goes to zero. This happens, in particular, when renewables are 100% in service every hour.
Table 5.5 reports 24 different power system states corresponding to the minimum and maximum inertia of the system, evaluated according to Equation (5.10). Each state is identified by a code, whose structure is the following

$$\#code = x_1x_2.x_3.x_4$$

where:
$\boldsymbol{x_1}$ indicated the scenario (A or B)
$\boldsymbol{x_2}$ indicates the event (0, 1, 2)
$\boldsymbol{x_3}$ indicates the value of the inertia constant of the system (1 for minimum inertia; 2 for maximum inertia)
$\boldsymbol{x_4}$ indicates the season (1 for summer and 2 for winter).

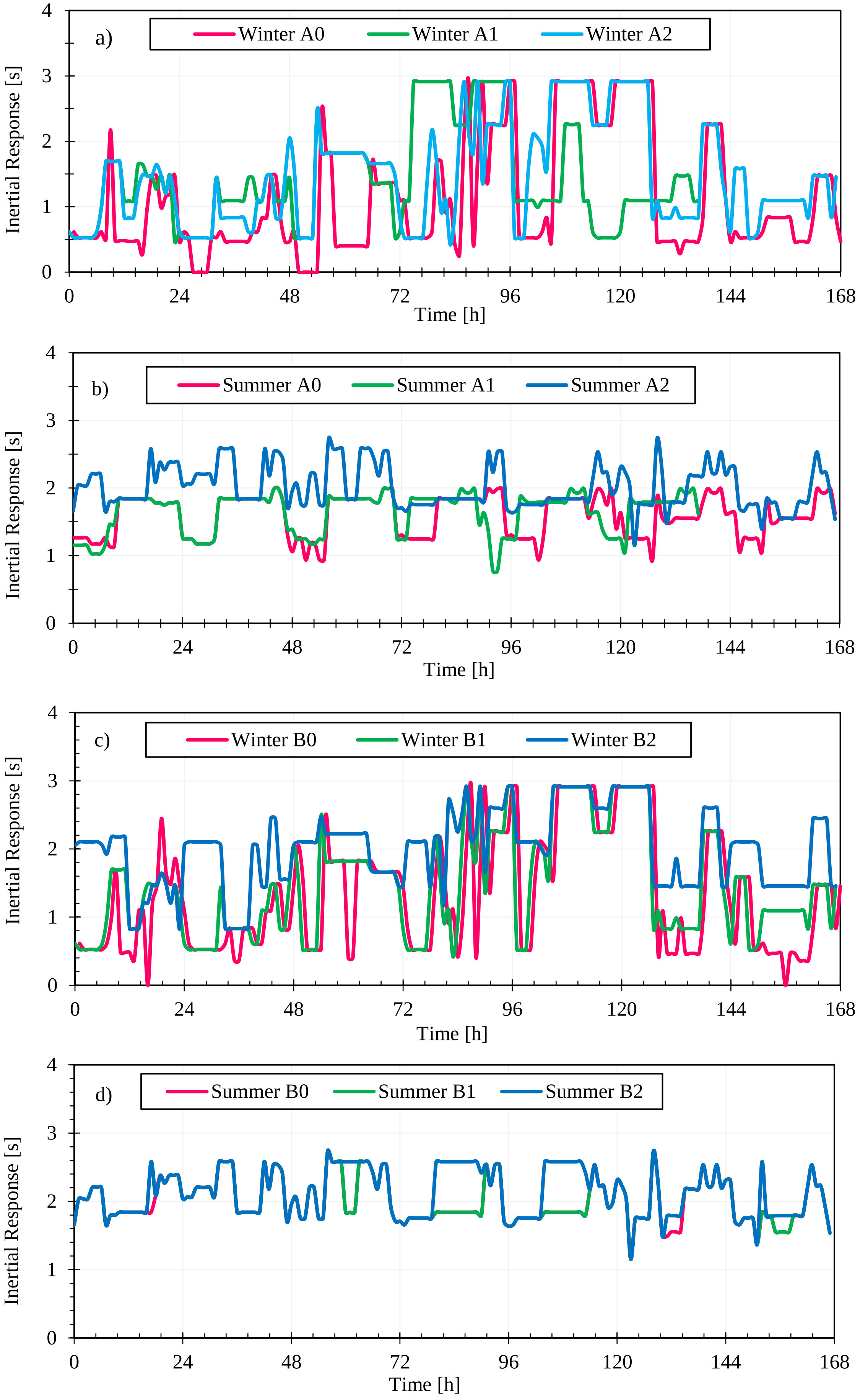
a)
Winter A0
Winter A1
Winter A2
Inertial Response [s]
0
1
2
3
4
Time [h]
0
24
48
72
96
120
144
168
b)
Summer A0
Summer A1
Summer A2
Inertial Response [s]
Time [h]
c)
Winter B0
Winter B1
Winter B2
Inertial Response [s]
Time [h]
d)
Summer B0
Summer B1
Summer B2
Inertial Response [s]
Time [h]

Figure 5.81. Trend inertial response in RES presence: (a) Scenario A, Winter; (b) Scenario A, Summer; (c) Scenario B, Winter; (d) Scenario B, Summer

For the 24 cases in Table 5.5, a dynamic stability analysis is performed by NEPLAN. The disturbance occurs at $t = 1s$, and the observation window is set equal to 10 seconds. Figure 5.9 shows grid frequency oscillation for the 24 Events from Table 5.5.

Table 5.5. Simulated Events overview.

Simulation	Active Generators	NSPL	T_N [s]
A0.1.1	G4	58%	0.54
A0.1.2	-	100%	0.00
A0.2.1	G4-G8	43%	1.48
A0.2.2	G8	100%	2.34
A1.1.1	G7	54%	0.57
A1.1.2	G3	74%	0.30
A1.2.1	G4-G8	38%	1.48
A1.2.2	G8	87%	2.34
A2.1.1	G3-G7	45%	0.67
A2.1.2	G1	20%	0.92
A2.2.1	G7-G8	45%	1.70
A2.2.2	G1-G8	59%	2.75
B0.1.1	G5-G7	26%	0.91
B0.1.2	-	100%	0.00
B0.2.1	G4-G7-G8	13%	1.71
B0.2.2	G8	86%	2.34
B1.1.1	G5-G7	26%	0.91
B1.1.2	G3	75%	0.31
B1.2.1	G4-G7-G8	13%	1.71
B1.2.2	G8	34%	1.29
B2.1.1	G5-G7	26%	0.92
B2.1.2	G3-G5	55%	0.51
B2.2.1	G4-G7-G8	13%	1.71
B2.2.2	G1-G8	61%	2.75

The trends in Figure 5.9. show that:

- in all cases, the grid frequency shows a typical trend occurring in the case of load loss. In 22 out of 24 cases the frequency initially increases, reaching a peak in less than one second due to the unbalance between generation and load. Then, it decreases again reaching a new steady-state value due to the action of the speed regulators of the diesel generators;
- the frequency has more significant oscillations when RES contribution is greater than 28% of the synchronous generation, and only one active synchronous generator is working. This is mainly due to lower values of both the system inertia and the primary regulation reserve of the generating systems depending only on the synchronous generators;
- in 22 out of 24 cases, the system reaches a new stable condition in less than 10 seconds, therefore in a time interval totally compatible with the grid code. The new conditions area far from the upper-frequency limit allowed for the isolated grid (51.5 Hz);

- the system is stable in 22 cases, with limited deviation from the rated frequency, while the upper limit frequency relays (set to 51.5 Hz) detach the synchronous generators in two cases: A0.1.2, B0.1.2.

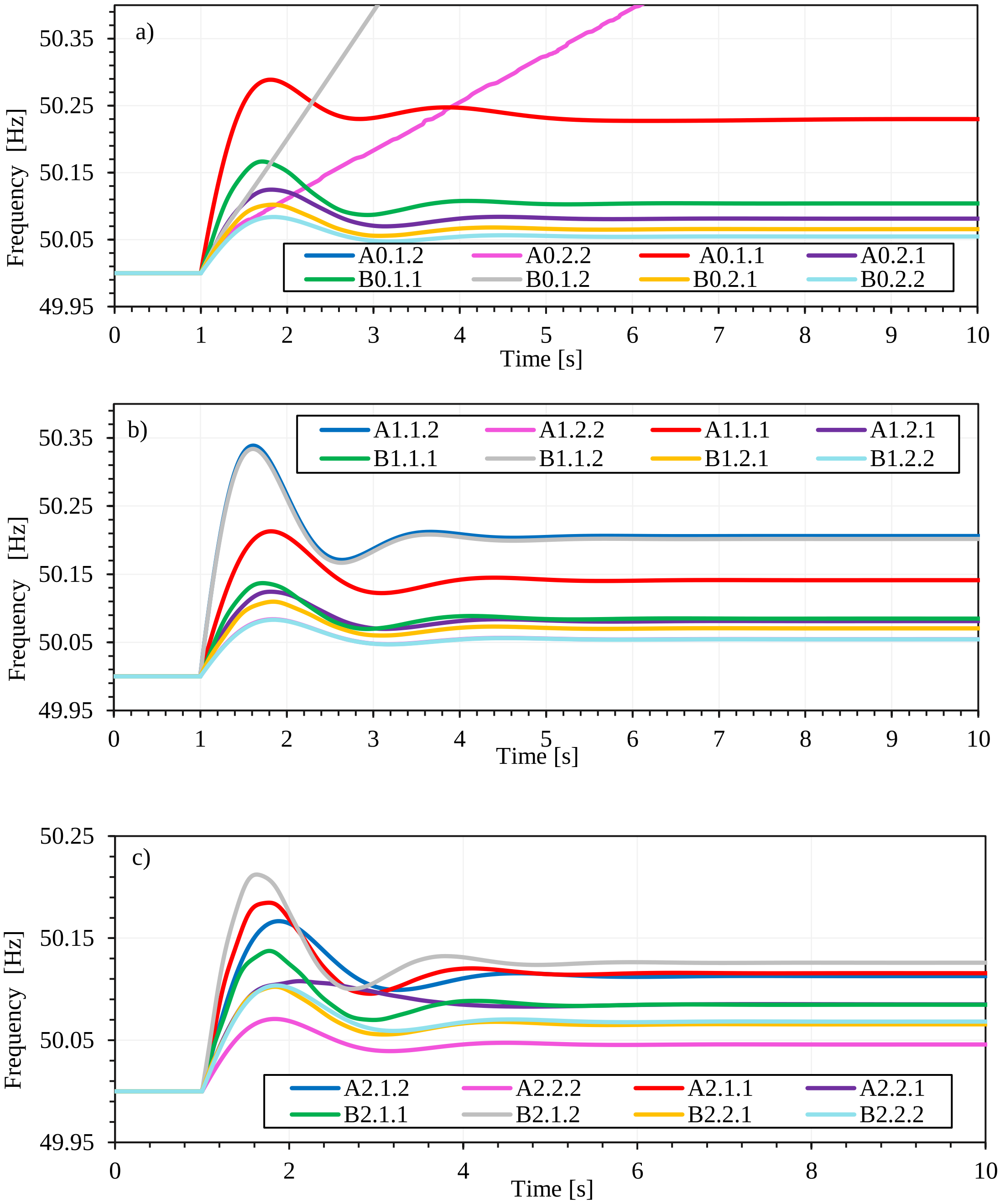

Figure 5.9. Grid frequency in the case of 3-phase short-circuit in the grid: a) Scenarios A0 and B0, b) Scenarios A1 and B1, and c) Scenarios A2 and B2.

For a further analysis of the dynamic stability issue, the RoCof is introduced, according to Equation 5.12:

$$RoCoF = \left.\frac{df}{dt}\right|_{t=0+} = \frac{f_o P_k}{2\sum_{i=1}^{n} H_i \, . \, A_{n,SG,i}} \tag{5.12}$$

where f_o is the rated frequency and P_k represents the power disturbance in the grid (in the examined case, the detachment of loads due to the 3-phase short-circuit). Although in Lampedusa RoCoF protections are not present, the analysis is presented for its theoretical value.
The analysis gave the following results:

- number of Events with RoCoF below 2%: 5;
- number of Events with RoCoF between 2% and 3%: 6;
- the number of Events with RoCoF exceeding 3% (Maximum limit from ENTSO-E, 2017): 13.

Therefore, 22 of the examined cases are acceptable from the point of view of grid stability. In the presence of RoCoF protections, 13 of the contested cases should be further analysed to ensure that, in every possible disturbance event, the system could maintain its stability considering the electricity production from RES in the scenarios above investigated without the intervention of the RoCoF relays.

5.5. Conclusion

A mathematical model has been introduced to investigate a feasible energy mix to supply small islands, considering solar, wind and sea wave sources.
From the environmental point of view, the installation of RES can avoid the emission of 9960 tons of CO_2/year and the consumption of 3170 tons of diesel per year. The main limitations to increase furthermore the RES production are related to the seasonal and daily variation of the electricity demand and production.
Since PV plants and modern wind turbine generators are connected through power converters, they do not offer a natural inertial response. This condition can lead to instability issues, thus particular measures for avoiding power blackout must be implemented. For example, power storage units can be installed both for increasing the RES share and, thanks to specific advanced controls (synthetic inertia, fast frequency regulation and so on) for injecting/absorbing power in the grid and compensating generation of load imbalances (These will be examined in chapters 6 to 8).

Chapter 6

VSC control strategies to allow high penetration RES

6.1. Introduction

The presence of unpredictable RES-based generators in the grid poses many problems like the more difficult generation-load balancing and frequency instability. Due to the irregular and uncertain production from solar and wind sources, a grid having a high penetration of these sources can be exposed to sudden changes of active and reactive power flows [40]. Moreover, in the presence of a generation-load unbalance, being lower the system inertia and kinetic energy, system stability is threatened.

To limit these issues, it is necessary to introduce proper control structures for managing inverter-interfaced RES in order to provide ancillary services to the power system. Fast Frequency Response (FFR) and Virtual Inertia (VI) are the most famous among these services. The two controls are usually applied to grid-following converters to support the grid in a fast way during unbalances. Nevertheless, other control structures are proposed in the literature. In this thesis, the inverter is assumed to be a Voltage Source Converter (VSC) where the control topology plays an essential role in its use in the isolated grid. Three control structure are chosen and compared: a classical Cascaded Current Control (CCC) [98], a Virtual Synchronous Machine (VSM) control and, finally, a VSM with Current Control (CC) and Reference Control (RC). The aim of this chapter is to evaluate the VSC with various internal control strategies for different values of the Short Circuit Ratio (SCR) to study both cases of the weak and robust grid.

6.2. Model of the system

Figure 6.1 shows a single-bus model of the power system used in the following to compare the behaviour of a VSC with VSM (converter E-S.1) and CCC control (converter E-S.2) [43]. The VSC is connected to the Point of Common Coupling (PCC) through an RL-filter, composed by a resistance R_f and an inductance L_f, and regulates the PCC voltage within the specified limits by providing the required reactive power support. The RL-filter inductance is 0.1 p.u. while the resistance is 0.01 p.u.

The ideal grid is an AC-voltage generator $V_{g.}$ (infinite bus) connected to the PCC by a grid impedance Z_g modelled by a resistance R_g and an inductance L_g The controllers have as main goal to create AC-voltage V_{vsc} through internal control loops. E-S.1 uses current feedback control using coordinate transformation while E-S.2 uses a control that provides VI and damping.

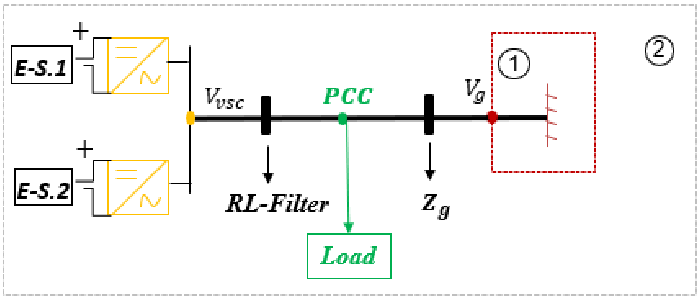

Figure 6.1. Model of the power system.

The SCR expresses the rate between the grid short circuit power S_{sc} and the VSC power S_{sc}:

$$SCR = \frac{S_{sc}}{S_{vsc}} \tag{6.1}$$

$$S_{sc} = \frac{V_g^2}{Z_g}$$

The SCR is inversely proportional to Z_g, if the SCR value is low, the grid is weak. Therefore, varying the SCR value from 1 to 10 it is possible to analyze the impact of Z_g passing from weak to strong grids (Table 6.1).

Table 6.1. Z_g for varying SCR.

SCR	L_g [H]	R_g [Ω]
1	0.0001	0.041
3	0.0003	0.122
5	0.0005	0.204
7	0.0008	0.286
10	0.00108	0.408

6.3. CCC structure

The structure of a cascaded loop shows the integration of an inner and an outer [99]. According to Figure 6.2, CCC_1 represents the traditional CC feedback that regulates the three-phase voltages through the transformation of coordinates. CCC_2 represents an external loop that uses CCC_1 as its actuator. These internal controls are independent of each other but sequentially linked by the frequency-domain analysis. C_0 and C are the input and output of the system. Finally, V_0 and V_c are compensating internal ties. The purpose of the CCC split control technique must ensure that CCC_1 has greater stability than CCC_2. CCC_2 must respond faster that *CCC₁*, which means that it has smaller bandwidth [47], [100], [101].

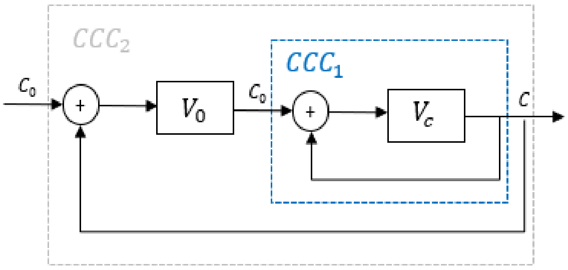

Figure 6.2. CCC block diagram.

The characteristics of CCC are:

- the power system quickly stabilises and has fact response from internal loops in steady-state;
- CCC does not emulate inertia and does not have the capability of regulating voltage;
- the outer loop bandwidth should be smaller than the inner loop's because the inner loop must reach the steady-state more rapidly;
- CCC allows overcurrent protections.

Figure 6.3 shows the proposed overall control scheme for the CCC. In Figure 6.3 are shown three controllers for generating a three-phase voltage $V_{vsc(abc)}$, which are:

- a Phase-Locked Loop (PLL) to track the grid voltage angle θ_{pll} through V_{pcc};
- a CC block used to protect the converter from overcurrent;
- an RC block used to obtain the CC input and coordinate the transformation abc/dq and dq/abc.

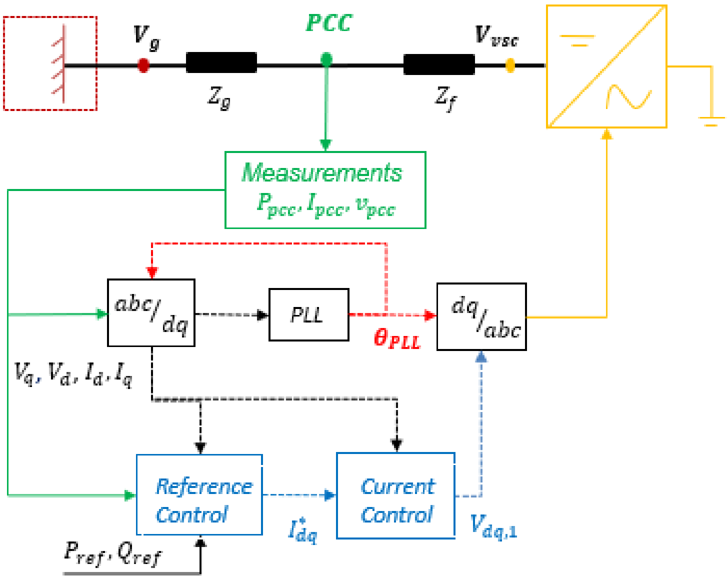

Figure 6.3. The CCC scheme.

The control needs the measurement of power, current and voltage at the PCC (P_{pcc} , I_{pcc}, V_{pcc}). Current and voltage at the PCC are the input for the block that performs the abc/dq transformation. The transformation blocks abc/dq and dq/abc use the angle θ_{pll} for generating I_{dq} and V_{dq}, which are the inputs of the CC and RC controllers. Moreover, P_{pcc} is used as an input of RC. V and P_{ref} are the reference signals for voltage and active power.

CC is described by the following equation [102]:

$$V_{vsc}^{dq*} = V_{pcc}^{dq} + CC \cdot I_{dq} + G_c \cdot \left(I_{dq}^{*} - I_{dq}\right) \tag{6.1}$$

where V_{vsc}^{dq*} represents the reference signal for VSC voltage in dq coordinates, V_{pcc}^{dq} represents the PCC voltage in dq coordinates, CC represents decoupling terms expressed as $\pm\omega_0 L_f I_{dq}$ and G_c is the transfer function of a PI controller with proportional gain $k_{p,C} = \propto_{cc} L_f$ and integral gain $k_{i,C} = \propto_{cc} R_f$, where α_{cc} represents the CCC bandwidth. The integral gain reduces the steady-state error while the proportional gain is associated with the ripple. By tuning these two parameters, excellent dynamic performance can be achieved [103], [104].

A method for the tuning of $\propto_{cc}$ is presented in [49]. In Figure 6.5 the results of some simulations performed in PSCad environment for Lampedusa are shown for $\propto_{cc}$ assuming the values of 1215, 607 and 304 rad/s. An active power step of 0.7 p.u. at the instant t = 0.5 s is considered in Figure 6.5 a) and a voltage step of 0.02 p.u. is considered in Figure 6.5 b).

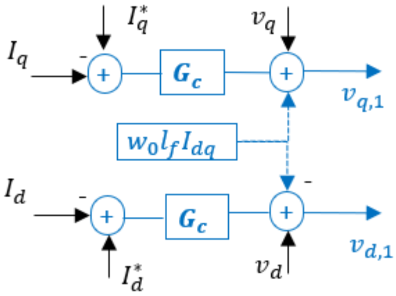

Figure 6.4. CC block diagram.

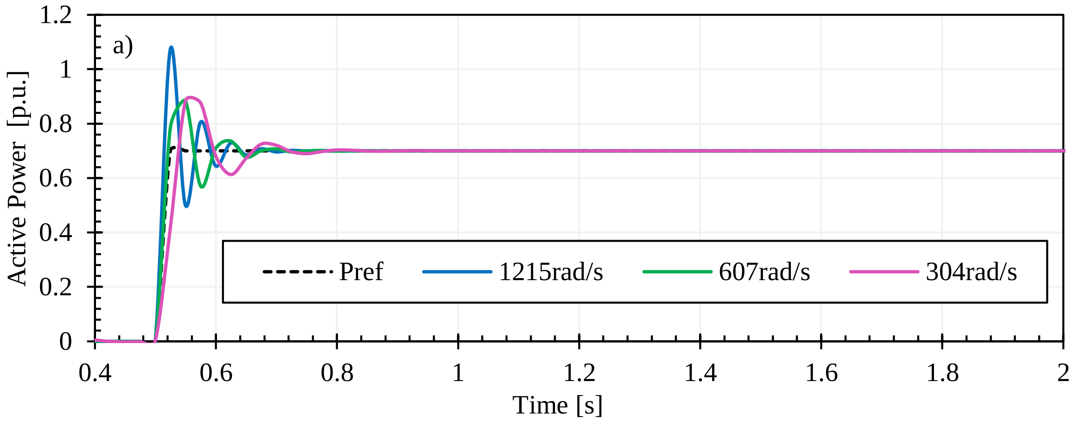

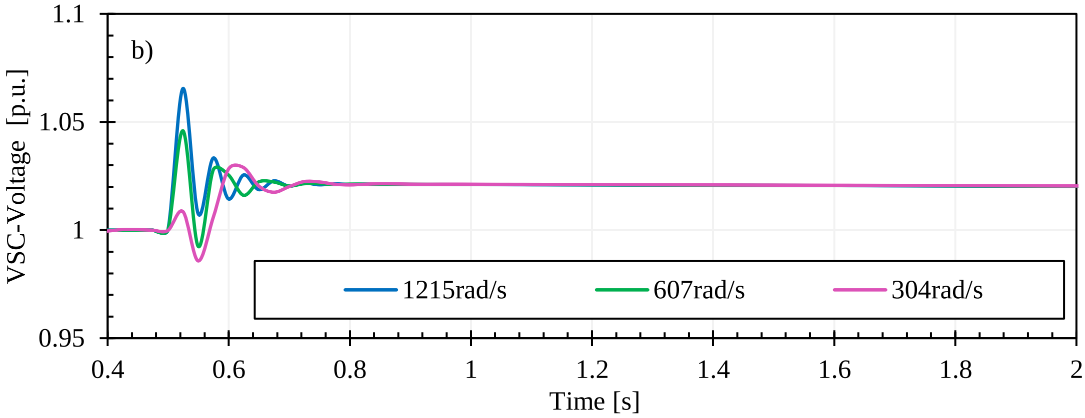

Figure 6.5: CVC active power (a) and voltage (b) response during a power/voltage reference step for different values of $\propto_{cc}$.

Assuming $\propto_{cc}$ equal to 1215 rad/s, Figure 6.6 shows the results of other simulations performed considering the following reference active power steps: 1;0.5; 0.2 in p.u.

The trend of Figure 6.6 is always the same for different values reference power. The reason is that the closed-loop function G_c given in Equation.6.1 depends only on the chosen value for $\propto_{cc}$.

Table 6.2 shows the analysis of overshoot S_e% and settling time $T_{\alpha\varepsilon}$.

Table 6.2 Different response characteristics from CCC.

Reference	VSC Active Power		
	20%	50%	100%
S_e%	59.7	56.4	50.
$T_{\alpha\varepsilon}$	0.6	0.6	0.6

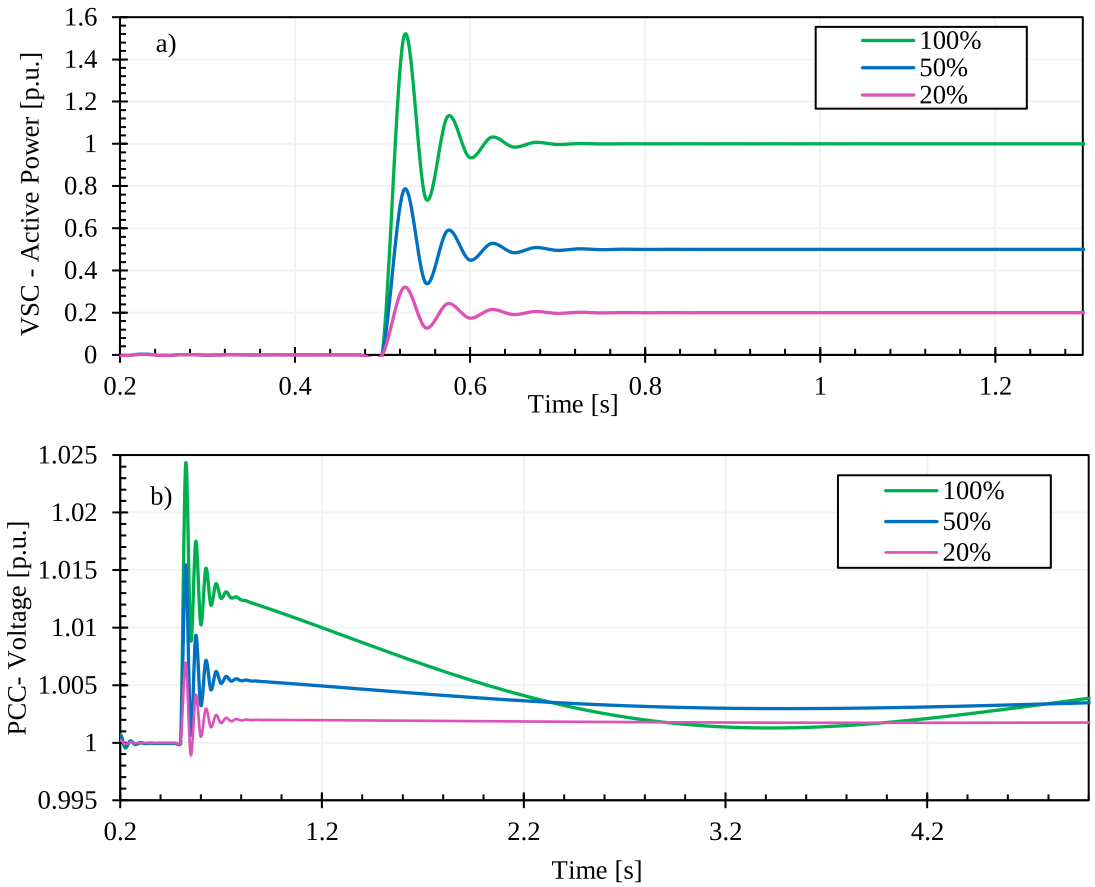

Figure 6.6. CC response for a reference power step and a reference voltage step, a) Active power for different RES penetration and b) PCC voltage for different RES penetration.

Two block diagrams represent the RC [105], [106], that provides the dq input to the CC. The first one is an active power close loop for the d-axis current reference I_d^*. The second is a reactive power close loop for the q-axis current reference I_q^*. In this context, Figure 6.6 shows the vector diagram and the control block of the dq-current I_{dq}, where I is in phase with the voltage V_{pcc}, and I_{q} can be used to control the PCC-reactive power $\mathrm{Q_{pcc}}$.

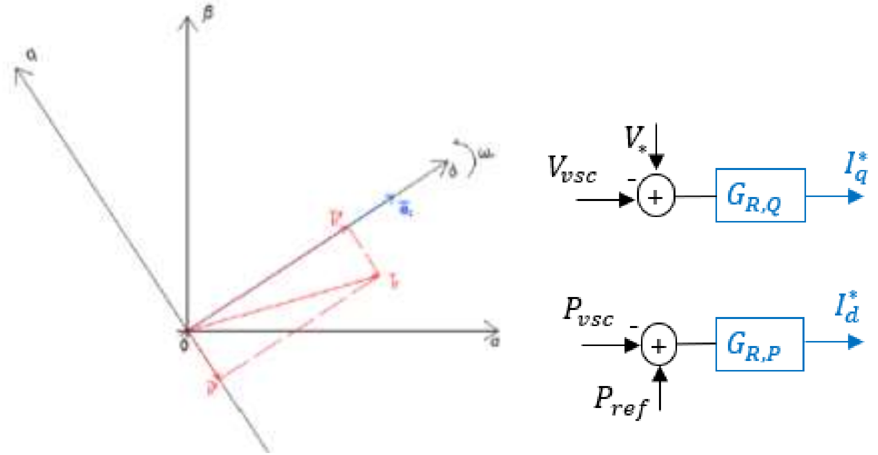

Figure 6.7. Vector Diagram and RC controllers.

The controller has an open-loop structure described by the following equations:

$$I_d^* = (P_{ref} - P_{vsc})G_{R,P} = (P_{ref} - P_{vsc})G_{c,dR}M_{dR}$$
$$I_q^* = (Q_{ref} - Q_{vsc})G_{R,Q} = (Q_{ref} - Q_{vsc})G_{q,cR}M_{qR} \tag{6.2}$$

where:

- $G_{c,dR}$ is the transfer function of the PI controller with proportional gain $k_{p,RP} = \propto_{RP} L_f$ and integral gain $k_{i,RP} = \propto_{RP} R_f$; where $\alpha_{RP} = 10/\alpha_{cc}$ represents the bandwidth;
- M_{dR} represents a limiter between 0 to 1.2 p.u.;
- $G_{q,cR}$ is the transfer function of the PI controller with proportional gain $k_{p,RQ} = \propto_{RQ} L_f$ and integral gain $k_{i,RQ} = \propto_{RQ} R_f$; where $\propto_{RQ} \approx -0.01 \propto_{cc}$;
- M_{qR} represents a limiter between -1 to 0 p.u.;
- Q_{ref} represents the VSC reference reactive power and is set equal to 0 p.u.

Figure 6.8 shows the output of the RC controller for $\propto_{cc}$= 125 and 62.5 rad/s considering a power step at t = 0.5 s.

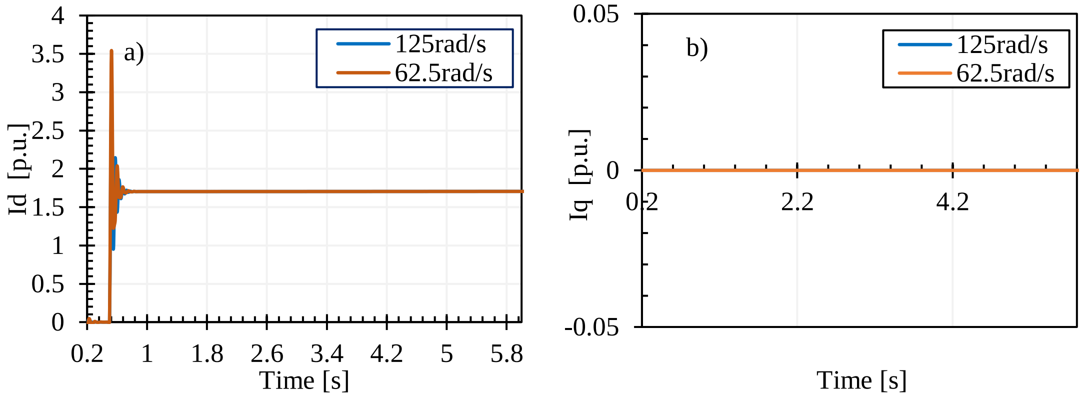

Figure 6.8. The output of the RC during a reference power step for different $\propto_{cc}$. a) d axis and b) q axis.

The last block characterizing the CCC is PLL. In order to synchronize the converter to the grid, it is necessary to implement a PLL. The control algorithm uses the output and input signals feedback circuits [46]. A block diagram of the conventional PLL designed is shown in Figure 6.8. The PLL operation starts by measuring the instantaneous AC output voltage at the PCC $V_{pcc(abc)}$, then this information is converted by an abc/dq transformer in dq-voltage $V_{pcc(dq)}$. The voltage $V_{\mathrm{pcc(q)}}$ is the input of the PLL filter in the proportional-integral form G_{pll}. The filter calculates the grid voltage angular frequency change $\Delta\omega$, which is added to the reference angular frequency. In this way, the grid angular frequency ω_{pll} and the angle θ_{pll} are evaluated [107], [108].

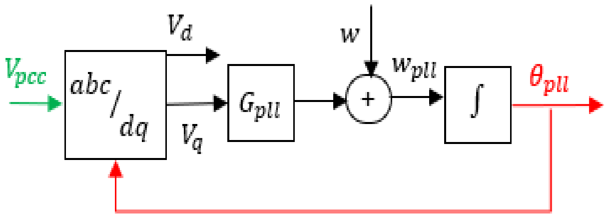

Figure 6.8. PLL block scheme.

G_{pll} represents the transfer function of a PI control with a proportional gain $k_{p,pll} = 2\alpha_{pll}$ and an integral gain $k_{i,pll} = \alpha_{pll}^2$, where α_{pll} represents the PLL bandwidth. To maintain the synchronism condition $\Delta\theta = 0$, the PLL must reset $\Delta\theta$ by varying the speed ω_r. Therefore, with $\hat{x}$ = [$\hat{\omega}_r$, $\hat{\theta}$]T, the linearised estimator can be expressed in state-space form as $d\bar{x}/dt = A\bar{x} + B\theta$ with the polynomial characteristic of this PLL is given by:

$$det(sI - A) = s^2 + \gamma_2 s + \gamma_1 \tag{6.3}$$

The poles of Equation 6.3 can be selected according to two perspectives

- two poles with an imaginary part, obtaining a second-order response;
- two poles with a real part getting a reasonable reaction.

In [109], they remarked that the PLL tuning must have: speed, precision and adequate action in case of a sudden voltage phase jump. A good compromise between these requirements is to keep bandwidth low to properly reject possible harmonics, to maintain a high dynamic response. For these reasons, a $\alpha_{\mathrm{pll}} = \pi$ rad/s is considered. Figure 6.9 shows the PLL response (grid frequency f_{ref}=50 Hz) for the voltage reference passing with a step from 0 p.u. to 1p.u. at t =0.5 s.

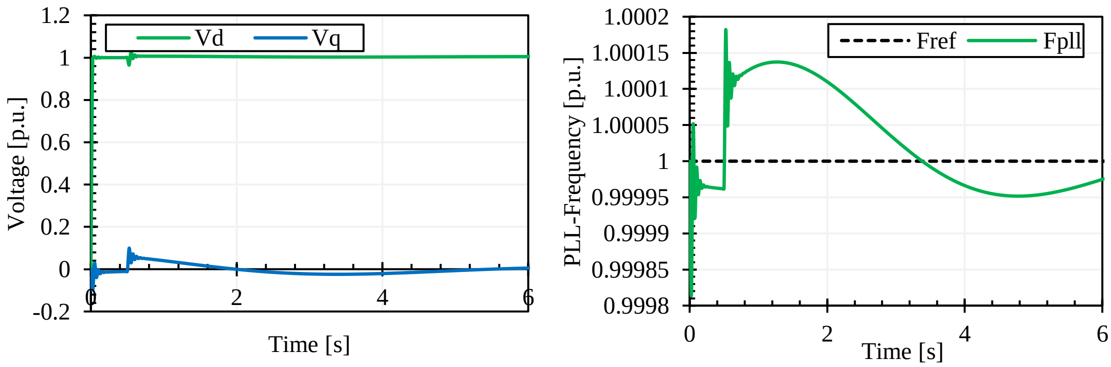

Figure 6.9. Voltage/Frequency response from PLL during a reference voltage step.

6.4. Classical VSM-Structure

The VSM control has the potentiality to allow a compatible grid integration of a VSC even in a weak isolated grid since it mimics the response of an SG. VSM has been proposed recently [110], [111], [112] and [113]. VSM- phase angle θ_{vsm} from Swing Control (SC) is shown in part 1 of Figure 6.10. The θ_{vsm} is used to generate the voltage V_{vsc}. The references for the virtual inertia and active power allow the choice of the oscillation damping and the inertia support that will be used by the converter to overcome the power system needs. The converter can operate in such a way that can provide a primary reserve to the grid.

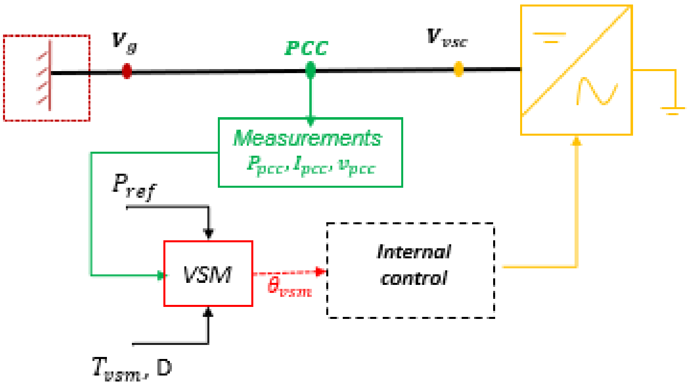

Figure 6.10: Basic VSM scheme.

The control process shows that:

- VSM provides power and emulates inertia and damping;
- VSM can be modelled in RMS-system studies;
- VSM contributes to the reduction of the RoCoF;
- the control succeeds considering delays, even in case of low SCR.

The VSM model proposes a power balance synchronisation mechanism established by the Swing Equation:

$$2H_{vsm}\frac{d\omega_{vsm}}{dt} = P_{ref} - P_{vsc} - Dw_{vsm} \qquad (6.4)$$

$$\frac{d\theta_{vsm}}{dt} = \omega_o\omega_{vsm} - \omega_o$$

where

- H_{vsm} is the virtual inertia of the VSC [s];
- ω_o is the rated angular frequency of the system [rad/s];
- ω_{vsm} is the angular frequency at the VSC [p.u.];
- P_{ref} is the reference active power of the VSC [p.u.];
- P_{vsc} is the actual active power output of the VSC [p.u.];
- D is the virtual damping coefficient of the VSC;
- θ_{vsm} is the angle position of the converter voltage concerning a reference frame synchronised with the grid and rotating at a constant frequency of in steady-state;

Equation 6.5 expresses θ_{vsm} in the Laplace domain:

$$\theta_{vsm} = \frac{1}{s}\left[\omega_0 + G_{vsm}(P_{ref} - P_{vsc})\right] \qquad (6.5)$$

where, G_{vsm} represents the transfer function $1/s[2H_{vsm}(\omega_o)^{-1}]$.

Taking into account the VSM model, Figure 6.10 shows the results of some simulations performed for different VSC active power reference steps (0.2 p.u.=20%; and 1 p.u.=100%.) with inertia constants 0.1 (red line), 3 (blue line), 7 (pink line), 10 s (green line) and damping levels: 30, 50, 100.

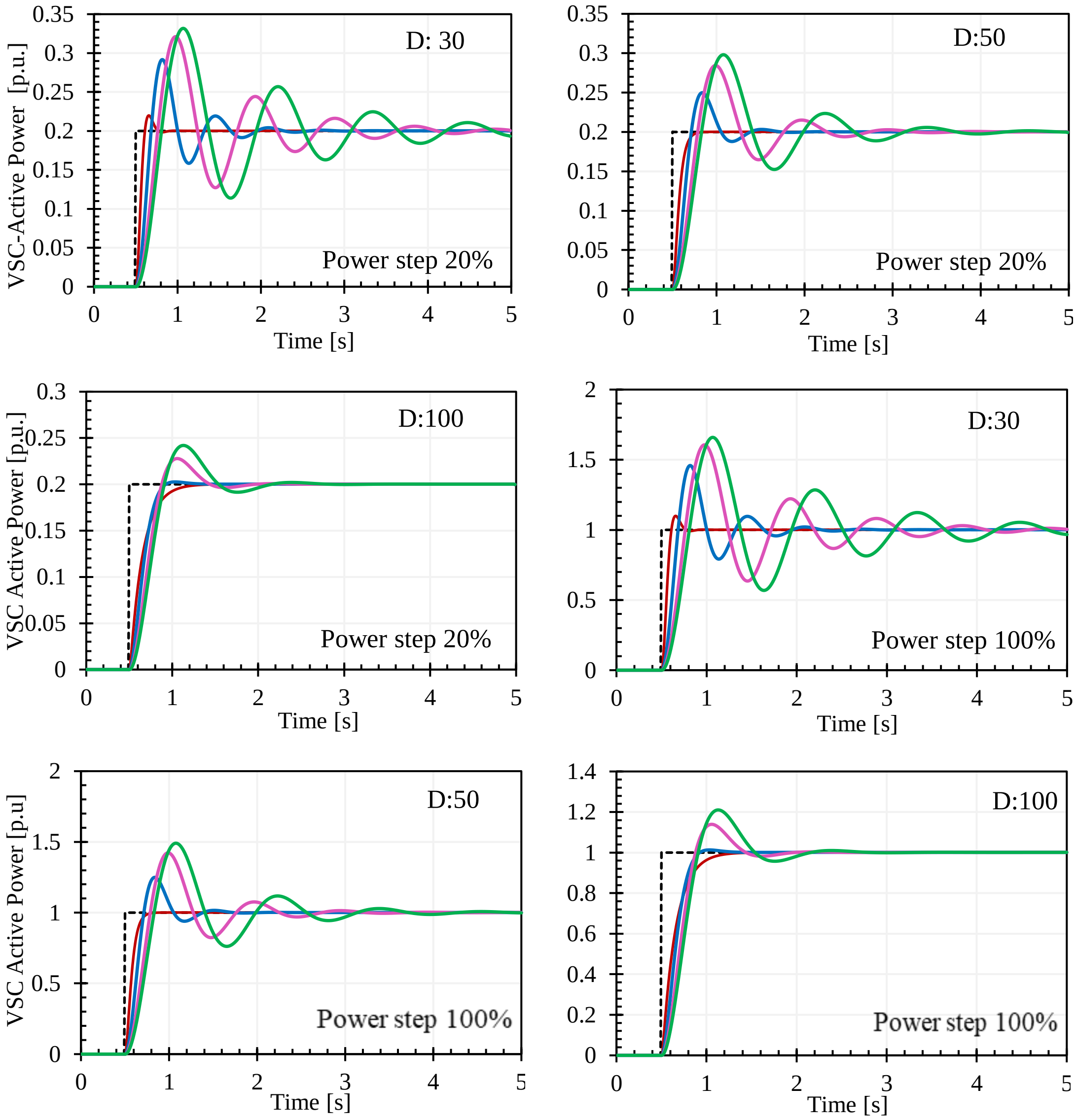

Figure 6.10. VSM response for different values of H_{vsm} and D with power step equal to 20% and 100%.

Figure 6.10 shows that waveform improves with high damping values. Note that the damping is opposed to the IR. Below, in Table 6.3 the analysis of overshoot S_e% and settling time $T_{\alpha\varepsilon}$ is shown. Table 6.3 allows verifying the similarity of the dynamic response of VSM with D between 50 to 100; with D in this range, it is possible to obtain a low power fluctuation.

Table 6.3. Different response characteristics from VSM.

Reference	D	Active Power Step		
		20%	50%	100%
S_e%	30	60.50%	60.50%	60.50%
	50	42%	42%	42%
	100	13.90%	13.90%	13.90%
$T_{\alpha\varepsilon}$[s]	30	2,9	1,9	1,1
	50	2,9	1,9	1,1
	100	2,9	1,9	1,1

Control methods that provide damping of VSM have been proposed recently in [114].
The steady-state active power injected by the VSC is given by:

$$P_{vsm} = \frac{V_{vsc}V_g}{X_f} sin\theta_{vsm} \tag{6.6}$$

Taking into account equations (6.4) and (6.6), the small-signal (Δ) analysis of the system leads to the following expression:

$$\begin{gathered} 2H_{vsm} \cdot \frac{d\Delta\omega_{vsm}}{dt} = \Delta P_{ref} - \frac{\mathrm{d}P_{vsm}}{\mathrm{d}\theta_{vsm}} \cdot \Delta\theta_{vsm} - D \cdot \Delta\omega_{vsm} \\ \frac{d\Delta\theta_{vsm}}{dt} = \omega_o \cdot \Delta\omega_{vsm} \\ \frac{\mathrm{d}P_{vsm}}{\mathrm{d}\theta_{vsm}} = \frac{V_{vsc} \cdot V_{PCC}}{X_f} \cdot cos\theta_{vsm0} = K_{p,vsm} \end{gathered} \tag{6.7}$$

where θ_{vsm0} [rad] is the steady-state virtual angle and $K_{p,vsm}$ represents the synchronising torque coefficient.
To find the relation between the variation of the output power ΔP_{vsm} and the reference power ΔP_{ref}, it is necessary to study the controller response based on Equation 6.7. The system's linear model can be written as follows:

$$\frac{d}{dt}\begin{bmatrix} \Delta\omega_{vsm} \\ \Delta\theta_{vsm} \end{bmatrix} = \begin{bmatrix} -K_{d,vsm}/2H_{vsm} & -K_{p,vsm}/2H_{vsm} \\ \omega_o & 0 \end{bmatrix} \begin{bmatrix} \Delta\omega_{vsm} \\ \Delta\theta_{vsm} \end{bmatrix} + \begin{bmatrix} 1/2H_{vsm} \\ 0 \end{bmatrix} \cdot \Delta P_{ref} \tag{6.8}$$

transforming Equations 6.7 and 6.8 in the Laplace domain

$$\omega_{vsm} = \frac{1}{s2H_{vsm}}\left(\Delta P_{ref} - \frac{\Delta P_{vsc}}{d\delta_v} \Delta\delta_v - K_{p,vsm}\Delta\omega_{vsm} \right) \tag{6.9}$$

$$\Delta\theta_{vsm} = \omega_{\mathrm{o}} - \frac{\Delta\omega_{vsm}}{s} \tag{6.10}$$

$$\Delta P_{vsc} = K_{p,vsm}\Delta\theta_{vsm} \tag{6.11}$$

$\Delta\omega_{vsm}$ from Equations 6.10 and 6.11 is

$$\Delta\omega_{vsm} = \frac{sP_{vsc}}{K_{p,vsm}\omega_0} \tag{6.12}$$

From Equations 6.6 and 6.12, after some mathematical passages, the following expressions are obtained

$$\Delta\omega_{vsm}\left(1 + \frac{K_{p,vsm}\omega_0^2}{2s^2H_{vsm}} + \frac{D}{2sH_{vsm}}\right) = \frac{1}{2sH_{vsm}}\Delta P_{ref} \tag{6.13}$$

$$\frac{sP_{vsc}}{K_{p,vsm}\omega_0}\left(1 + \frac{K_{p,vsm}\omega_0^2}{2s^2H_{vsm}} + \frac{D}{2sH_{vsm}}\right) = \frac{1}{2sH_{vsm}}\Delta P_{ref}$$

replacing Equation 6.13 in Equation 6.12, it is obtained:

$$VD_{vsm} = \frac{\Delta P_{vsm}}{\Delta P_{ref}} = \frac{\frac{\omega_0 K_{p,vsm}}{2H_{vsm}}}{s^2 + \frac{D}{2H_{vsm}}S + \frac{\omega_0 K_{p,vsm}}{2H_{vsm}}} = \frac{\omega_n^2}{s^2 + 2\beth\omega_n s + \omega} \tag{6.14}$$

where VD_{vsm} represents the power imbalance transfer function. The poles from Equation 6.14 are $-\beth\omega_n \pm \omega_n\sqrt{\beth^2 - 1}$, where $\beth$ is the damping ratio and ω_n represents the natural frequency. Equation 6.14 represents a second-order function, where the response can be modified depending on the following characteristics:

- for $0<\beth<1$ the poles are complex and conjugated, and therefore the response is oscillatory damped; the oscillation frequency, in this case, is given by the imaginary part of the poles and an overshoot characterises the system for a step in the reference active power;
- for $\beth\geq1$ the poles are real and negatives and therefore the response is non-oscillatory damped. In this case, the overall dynamic response of the system is decided by the smaller poles, and this maximises the dynamic response of the control of the active power;
- for $\beth=1$ the system has two coincident poles in ω_n. In this case, the transfer function in Equation 6.14 becomes:
-

$$VD_{vsm} = \frac{\omega_n^2}{(s + \omega_n\ )^2} \tag{6.15}$$

The setting of the values of $\beth$ and ω_n must be done correctly, as shown in Figure 6.11, where the results of some simulations are reported. Simulations are performed based for an active power step of 0.7 p.u. at t=0.5 s and different values of $\beth$ (0.1, 0.5, 0.7071) and ω_n (125.6, 62.8, 31.4, 9.42 rad/s).

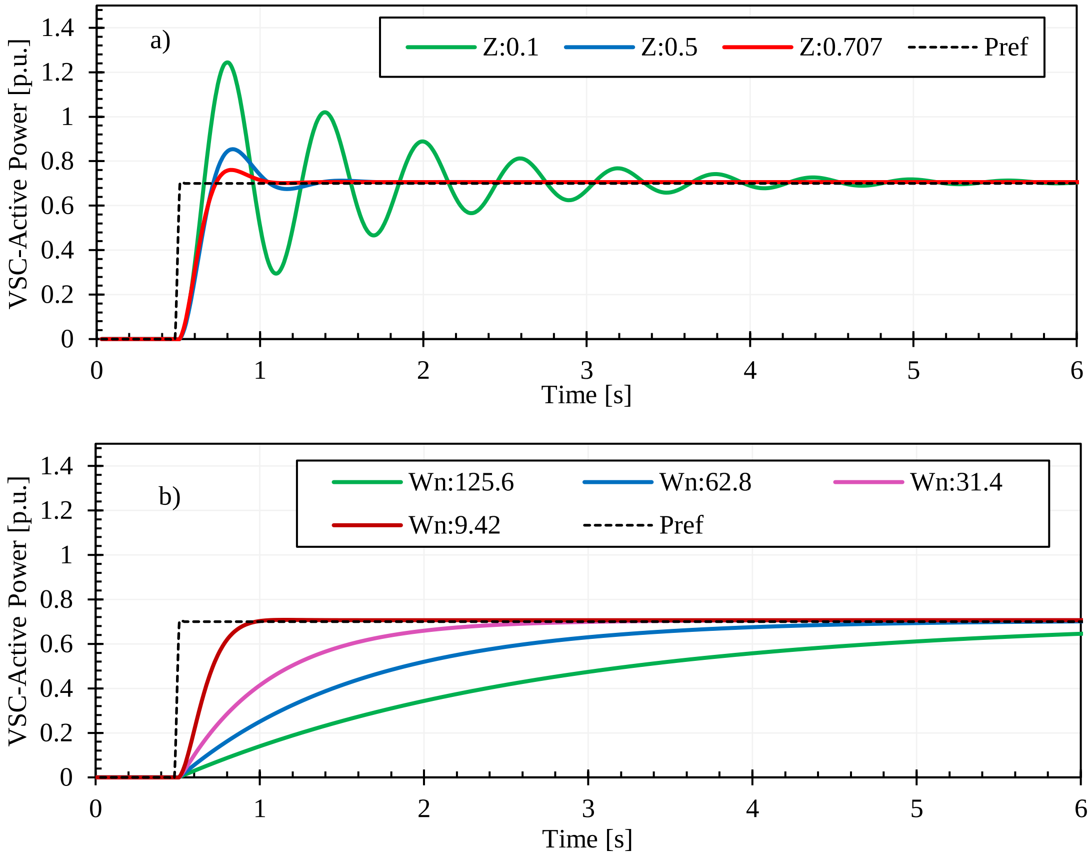

Figure 6.11. The response of the VSM to a 0.7 p.u. power step varying the damping ration (a) and the natural frequency (b).

D can be calculated as a function of the other parameters. For doing this, it is necessary to find V_{vsc} and δ_{v0} at the steady-state after a step variation of the active power reference. From Equation 6.14 is therefore obtained the value $D = 4H_{vsm}\beth\omega_n$ where $\omega_n = \sqrt{\omega_o K_{p,vsm}(2H_{vsm})^{-1}}$.

For instance, step active power of 0.7 p.u. is considered at the instant t = 0.5 s. In this case, $V_{vsc} = 1.016\, p.u.$ and $\delta_{v0} = 0.0136\, rad$ and, from the third of Equation 6.7, it is obtained $K_{p,vsm} = 1/X_f$.

To verify the damping control performance, the results of a simulation in the presence of a double-phase short circuit are presented below. The short-circuit is applied at the instant t = 5s with short-circuit resistance $R_{sc} = 0.5\ \Omega$ and H_{vsm} is assumed equal to 7 s. Figure 6.12 responds to the active power step applied at t=0.5 s (Figure 6.12 a), and the response to the short-circuit (Figure 6.12 b) with the assumed values for *D* and H_{vsm} are shown.

Figure 6.12 shows that the response to the active power step is fast and without oscillation while, in the presence of short-circuit, the derogated current increases by 30 times because VSM control is not capable of guarantee overcurrent protection to the VSC.

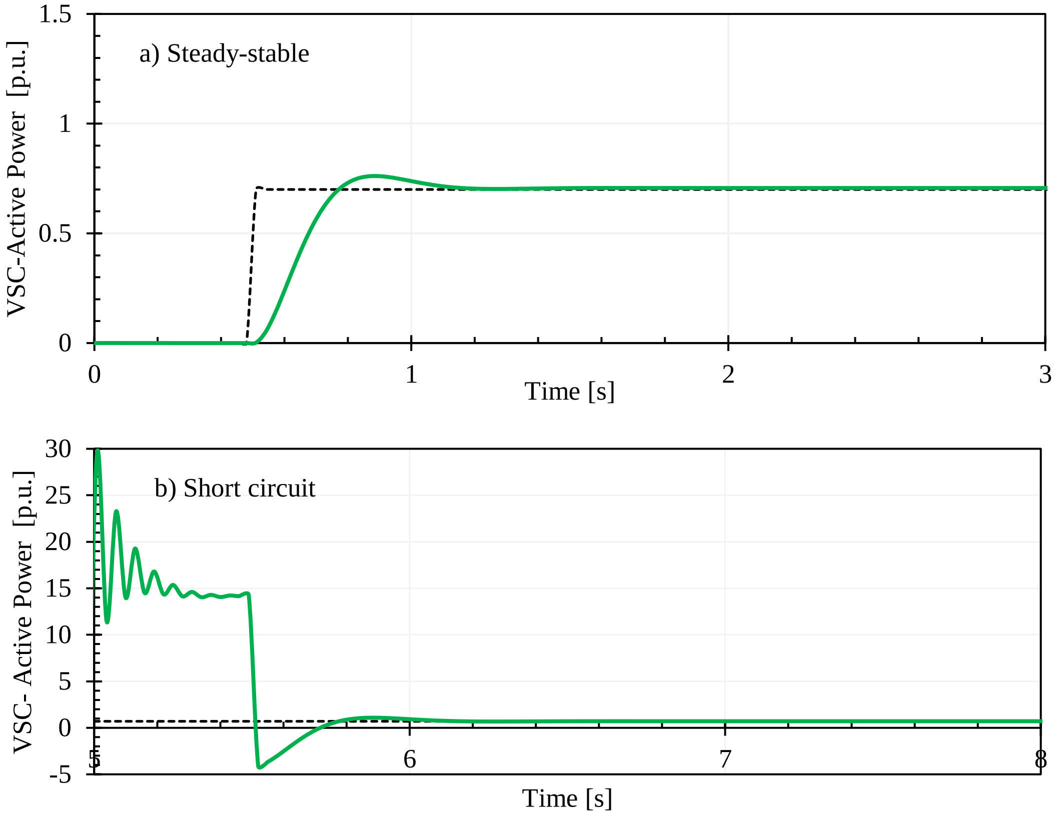

Figure 6.12. Simulation of VSM with Damping Control Loop.

6.5. VSM with CCC

As shown in Figure 6.12, the VSM control guarantees to the VSC a behaviour like an SG but does not guarantee the protection of the converter from overcurrent in the presence of a short circuit in the grid. A solution to this problem is to limit the converter current using the CCC described in Section 6.3. Therefore, this Section proposes a fusion between VSM and CCC. Figure 6.13 shows the new block diagram with the combined controls. Seven blocks are visible:

- a VSM block implementing the SG equations;
- a block for taking the measurements of P_{pcc} , I_{pcc} and V_{pcc}, which are the input of the RC block and the abc/dq block;
- the abc/dq and dq/abc blocks, using θ_{vsm} for the transformations of voltages and currents;
- a damping controller denominated as DC used to improve the response in the active power of the VSC;
- a CC used to protect the converter from overcurrent;
- a RC used to obtain the converter input of the current control and coordinate the abc/dq and dq/abc transformation;

P_{ref}, H_{vsm} are reference variables while L_f and ω_0 are complementary variables [115], [116].

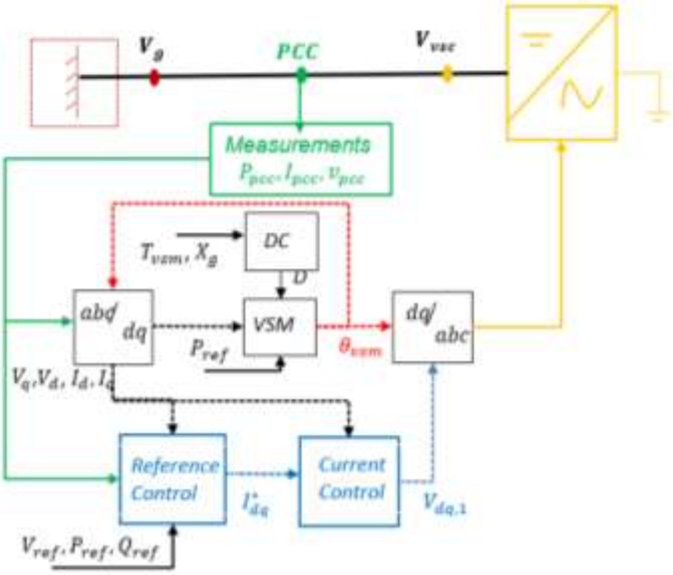

Figure 6.13. VSM-CCC fusion.

6.5.1. Comparison between CCC and VSM+CCC in the presence of time delay

All the simulations presented in the previous sections in order to compare the various control strategies were conducted in the ideal case in which there is no time delay in the control. In that case, the dynamics of the converter and the grid were compatible: it means that even if the dynamics of the grid are fast, since the converter is fast enough, it can follow the oscillations of the parameters effectively. But if a delay Δt is introduced in the measurement or the control system, the current that is delivered at the instant t + Δt based on the current measured at time t is different from the current that would be provided in the ideal case at time t. This difference depends on the dynamics of the grid. If the grid is robust, then even supplying a significant component of reactive current, the voltage oscillations are contained just because the grid is strong. It means that, in all cases, the delay does not have much influence on the control. In case of a weak grid, instead, as soon as the VSC sets the reference current necessary to supply the right reactive power to reach the new voltage value, the voltage itself will vary significantly: the grid dynamics will be therefore very fast and, considering the delay (as in the real case), the controller may not be able to be effective [117].

In this section, the CCC and the VSM+CCC control are compared, considering a delay in the control structure. The system to which refer is the one presented in Figure 6.1. The E-S.1 converter is based on VSM+CCC and can provide virtual inertia and damping. The E-S.2 converter is based on CCC with current feedback control through coordinate transformation.

To test the performances of the two converters in extreme fault conditions, a double-phase short-circuit with a short-circuit resistance $R_{sh} = 10\ \Omega$ is applied to the grid at the instant t = 10 s. A robust grid with SCR=10 and a weaker grid with SCR=5 are considered. A time delay $T_d = 1.5T_s$ with T_s indicating the sampling time (sampling rate f_s of about 1-5 kHz) is introduced. The VSM has the following parameters $H_{vsm} = 7s$, ב= 0.707.

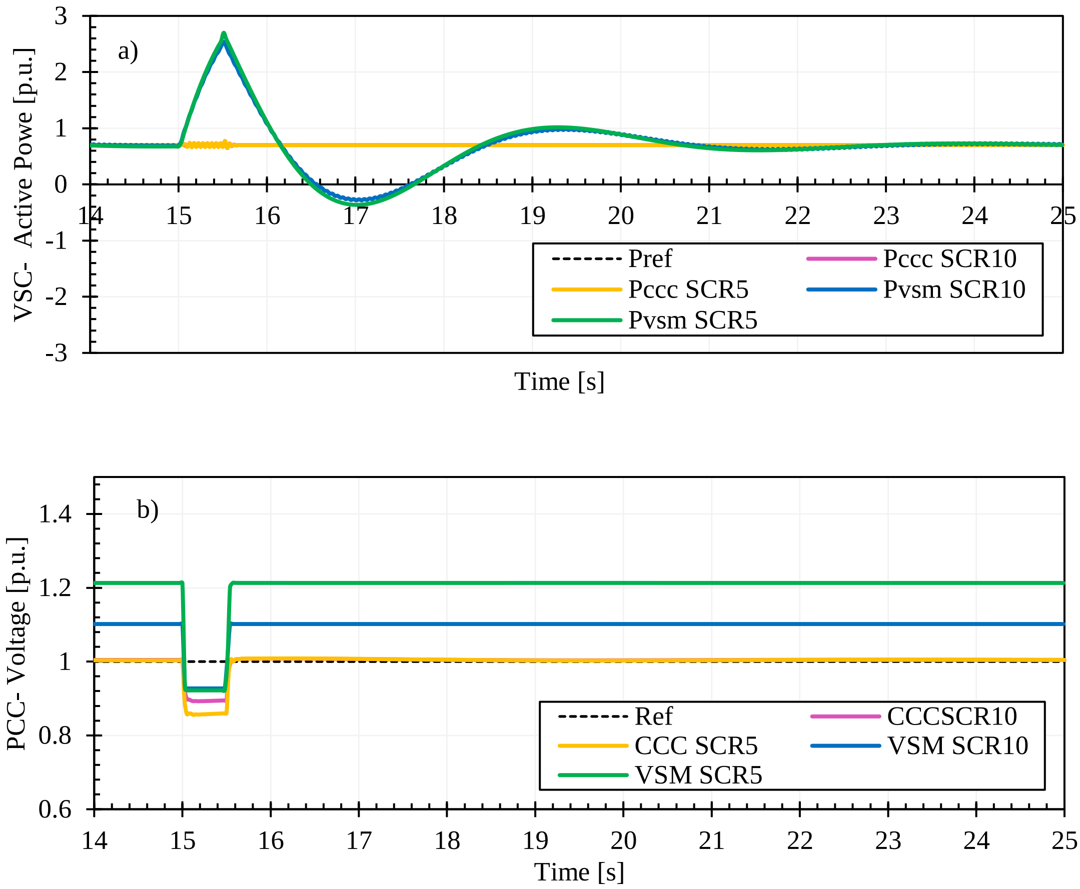

Figure 6.14. Controllers response during a load step.

The trends in Figure 6.14 show sthat:

- the E-S.1 converter with VSM control has a variable active power trend that depends on the SCR;
- the E-S.2 converter with CCC has the same VSC's active power trend for the two different SCR values;
- E-S.1 response speed is slower than E-S.2;
- E-S.1 has an active power overshoot of 4 p.u. while E-S.2 has an overshoot of 0.2 p.u.;
- in the case of SCR, E-S.1 is not capable of supporting a weak grid. PCC-voltage is 12% over the allowed range in the case of SCR = 5.

6.5.2. Presence of a load at the PCC

In the case of a load connected to the PCC (Figure 6.15), the internal control (present both in the CCC and in the VSM+CCC) can be modified through a reduction of the grid using a Thevenin equivalent impedance $Z_{th} = R_{th} + j\omega_O L_{th}$ [118].

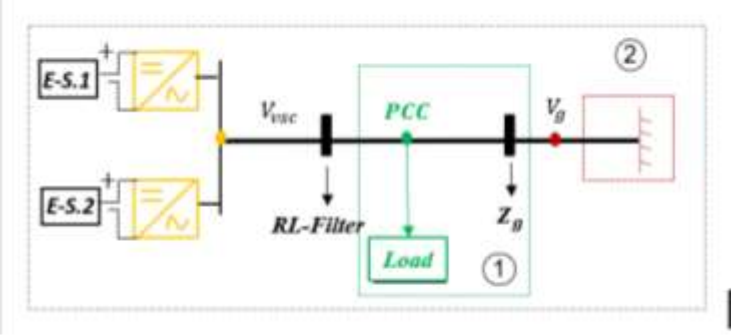

Figure 6.15. The grid model with a load connected at PCC.

In this case, Equation 6.1 is rewritten as it follows:

$$V_{vsc}^{dq*} = V_{pcc}^{dq} + \pm\omega_O L_{th} \cdot\ I_{dq} + G_{c,th} \cdot \left(I_{dq}^{*} - I_{dq}\right) \tag{6.16}$$

where $G_{c,th}$ represents the transfer function of a proportional-integral PI block with

- proportional gain $K_{p,th} = \propto_{cc,th}\ L_{th}$
- integral gain $K_{I,th} = \propto_{cc,th}\ R_{TH}$
- bandwith $\propto_{cc,th}$

and the equivalent Thevenin impedance is:

$$Z_{th} = \frac{(R_{load} + j\omega_O L_{load})\left(R_g + j\omega_O L_g\right)}{(R_{load} + j\omega_O L_{load}) + \left(R_g + j\omega_O L_g\right)} \tag{6.16}$$

[119], [120], [121] some techniques show a better performance of the VSC in terms of power quality with the impact of the load using an impedance estimation into CCC. The methods by grid impedance estimation are generally passive [119], [121] and active [122]. For this case, a simple passive method like [121], [123], is proposed. In this way, an estimator for inductance ($\boldsymbol{L_t}$) and estimator resistance ($\boldsymbol{R_t}$) derived from the power system model is proposed to use into cross-coupling ($\boldsymbol{W_{Rv}}$) and the calculation of the PI parameters as shows Figure 6.17. Also, an active resistance ($\boldsymbol{R_v}$) is added to reduce the current error by increasing the integral parameter of the PI, generating the possibility of active damping within CCC.

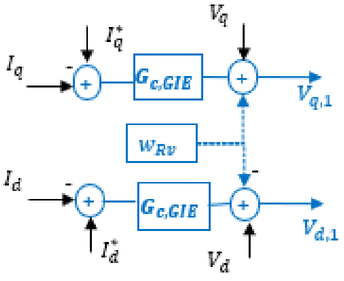

Figure 6.16. Internal current control with impedance estimator.

where

$G_{C,GIE}$ represents the transfer function of a proportional-integral PI block with a proportional gain $k_{p,GIE} = \propto_{GIE}\ L_t$ and integral gain $k_{I,GIE} = \propto_{GIE}\ (R_t + R_v)$.

$\propto_{GIE}$ represents the GIE bandwidth.

L_t is the sum of L_f and L_{th} and R_t is the sum of R_f and R_{th}.
R_v can be calculated since an integral part as $R_v = \propto_{GIE} L_t - R_t$.

In the following, the input reference current $\mathrm{I}_\mathrm{f}^{\mathrm{dq}*}$ can be expressed as:

$$I_f^{dq*} = \left[\frac{V_g^{dq*} - V_g^{dq} + (\boldsymbol{G_{RC,GIE}} - W_{Rv}) \cdot I_f^{dq}}{\boldsymbol{G_{RC,GIE}}} \right] CL \tag{6.18}$$

Where $\boldsymbol{CL}$ represents the transfer functions of a current limiter necessary for limiting overcurrents during transients and $\boldsymbol{G_{RC,GIE}}$ represents the transfer function of a proportional-integral PI block with a proportional gain $\boldsymbol{k_{p,GIE}} = \propto_{\boldsymbol{GIE}} \boldsymbol{L_t}$ and integral gain $\boldsymbol{k_{I,GIE}} = \propto_{\boldsymbol{GIE}} (\boldsymbol{R_t} + \boldsymbol{R_v})$. $\propto_{\boldsymbol{RC2}}$ represents the RC2 bandwidth.
The setting parameters are; a step active power of 0.7 p.u. activated at the instant t = 5 s, T_{vsm}:7 s, $\propto_{C,GIE}: 1215\ rad/s$ and $\propto_{RC2}: 121\ rad/s$ and perturbation with R_{sh}: 0 Ω and 10 Ω between R_{th} and L_{th}.

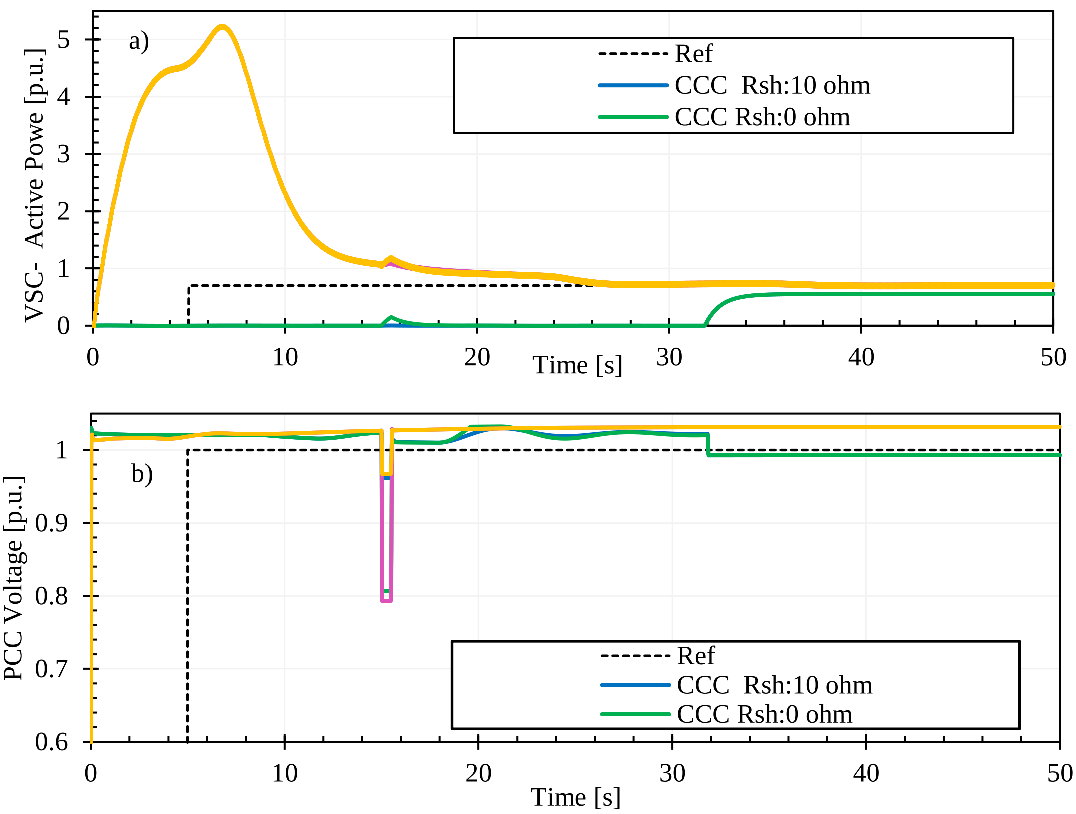

Figure 6.17. Controllers response with impedance estimation and active resistance during a load step.

The trends in Figure 6.19 reveals the following aspects:

- the settlement time Taε from PCC-voltage trend was evaluated as the time taken by the response to definitively enter in a band between ±3% of the steady-state value after the step voltage; in this case, it is set ε% = 0.3 of the steady-state value that corresponds to 0.3 kV. These values are not placed in tables because after the fault the voltage is within this range;

- the simulation results show that the virtual impedance has a visible improvement into system stability and current sharing ability are strongly enhanced;

- the controls require almost 15 s to stabilise in the event of extreme failure resistance;
- E-S.2, allows the VSC to produce only 78% of the reference at 26 s this means that it is slower than E-S.1.

6.6. Conclusion

The chapter presented an overview of two internal control strategies for a VSC in a simple isolated power system in stable-state. The simulations were made by varying reference power in different steps and demonstrating the best option for independently setting parameters of each control. On the other hand, the control system setting parameters are based on the variations of power production that cause voltage fluctuations in the PCC between the converter and the AC grid. A low value of the grid impedance at the PCC reduces the voltage fluctuations, resulting in a robust grid. The dynamic response of the two controls is good at steady-state. In particular, CCC is faster than VSM. Below a comparison is reported of the two internal controls for the VSC in Table 6.4.

Table 6.4. Comparison of VSM/CCC.

Description	CCC	VSM
Possibility of high-frequency instabilities	x	x
Increased RoCof	x	
Emulates inertia		x
Provides synchronising power and voltage reference		x
Not have the capability of regulating voltage	x	
Control succeeds considering delays, even in case of low SCR		x
Can be modelled in RMS system studies		x
Contributes to RoCof		x

Chapter 7

VSM+CCC application for improving system stability in the presence of RES

7.1. Introduction

This Chapter investigates how VSM+CCC control for inverter-interfaced renewable energy sources can be effectively used for improving the dynamic stability in small islands not supplied by the main grid. In the proposed analysis, the RES-based generators of Lampedusa island are assumed interfaced to the grid by VSC with a swing controller and a CCC with two different options for the RC control for regulating the voltage at the PCC and the active power output [52] [48]. Firstly, the hourly electricity production and demand of the island are analysed during typical Winter and Summer days and the power system inertia is calculated hour by hour, looking for the most critical condition in terms of the reduced IR of the generating system in the presence of RES. Subsequently, a simple power system is created, where the overall RES plants are represented as a unique VSC and the conventional SGs as an unique ideal voltage source. The system is modelled in the PScad environment, verifying the response of the renewables-based generators with VSM control in the presence of a disturbance in the grid. In order to examine an extreme situation, a double-phase short-circuit is considered.

7.2. Model of the power system

The simple power system proposed in Figure 7.1 approximates an aggregate model of a two-area power system.

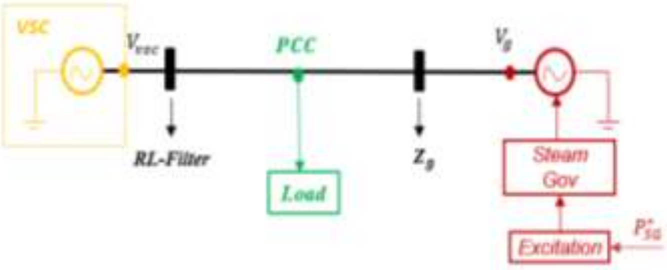

Figure 7.1. Model of the power system.

Figure 7.1 shows:

- on the right an SG with its internal control connected to the grid impedance Zg;
- at the center the load connected to the PCC;
- on the left, the VSC with its RL-filter (Chapter 6).

Concerning the control scheme presented in the previous chapter, a lead-lag filter to measure the active power at the PCC is included, to improve the active power response of the VSC. Also, the implemented control scheme consists of an automatic damping loop and an extension of a power loop (Figure 7.2).

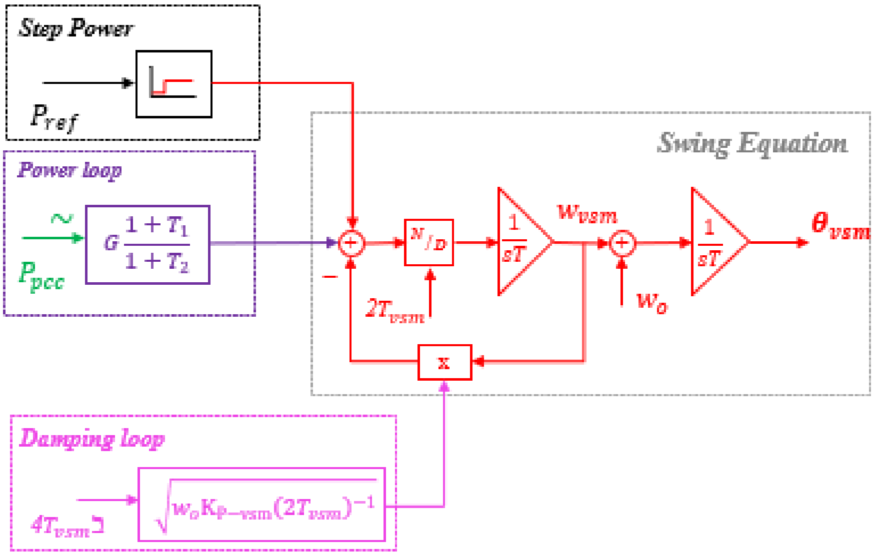

Figure 7.2. VSM structure

The transfer function of the lead-lag has:

- lead time constant $T_2 = 1/\propto_{cc}$
- lag time constant $T_1 = 1/\propto_{RC}$.

Figure 7.3 reports the block diagram of the internal control of the SG. The data assumed for the control circuits are reported in Appendix A Tables A.4.1 to A.4.1V.

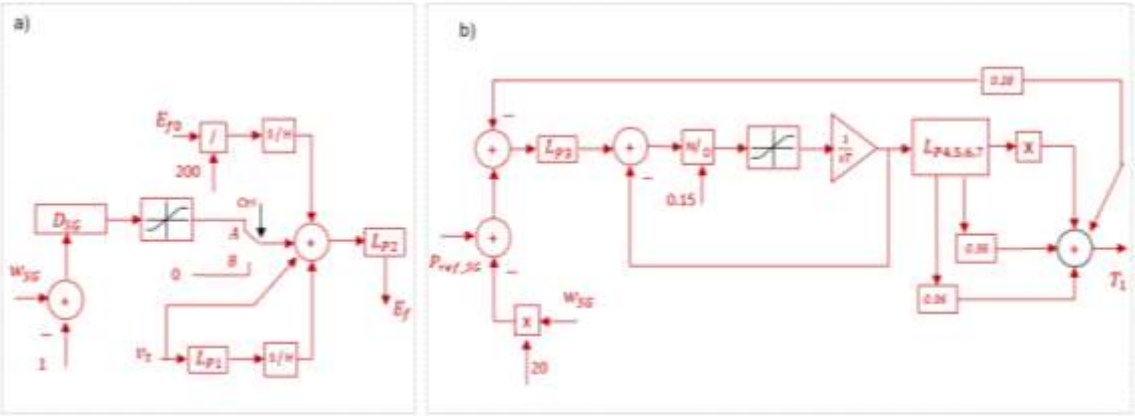

Figure 7.3: SG Internal control: a) power system stabilizer; b) speed governor.

In Figure 7.3 ω_{SG} represents the SG angular frequency, D_{SG} the damping coefficient of the SG, L_{P1} to L_{P7} the transfer functions of low pass filters, E_f the field voltage and P_{ref_SG} the reference active power of the SG.

The swing equation of the SG is:

$$2H_{SG}\,\frac{d\omega_{vsm}}{dt} = P_{ref\_SG} - P_m - D_{SG}\omega_{GS} \tag{7.1}$$

where P_m represents the mechanical power in p.u. and H_{SG} represents the inertia constant in seconds of the SG.

The swing equation of the VSC is described in Chapter 6. In the following, the input reference current $\mathrm{I_f^{dq*}}$ of the VSM is calculated in two different ways:

- Option RC-1: I_f^{dq*} can be expressed as Equation 6.18;
- Option RC-2: I_f^{dq*} can be expressed as:

$$I_f^{dq*} = \left[\frac{V_g^{dq*} - V_g^{dq}}{\omega_o L_g} + I_f^{dq}\right] LP \cdot CL \tag{7.3}$$

where LP is the transfer function of a low-pass filter used for avoiding spiky transients and miscalculations before sending the calculated references to the current controller.

The load at the PCC is modelled as a fixed impedance where active power $\mathrm{P_{load}}$ and reactive power $\mathrm{Q_{load}}$ are expressed as:

$$P_{load} = P_{load-0}\left(\frac{V_{\mathrm{base}}}{V_0}\right)^{NP}(1 + K_{PF}.dF) \tag{7.4}$$
$$Q_{load} = Q_{load-0}\left(\frac{V_{\mathrm{base}}}{V_0}\right)^{NQ}\left(1 + K_{QF}.dF\right)$$

where dF is the frequency variation, V_0 is the rated voltage, P_{load-0} and Q_{load-0} are, respectively, the active and reactive power of the load at the rated voltage and frequency and NP, K_{PF}, NQ and K_{QF} are some indexes expressing the active and reactive power dependence from the actual values of voltage and grid frequency.

7.3. Case study

The case study considers the 10 kV isolated power system of the island of Pantelleria in the case of a high share of RES generation. Considering a renewable energy mix composed by 1 MW of photovoltaic plants and 1 MW of wind plants and taking into account the reports provided by the local utility, the daily power profiles in typical Summer and Winter days for one week are reported in Figure 7.4.

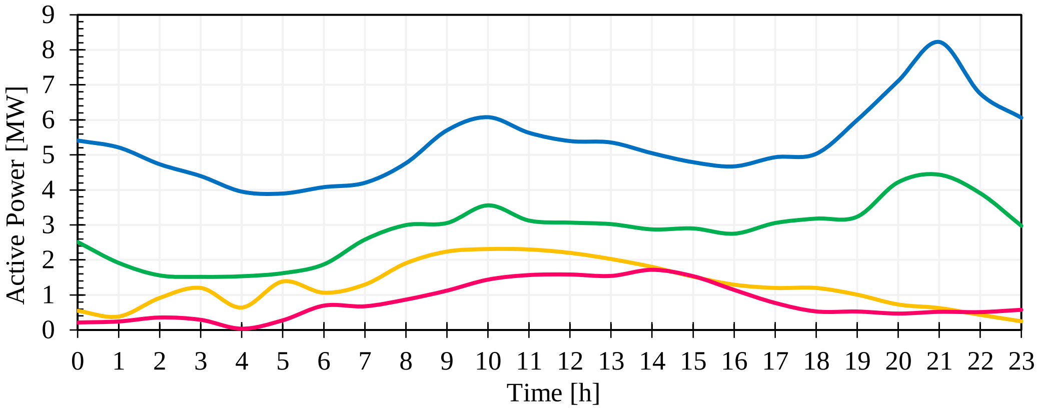

Figure 7.4. Trend electricity production a) from TP and b) from AG.

In particular, the yellow line represents the daily power profile generated by the VSC (mix composed by wind and photovoltaic plants) during Summer while the pink line represents the same power trend in Winter. The blue line represents the daily load power during Summer and the green line the same power in Winter. Based on the previous figure and considering the data of the diesel generators of the island, the inertia of the SG is calculated hour by the hour using Equation 2.2 and shown in Figure 7.5.

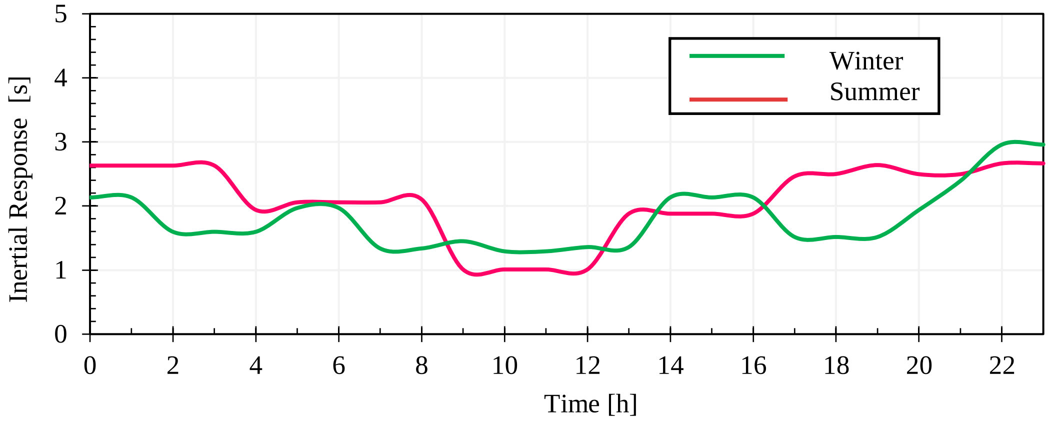

Figure 7.5. Inertia trend in Winter and Summer.

The worst case, defined as the working condition presenting the minimum inertia, is defined both for summer (Scenario A) and winter (Scenario B) in Table 7.1.

Table 7.1. Parameters for the study.

Description	Summer	Winter
H_{SG} (s)	1.01	1.29
H_{sysy} (s)	0.77	0.45
NSPL	24%	65%
P_{load} (MVA)	6.08	3.56
Hour	9	11

The system's behaviour is simulated in the case of a double-phase fault. The methodology for checking the VSM behaviour in case of fault is given in the flow chart reported in Figure 7.6.

In the simulations, the following parameters are considered: ζ=0.707; ω_n=10; $\propto_{cc}< 0.1\cdot 2\cdot \pi\cdot f_s$; f_s =5 kHz. The system is simulated for two different values of the virtual inertia H_{vsm}: 8 s and 0.01 s.

The simulations are divided into four cases: A1, A2, B1 and B2 where A indicates the Winter case while B indicates the Summer case and 1 and 2 show the control option RC-1 and RC-2.

The double-phase short circuit is applied at t=45s. Two different values of the short-circuit resistance R_{sc} are considered: 0.5 Ω and 0.5 kΩ, for testing the VSM control performance in two extreme fault conditions. In addition, the vector-current control is tested with two angle options for the dq-frame transformation:

1) θ_{vsm};

2) $\theta_{comp} = \theta_{vsm} + \theta_0$, where $\theta_0 = 1.5\,\omega_o/\propto_{cc}$.

The second option allows compensating the delay introduced by the PWM using synchronous sampling.

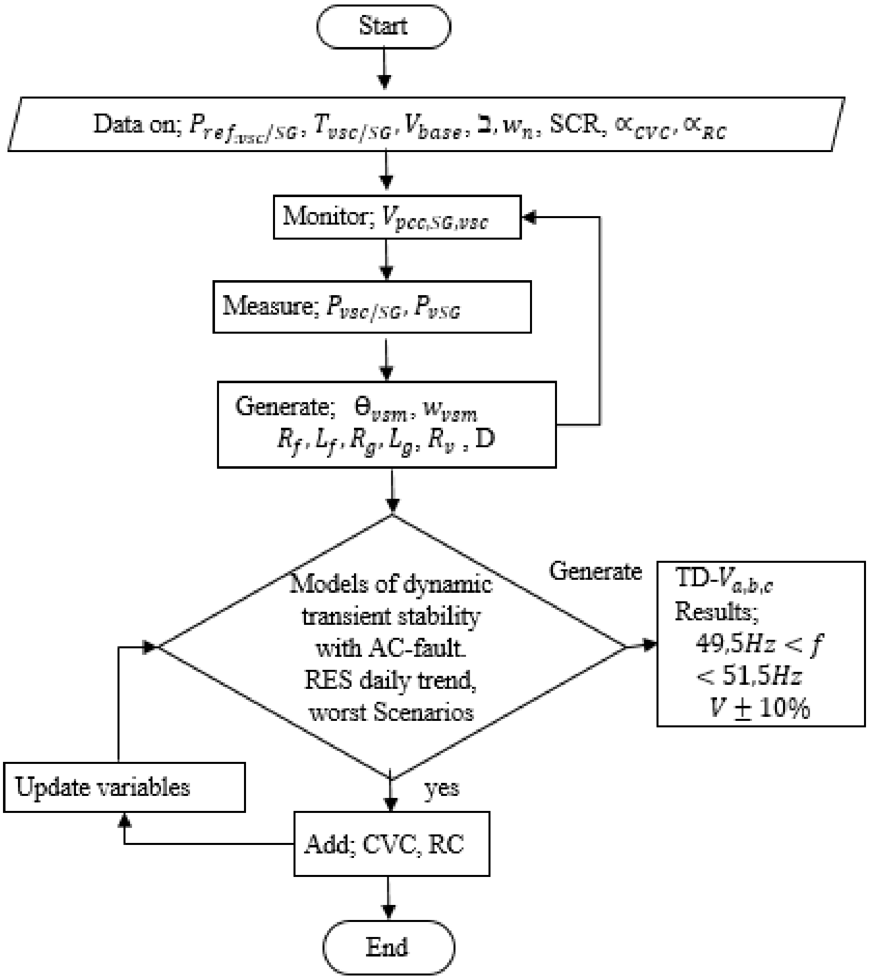

Figure 7.6. Flow chart of the proposed methodology.

Fig. 7.7 shows the power trend calculated, initially, in the hypothesis of the strong grid with SCR=10.

The graphs representing the load and RES active power are grouped into four groups:

- SCENARIO A1: Fig. 7.7 a), b), c), d);
- SCENARIO A2: Fig. 7.7 e), f), g), h);
- SCENARIO B1: Fig. 7.7 i), j), k), l);
- SCENARIO B2: Fig. 7.7 m), n), o), p).

For each scenario, it is assumed:

- β) $\Theta = \Theta_{comp}$; R_{sc}: 0.5 kΩ;
- ∂) $\Theta = \Theta_{vsm}$; $R_{sc} = 0.5$ kΩ;
- Υ) $\Theta = \Theta_{comp}$; $R_{sc} = 0.5\ \Omega$;
- Φ) $\Theta = \Theta_{vsm}$; R_{sc}: 0.5 Ω.

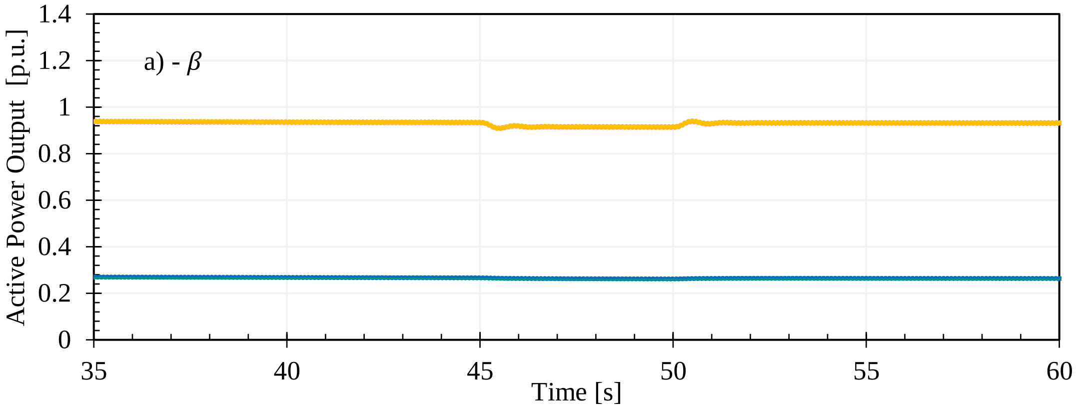

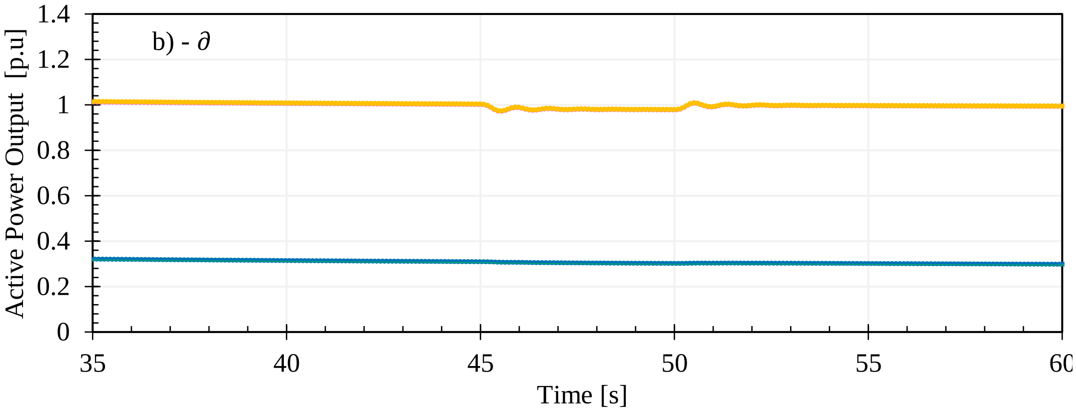

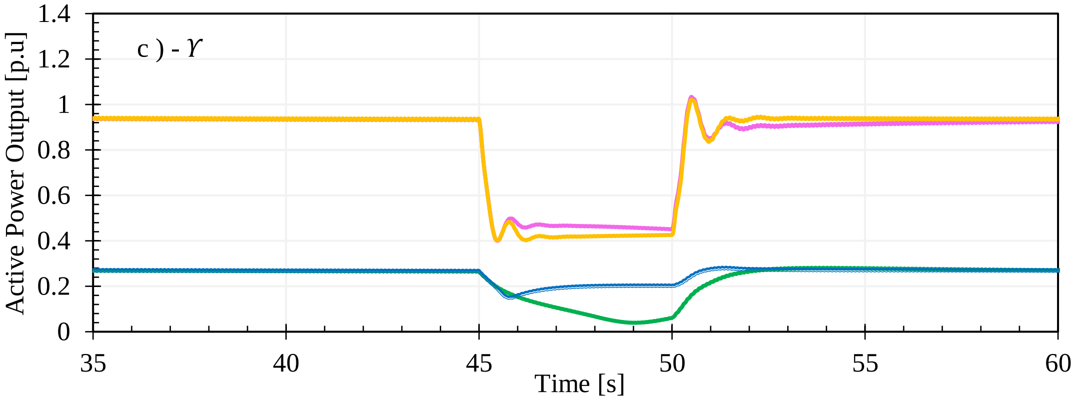

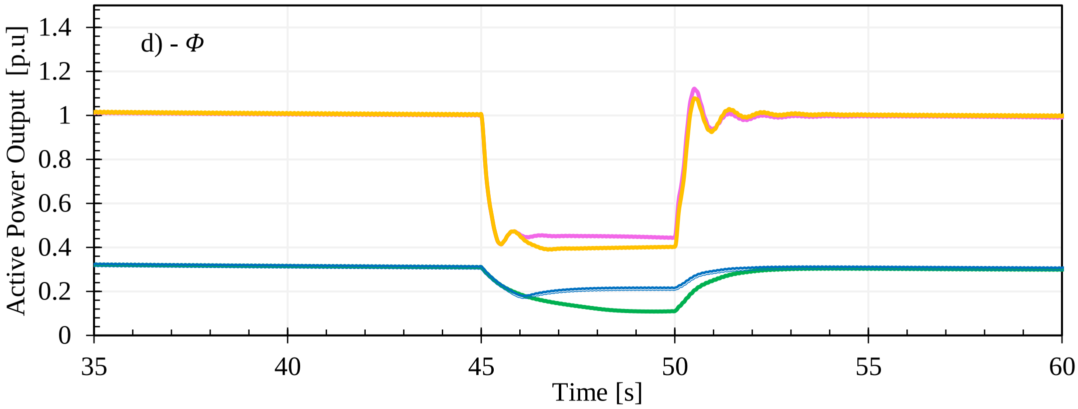
d) - Φ
Active Power Output [p.u]
1.4
1.2
1
0.8
0.6
0.4
0.2
0
35
40
45
50
55
60
Time [s]

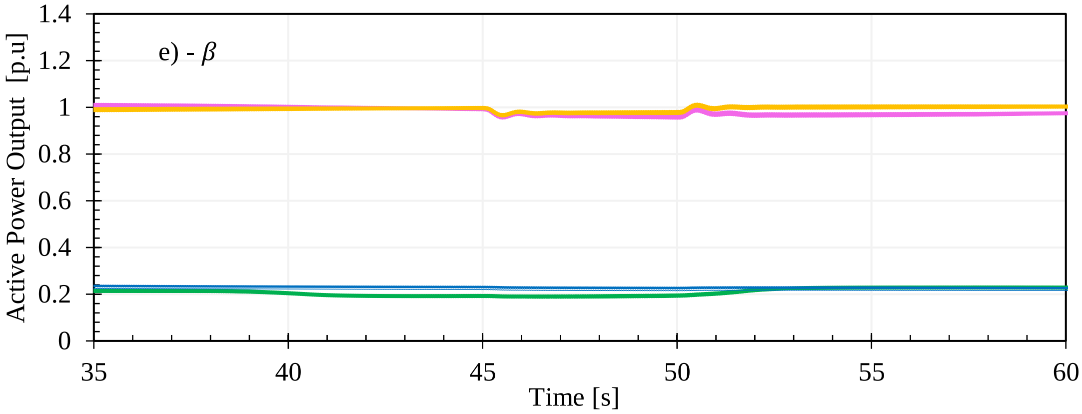
e) - β
Active Power Output [p.u]
1.4
1.2
1
0.8
0.6
0.4
0.2
0
35
40
45
50
55
60
Time [s]

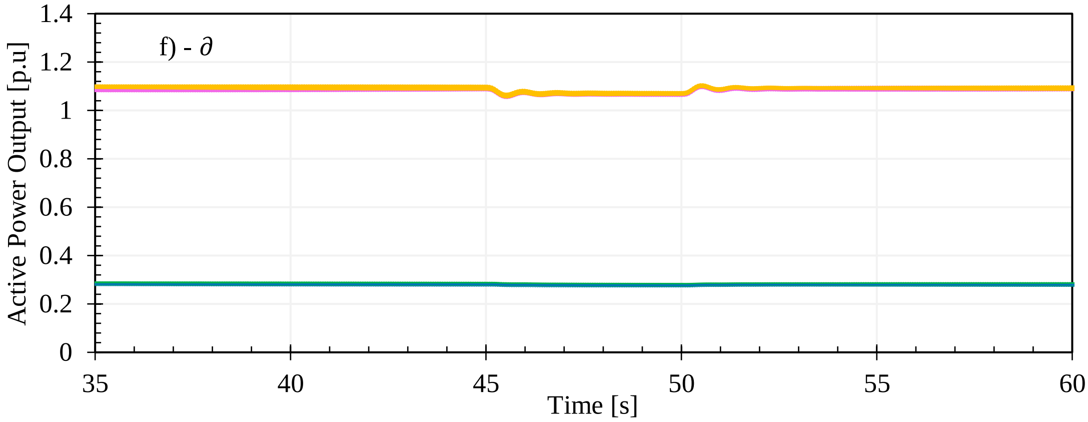
f) - ∂
Active Power Output [p.u]
1.4
1.2
1
0.8
0.6
0.4
0.2
0
35
40
45
50
55
60
Time [s]

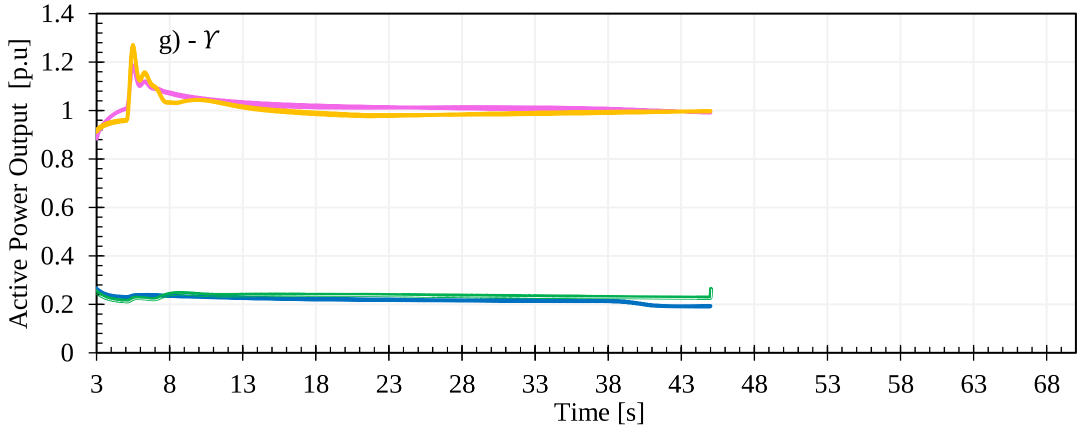
g) - ϒ
Active Power Output [p.u]
1.4
1.2
1
0.8
0.6
0.4
0.2
0
3
8
13
18
23
28
33
38
43
48
53
58
63
68
Time [s]

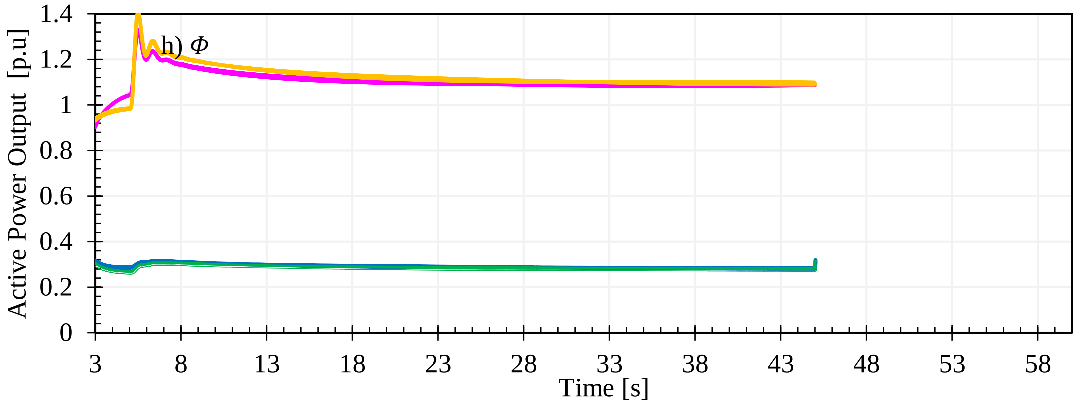
h) Φ
Active Power Output [p.u]
1.4
1.2
1
0.8
0.6
0.4
0.2
0
3
8
13
18
23
28
33
38
43
48
53
58
Time [s]

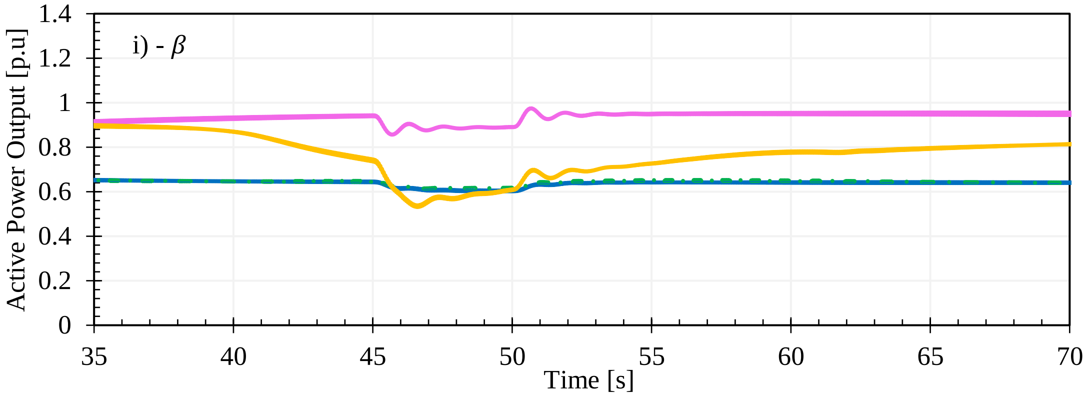
i) - β
Active Power Output [p.u]
1.4
1.2
1
0.8
0.6
0.4
0.2
0
35
40
45
50
55
60
65
70
Time [s]

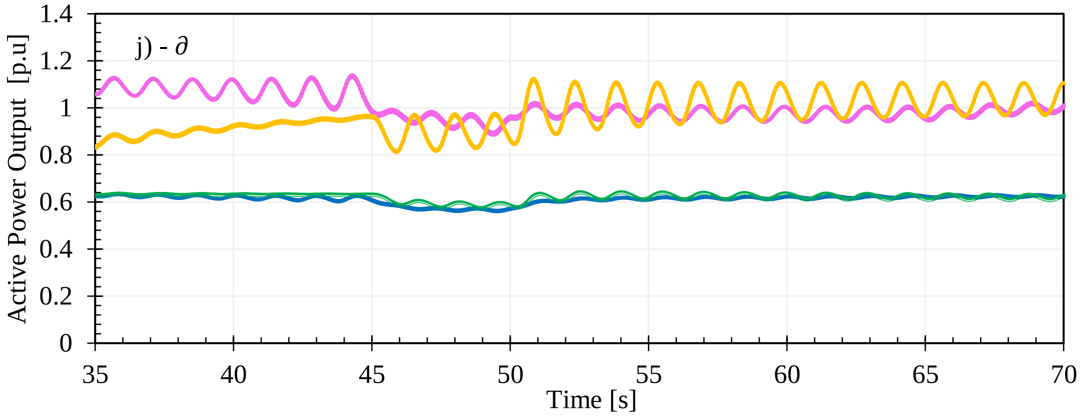
j) - ∂
Active Power Output [p.u]
1.4
1.2
1
0.8
0.6
0.4
0.2
0
35
40
45
50
55
60
65
70
Time [s]

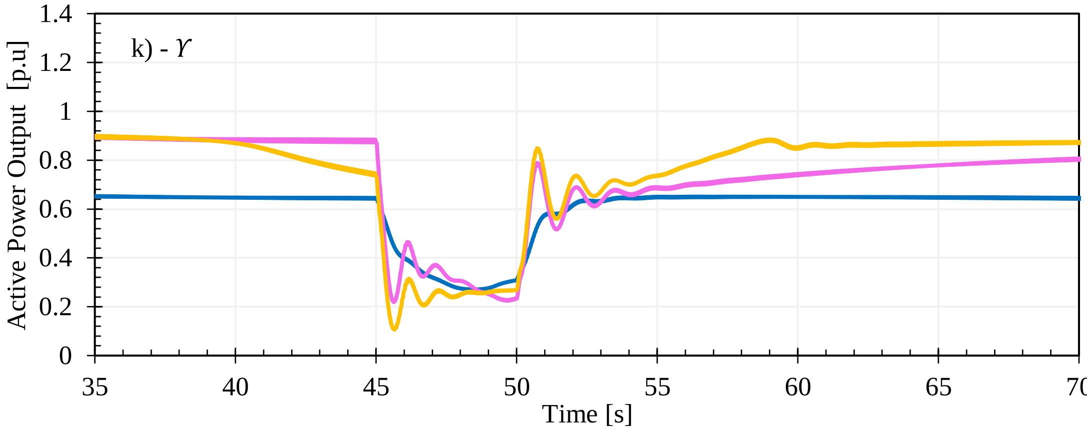
k) - Υ
Active Power Output [p.u]
1.4
1.2
1
0.8
0.6
0.4
0.2
0
35
40
45
50
55
60
65
70
Time [s]

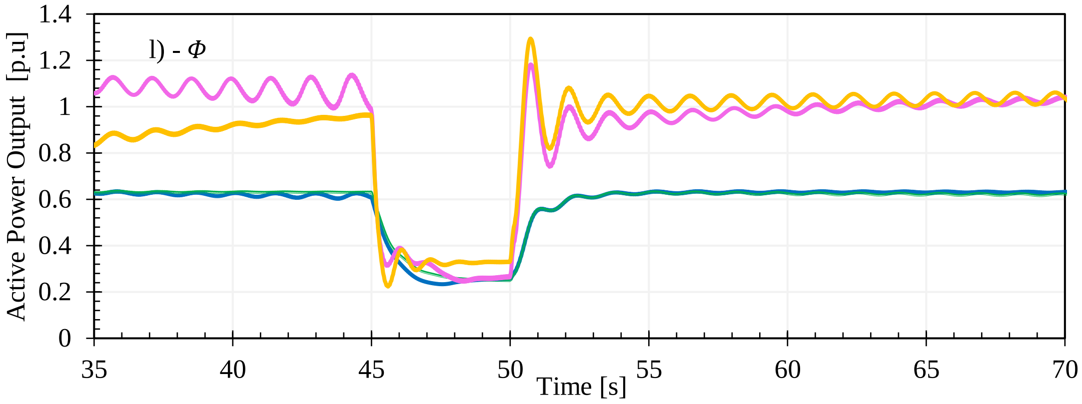
l) - *Φ*
Active Power Output [p.u]
1.4
1.2
1
0.8
0.6
0.4
0.2
0
35
40
45
50
55
60
65
70
Time [s]

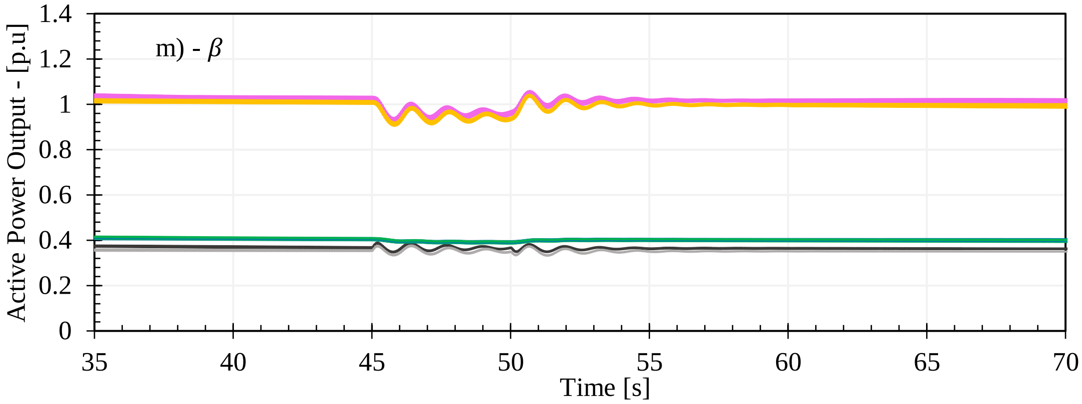
m) - *β*
Active Power Output - [p.u]
1.4
1.2
1
0.8
0.6
0.4
0.2
0
35
40
45
50
55
60
65
70
Time [s]

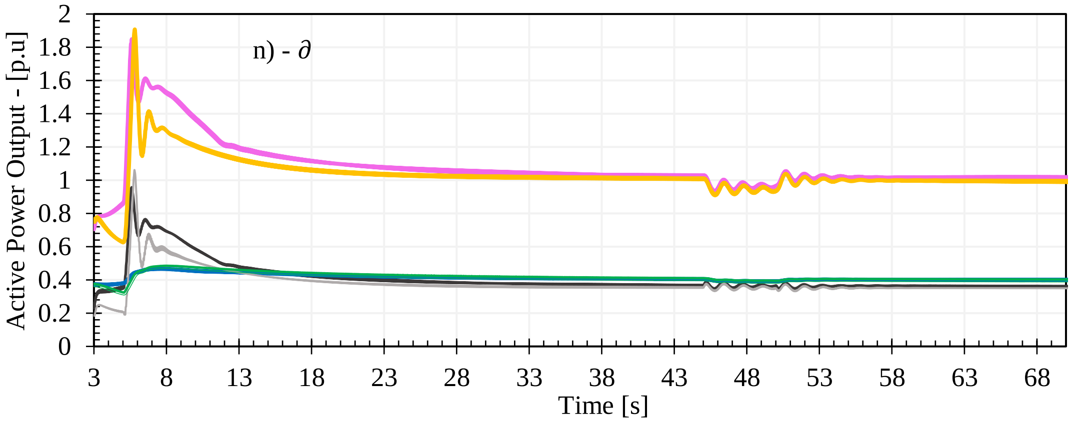
n) - *∂*
Active Power Output - [p.u]
2
1.8
1.6
1.4
1.2
1
0.8
0.6
0.4
0.2
0
3
8
13
18
23
28
33
38
43
48
53
58
63
68
Time [s]

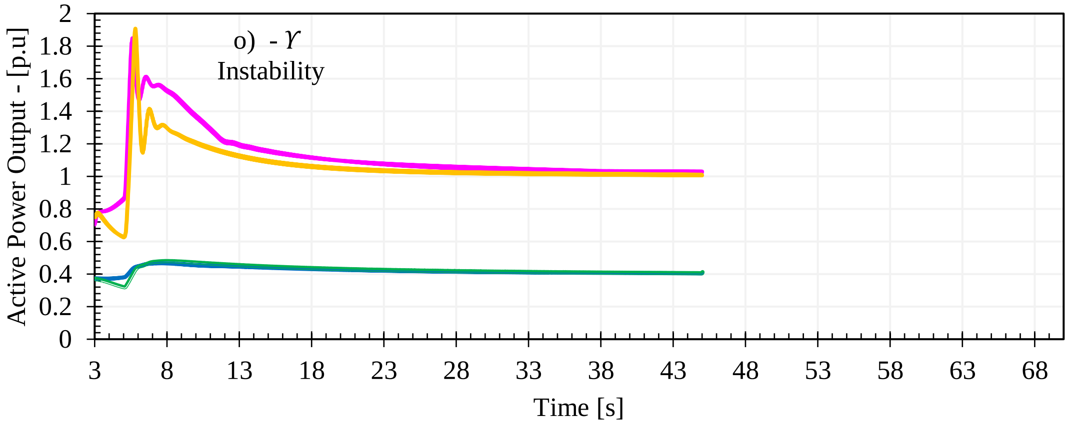
o) - *ϒ*
Instability
Active Power Output - [p.u]
2
1.8
1.6
1.4
1.2
1
0.8
0.6
0.4
0.2
0
3
8
13
18
23
28
33
38
43
48
53
58
63
68
Time [s]

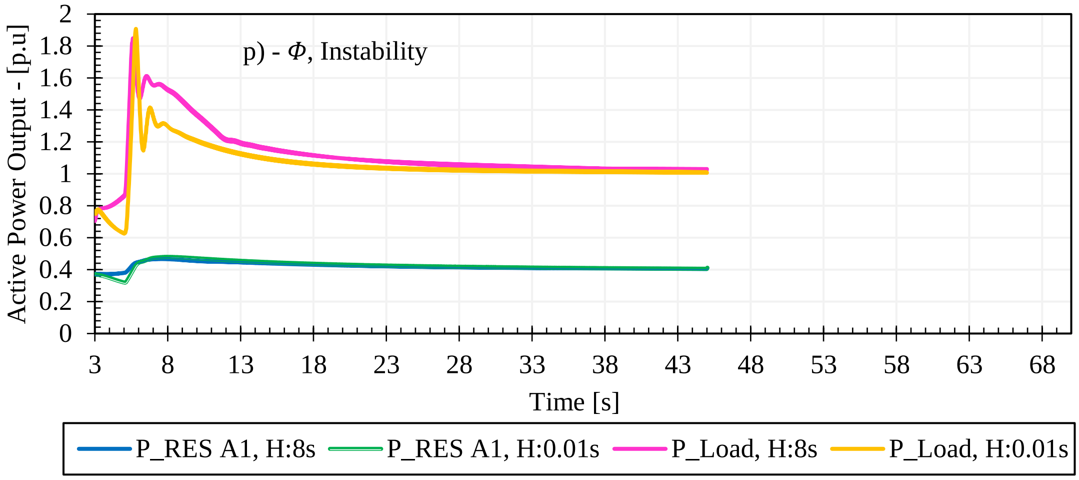

Figure 7.7. Load and RES Active power with SCR=10.

The trends in Figure 7.7 reveals the following aspects:

- in all simulations, the grid dynamic shows the typical trend occurring after a short circuit with a load loss depending on the unbalance between SG and RES. After the short-circuit is eliminated, the active power rises again to the steady-state value due to the action of the speed regulators of the diesel generators and the internal controls of the VSC;
- the active power trend has more significant oscillations when RES contribution is greater than 60% (Scenarios B1 and B2) of the load power and for the lowest value of R_{sc}. The grid stability improves using the angle compensation and a higher H_{vsm};
- Scenarios A1 does not present instability situations, even for low H_{vsm} and R_{sc} value. The positive behaviour of the system is due to the contribution both of the SG and of the control chosen for the VSC (RC-1) during the fault;
- on the contrary, in Scenario A2 in the presence of a low resistance short-circuit, the system gets instable when the control option RC-2 is chosen both for high and low H_{vsm} values;
- in Scenarios A2 and B2, thanks to the RC-2 control option, the system is more quickly stabilised. RC-2 control shows a better performance than RC-1 in steady-state, but in the presence of short circuits, it is not capable of maintaining the desired power output;

Starting from the results obtained for the strong grid, an analysis for the successful cases from Figure 7.7 is done for a weak grid (SCR = 3), considering the groups A1: Figure 7.7 a), b), c), d) and B1: Figure 7.7 i), j), k), l).

The results of the simulations for the weak grid are reported in Figure 7.8.

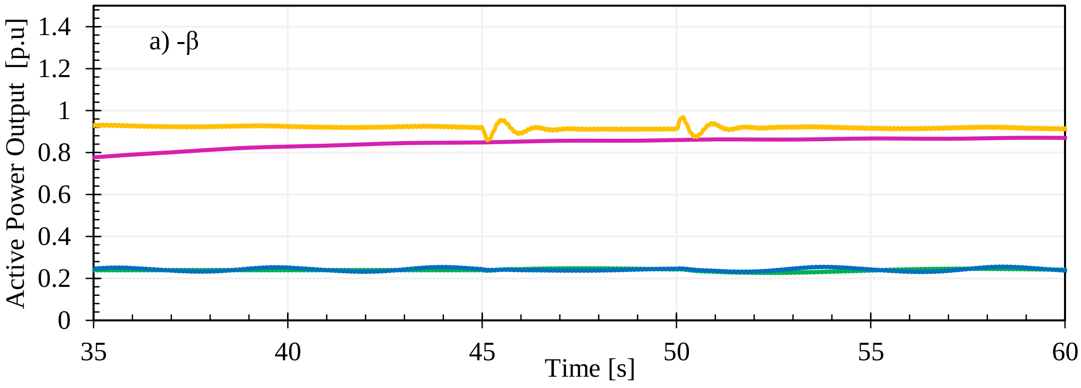

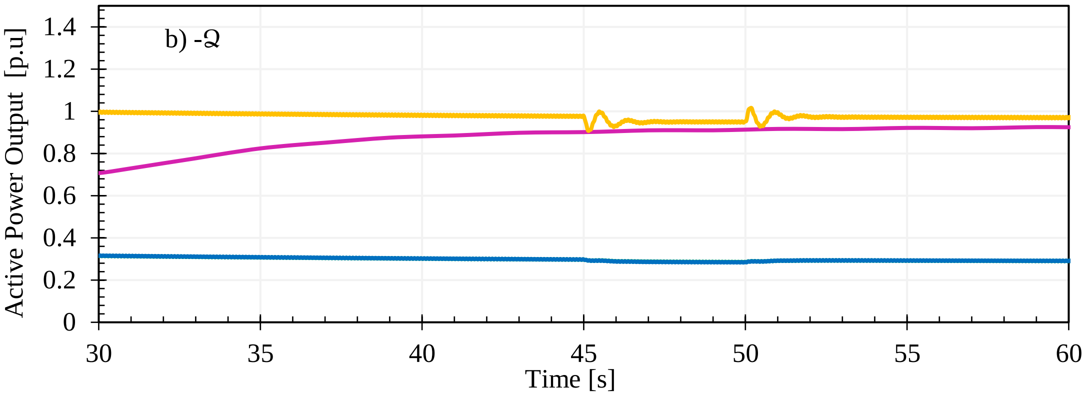
b) -Ω
Active Power Output [p.u]
0
0.2
0.4
0.6
0.8
1
1.2
1.4
30
35
40
45
50
55
60
Time [s]

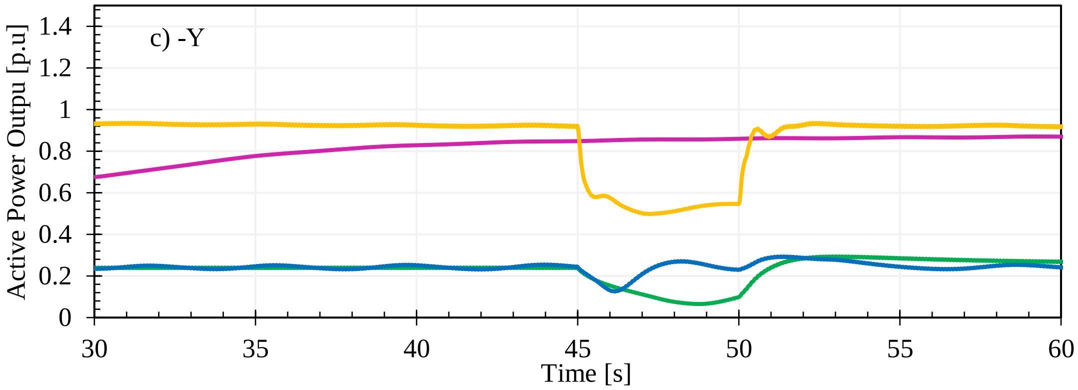
c) -Y
Active Power Outpu [p.u]
0
0.2
0.4
0.6
0.8
1
1.2
1.4
30
35
40
45
50
55
60
Time [s]

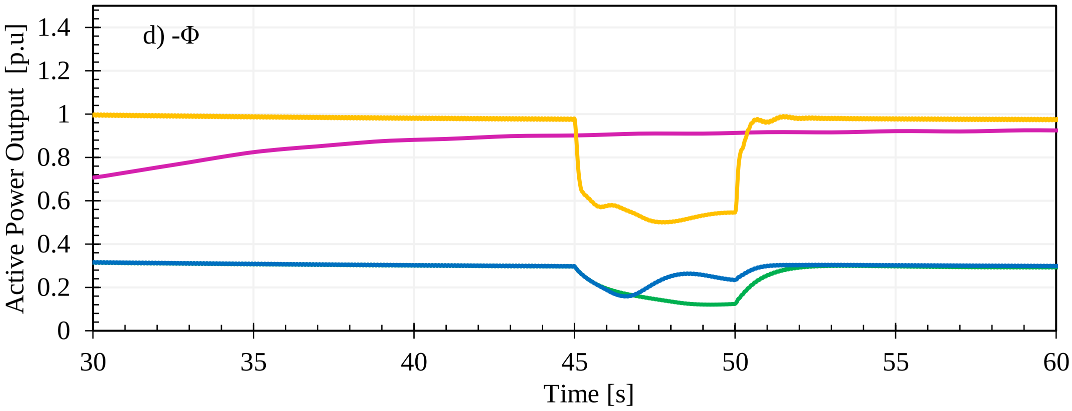
d) -Φ
Active Power Output [p.u]
0
0.2
0.4
0.6
0.8
1
1.2
1.4
30
35
40
45
50
55
60
Time [s]

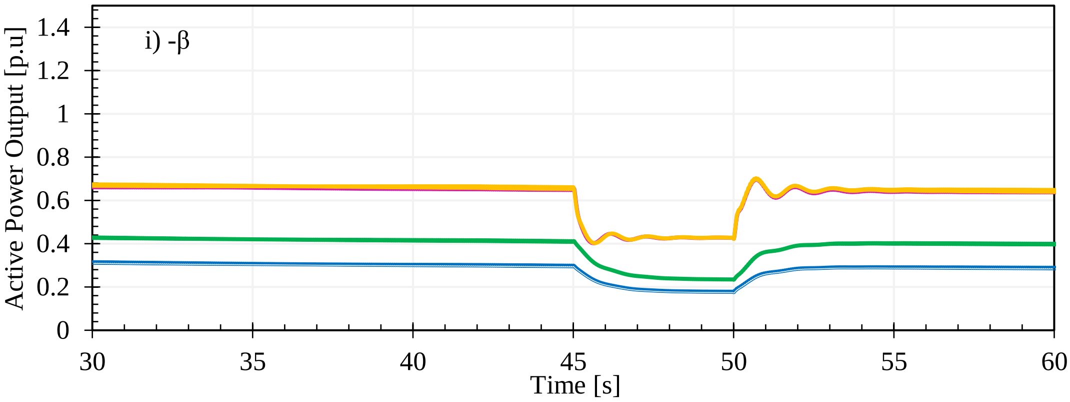
i) -β
Active Power Output [p.u]
0
0.2
0.4
0.6
0.8
1
1.2
1.4
30
35
40
45
50
55
60
Time [s]

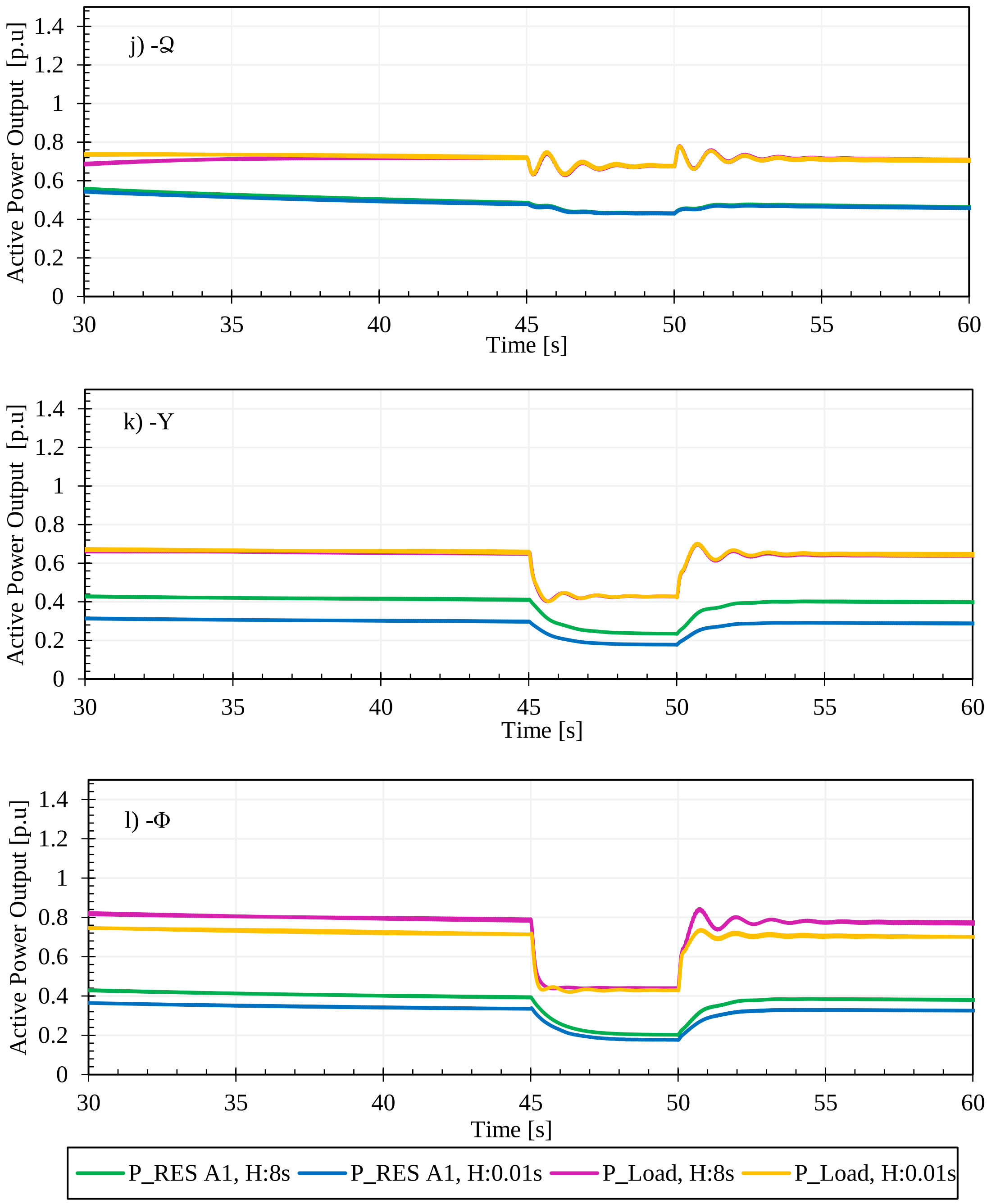

Figure 7.8. Load and RES Active power with SCR=3.

The trends in Figure 7.8 reveal the following aspects:

- in Scenario A1 no alterations are seen in the power generation from the VSC: it delivers the desired power to the load. On the other hand, in Scenario B1 the power production is reduced to 66%, and this creates a deficit in power generation during this hour;
- the lower is SCR (and so, as higher is the grid reactance Xg), the closer is the power contribution of the VSC to that of the SG. Note that mathematically this is obtained by calculating the SCR = S_{sc}/S, where S is the rated power and $S_{sc} = V^2/X_g$ is the grid short-circuit power;
- also in the presence of low SCR value, the behaviour of the VSC during the fault does not vary;

- the PCC voltage is significantly affected by SCR value, as shown in Figure 7.9, where the voltage variation during the fault is shown for both the robust and the weak grid.

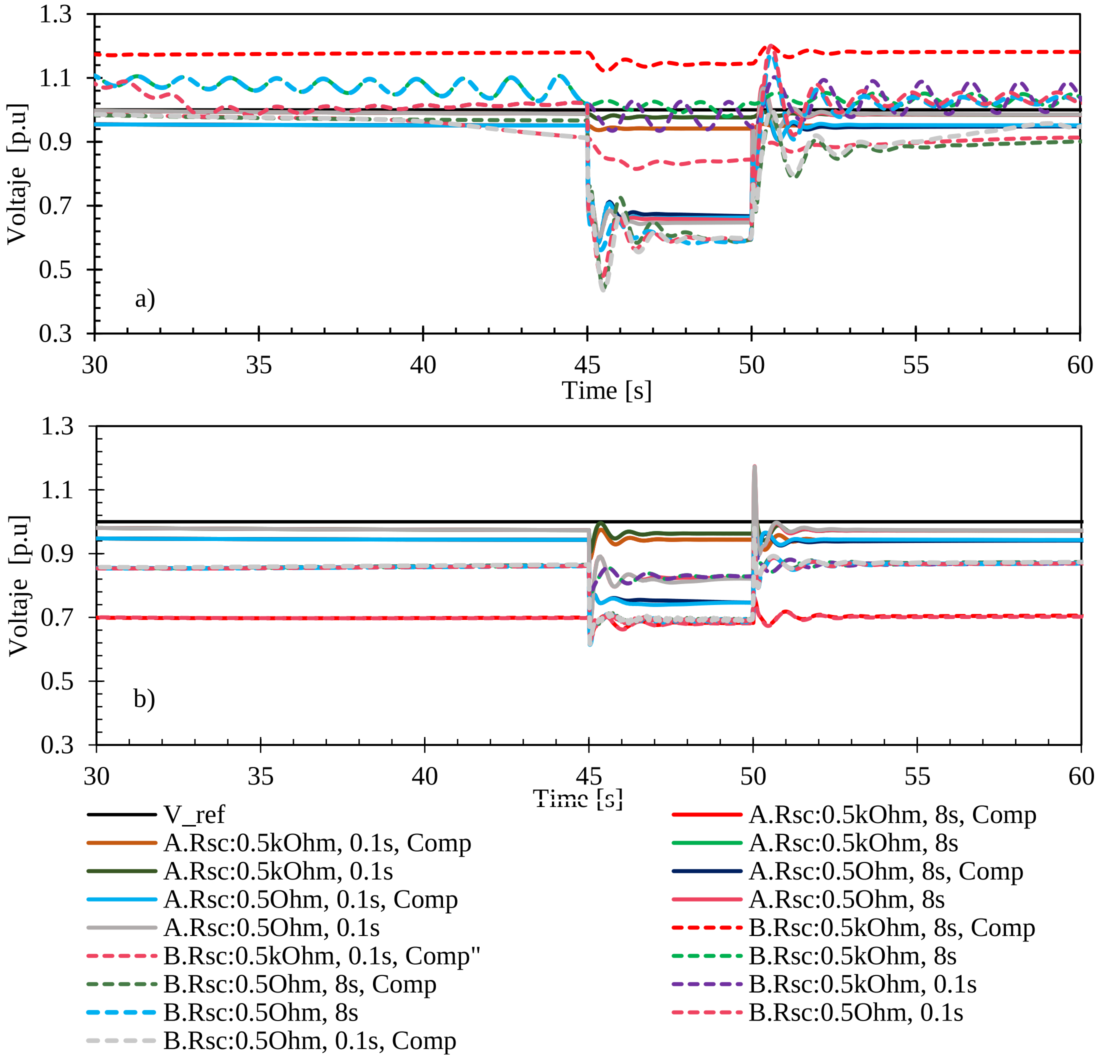

Figure 7.9. PCC voltage for cases A1 and B1 where a) represents SCR=10 and b) represents SCR=3.

Fig. 7 shows that:

- It is remarkable to see that there is a variation of PCC voltage when the power system operates at different transfer power conditions.
- Case A1 is negligible the SCR value.
- Case B1 with SCR=3 does not meet the minimum standard established for medium voltage.

7.4. Conclusion

The study shows the advantages of implementing a swing controller for RES-based generators on a small island in the presence of a double-phase short-circuit. The VSM+CCC model allows implementing virtual inertia and damping in the isolated micro-grid, improving grid stability. In the simulations, performed for the Island of Pantelleria in the Mediterranean Sea, the VSC active power output transients and the PCC voltage are observed. The study shows how the value of the SCR can influence the behaviour of the VSC.

Chapter 8

Use of BESS for providing Virtual Inertia in Small Islands.

8.1. Introduction

In this Chapter, the virtual inertia need of a small island is assessed considering several cases characterised by different RES production from an optimum energy mix obtained through a cost-benefit analysis. This analysis in the future will become fundamental for evaluating the feasibility for the transition of a traditional power system based on fossil fuel towards a renewable energy-based power system. Three cases are evaluated and compared: an approach based only on SGs (traditional system assumed as a base scenario), a system with SGs and RES-based generators, and, finally, the same system with SG and RES but where the SGs are activated following criteria that minimize the electricity generation cost. Then, the inertial response analysis of the three cases is performed. Finally, for the third case, a battery energy storage system (BESS) is calculated to compensate for the reduction of IR in the power system. Finally, some considerations about the sizing and cost of the BESS for providing VI to Pantelleria Island are reported, based on a comparison with the literature.

8.2 Methodology

This part of the study is divided into three different steps:

- First step: by using the optimization algorithm presented in chapter 5, the optimal size of varying power plants able to satisfy a fixed share of the energy demand is found. The best choice of the energy mix is represented by the one that has the lowest LCoE. Wind, solar and sea wave energy are considered as renewable energy sources.
- Second step: the optimal combination of the RES plants with the conventional SGs is analysed to supply active power to the typical load profiles of the island. In this step, three RES generation hypotheses (minimum, average and maximum production) from the first step, are considered for three cases.
- Third step: the dynamic grid stability is theoretically assessed by conducting an IR analysis of the power system [124], [125], including the RES trend and assuming that the RES does not have inertia due to the power electronics components [48]. In this way, the minimum, maximum and average inertia of the power system is calculated from the IR hourly trend, and it is verified if the system requires the addition of a BESS for providing VI [77], [126], [127]. The BESS system is sized in the examined cases to give the needed VI.

8.3. Case Study

8.3.1. Data for the analysis

The island of Pantelleria is taken as a case study for this analysis. The total rated power of the SGs is 24.5 MVA. Table 8.1 shows the rated capacity of each SG and the corresponding inertia constant.

Table 8.1. Rated power of SGs installed in Pantelleria.

Identification	Rated power [MVA]	Inertia constant [s]
G1	1.25	1.45
G2	5.04	3.24
G3	3.07	2.31
G4	2.92	2.24
G5	3.09	3.05
G6	2.65	2.12
G7	1.76	1.69
G8	5.22	3.31

Figure 8.1 shows the map of Pantelleria. GIS information is overlapped, considering the presence of reserved areas (green and light blue), as well as the airport (yellow). The depth of seabed is added to find suitable locations for sea wave exploitation.

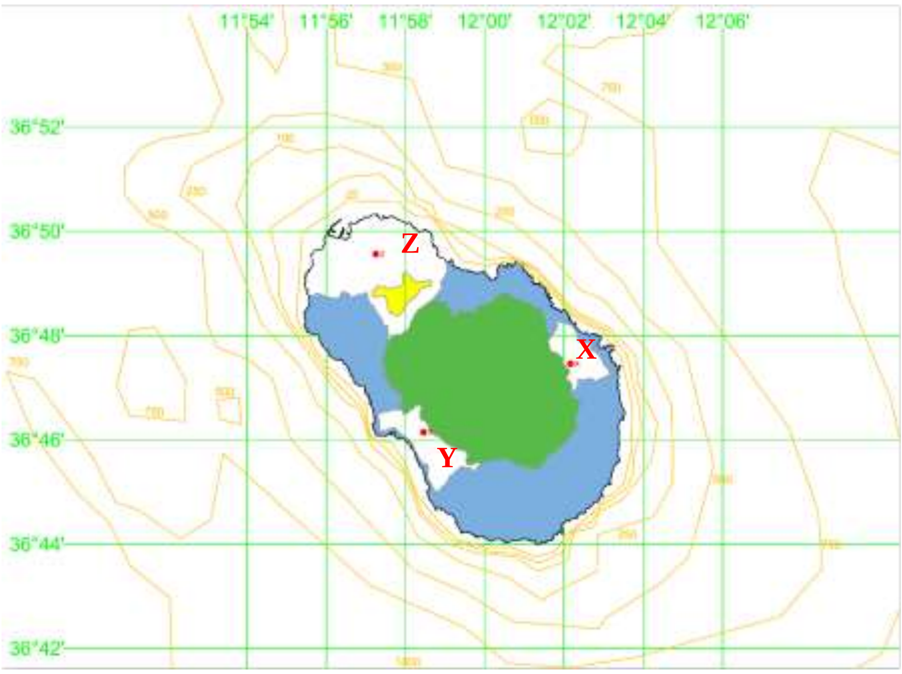

Figure 8.1. GIS map of Pantelleria.

In Figure 8.1, three red points, X, Y, Z, are represented showing the locations of RES supplied technologies. In detail:

- wind turbines can be installed only in X and Y, avoiding any interference with the airport;
- PV plants can be established in a distributed way in the entire territory; thus, all reference points are considered;

- sea wave can be installed only in the northern area, where the sea depth is limited (reference point Z);
- geothermal energy can be exploited only in Y reference point (close to the source).

A modular approach is also adopted. For each technology, the following RES rated powers have been assumed: 3.3 kW for PV, 80 kW for sea wave, 250 kW for wind turbines and geothermal steam turbines. Only one reference day is considered for each month (15th day). Table 8.2 reports the characteristics of the PV modules considered in the study, while the selected wind turbine data are reported in Figure 8.2.

Table 8.2. Main parameters of photovoltaic modules.

Model	HIT VBHN330SJ53
Number of cells per panel	96
Maximum power rating	330 W_p
Max. Power at NOCT	251.9 W
NOCT	44°C
Open circuit voltage	69.7 V
Short circuit current	6.07 A
Module efficiency	19.70%
Temperature Coefficient (Pmax)	-0.258%/°C
Temperature Coefficient (Voc)	-0.164V/°C
Temperature Coefficient (Isc)	3.34mA/°C
Dimensions	1590x1053x40 mm
Weight	19 kg

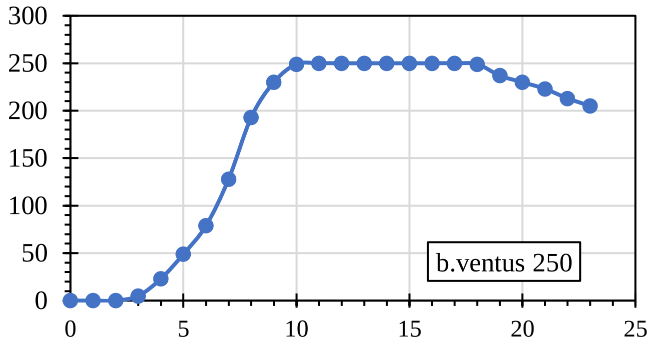

Model	b.ventus 250
Nominal power	250 kW
Cut-in wind speed	2.5 m/s
Nominal wind speed	9.0 m/s
Cut-out wind speed	23 m/s
Rotor diameter	42.54 m
Rotor area	1421 m^2
Tower height	28.37 m
Voltage	400 V (AC)
Frequency	50 or 60 Hz
n. blades	3

Figure 8.2. Data of the selected wind turbine.

Data on solar radiation are available from the online GIS tool PVGIS, a European instrument usable to perform preliminary energy assessments [128]. The total monthly solar radiation on a horizontal surface is reported for the three reference points in Figure 8.3. For each reference point, hourly data are extracted considering 12 years (2005 – 2016) for the 15th day of each month. As an example, see Figure 8.4 about January in reference point X.

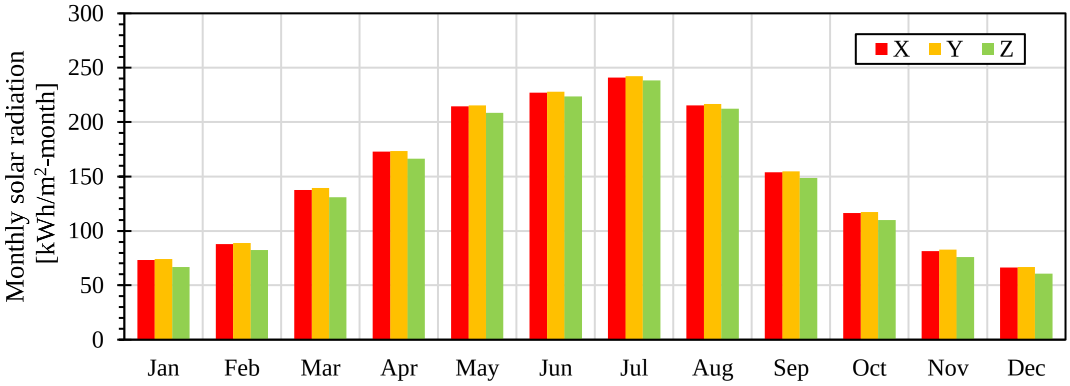

Figure 8.3. Monthly solar radiation in Pantelleria.

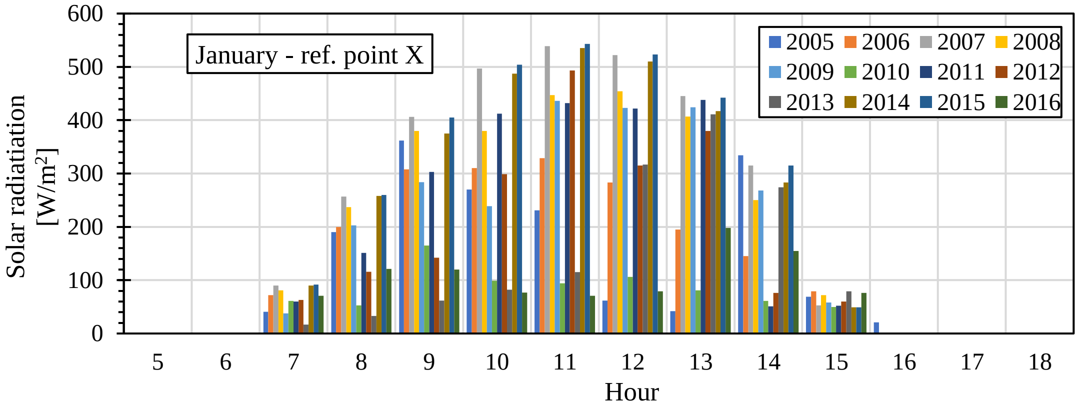

Figure 8.4. Hourly solar radiation in 12 years during January in the reference point X of Pantelleria.

The same GIS tool also contains information on wind speed, measured at 10 m above the ground. In this case, only X and Y reference points are considered. Since the wind turbine should be installed at 28 m from the ground data are preliminarily modified, considering Equation 8.1, according to IEC 61400-1 [129]:

$$v_z\langle t\rangle = v_{z,ref}\langle t\rangle \frac{\ln\left(\frac{z}{z_0}\right)}{\ln\left(\frac{z_{ref}}{z_0}\right)} \tag{8.1}$$

where $v_z\langle t\rangle$ is the time-dependent wind speed at the height z above the ground, $v_{z,ref}\langle t\rangle$ is the time-dependent wind speed at the reference height z_{ref}, finally, z_0 is an equivalent length related to the local orography. For both reference points, the probability function of wind speed availability in each month is evaluated. Data are scaled considering a year; thus, the annual distribution is equal to the sum of the monthly distributions here reported.

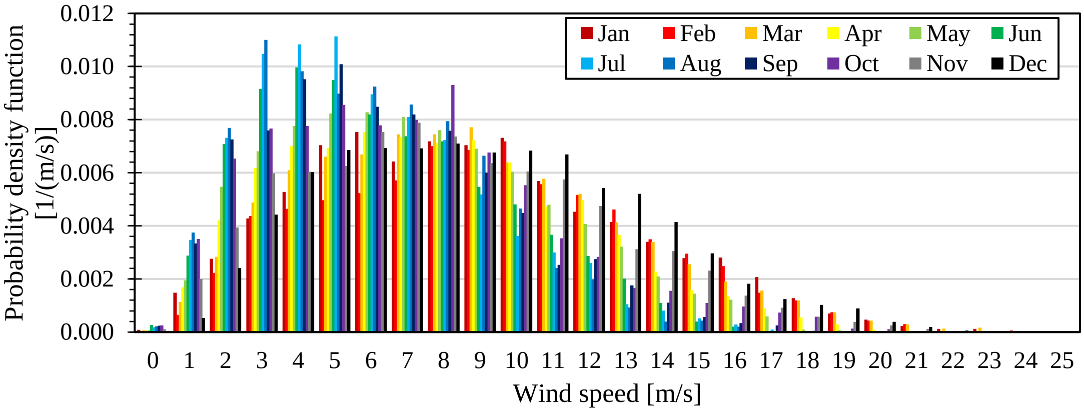

Figure 8.5. The probability density function of wind speed at 28 m from the ground each month.

As well as solar radiation, hourly wind speed data were also extrapolated for the 15th day of each month, as shown in Figure 8.6.

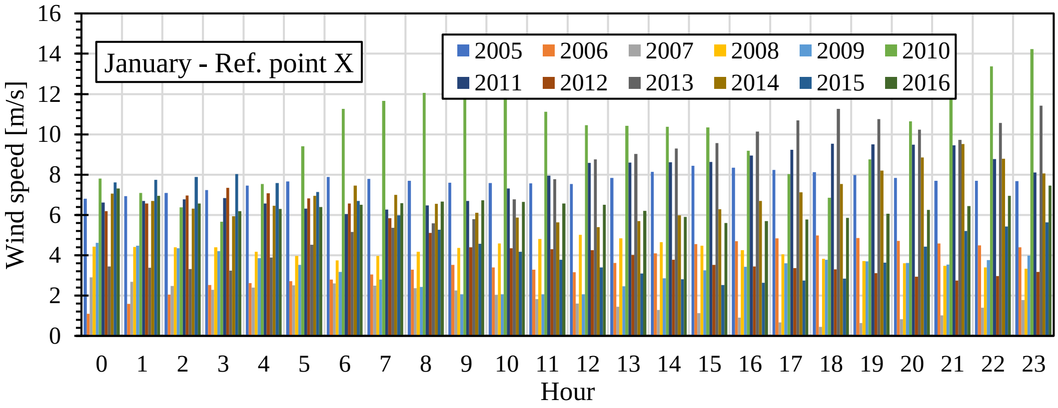

Figure 8.6. Wind speed in 12 years during January in the reference point X of Pantelleria

Sea Wave is the last unprogrammable energy source considered in this assessment. Some data are available from the RON (Italian acronym of "Rete Ondametrica Nazionale") buoy measuring grid [130]. The closest station is Mazara del Vallo (lat. 37.518°N, long. 12.533°E). Data are almost complete in the years 2003, 2004, 2005, 2006, 2010 and 2011 [131]. Then, the average wave energy flux and the hourly trends are obtained, as reported in the examples in Figure 8.7 and Figure 8.8.

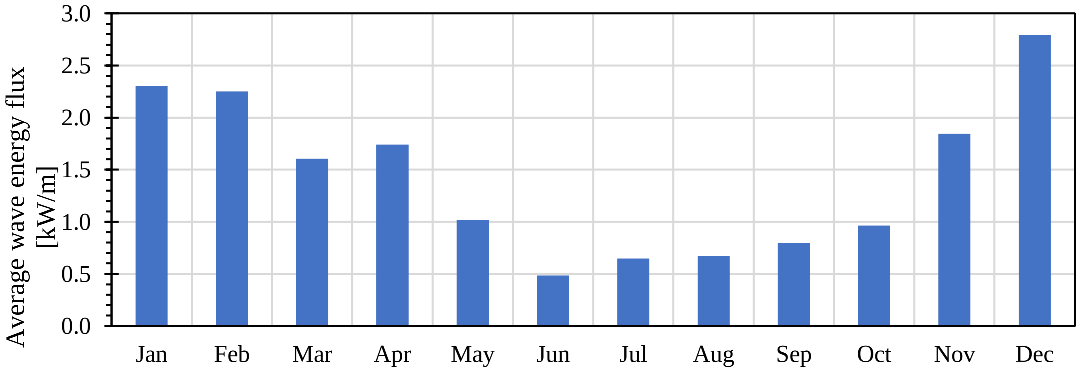

Figure 8.7. Monthly average wave energy flux in Pantelleria.

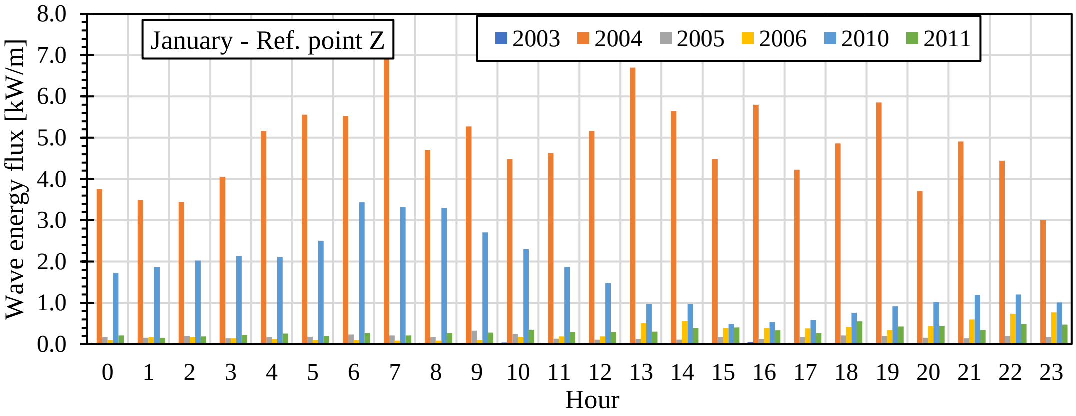

Figure 8.8. Hourly wave energy flux in Pantelleria.

Finally, the last renewable energy source is geothermal. Unlike the previous RES, geothermal energy can be used as a programmable energy source, with the possibility to follow the trend of the local energy demand. In the past, studies were performed to evaluate the potential energy source in Pantelleria [73], [132]. According to these reports, a possible geothermal power plant can be installed in Pantelleria, with a rated power until 2.5 MW, corresponding to the estimated energy production of 20000 MWh/y. Table 8.3 reports the economic parameters used for calculating the optimal energy mix that minimizes the LCoE. Data are obtained from the literature [93], [133], [94].

Table 8.3. Investment and operative and maintenance costs for renewable energy sources.

Technology	Investment	O&M costs
Wind turbine	1212.57 €/kW	42.12 €/(kW-year)
Solar PV	980.10 €/kW	12.15 €/(kW-year)
Sea wave converter	5020.00 €/kW	75.00 €/(kW-year)
Geothermal turbine	4353.00 €/kW	115.00 €/(kW-year)
Inverter	100.00 €/kW	10.00 €/(kW-year)
Battery	600.00 €/kWh	60.00 €/(kWh-year)

The inflation rate for the energy sector was fixed to 2.993%, by considering the trend of diesel price in Italy [134]. The interest rate was set equal to 1.14% [95]. The desired share of RES production was varied up to 70% with a step of 5%.

8.3.2. Calculation of the optimal energy mix

For each condition, the configuration that minimizes the LCoE parameter was identified using the algorithm introduced in Chapter 5. The numbers of required plants for each reference point and technology are reported in Table 8.4.

The details of the energy contribution inside the RES share is depicted in Figure 8.9.
In any case, the LCoE evaluation shows an almost linear trend with the RES share, as shown in Figure 8.10.

Table 8.4. Size of the optimal energy mix fora different share of energy demand.

RES Share	Number of plants						
	Wind		PV			Sea wave	Geo
	X	Y	X	Y	Z		
5%	0	1	58	27	0	1	0
10%	2	0	0	31	161	2	0
15%	1	2	0	47	0	13	0
20%	5	0	16	53	0	9	0
25%	0	2	0	84	36	13	2
30%	0	2	0	0	147	9	3
35%	1	1	104	6	1	8	4
40%	0	5	115	0	18	10	3
45%	1	4	101	58	1	7	4
50%	0	2	80	37	66	14	6
55%	3	1	106	63	6	13	6
60%	1	3	102	59	76	10	7
65%	1	1	129	85	28	12	9
70%	3	2	61	90	72	11	9

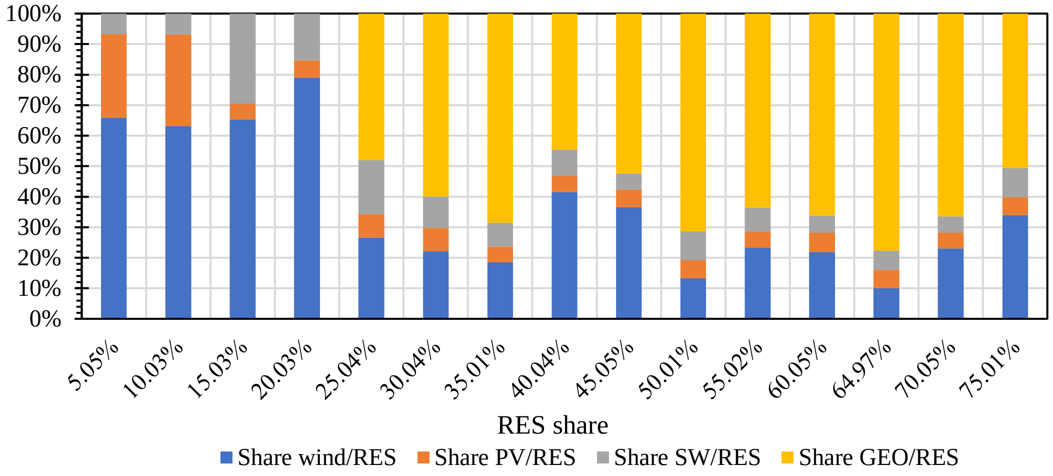

Figure 8.9. Contribution of renewable energy sources at different RES share

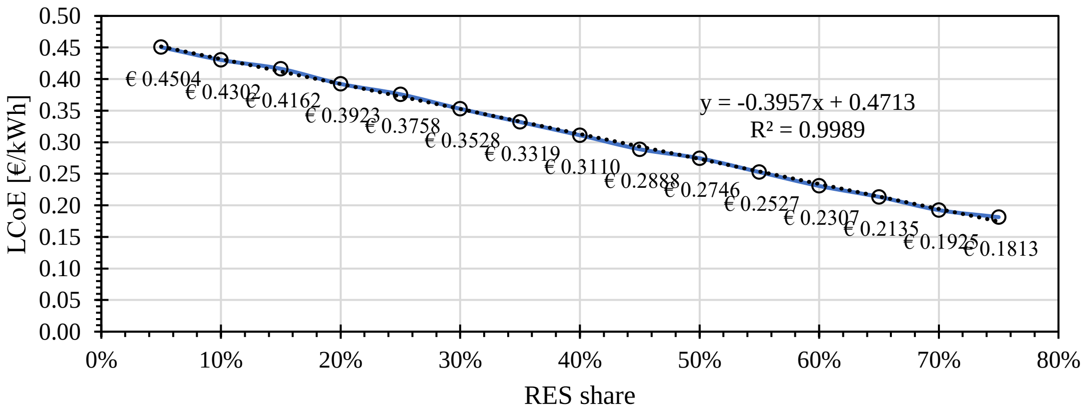

Figure 8.10. LCoE trend at different RES portions.

The best energy mix from an economic point of view requires the inclusion of 70% of RES with the installation of:

- 735.9 kW of PV plants (223 small plants with rated power 3.3 kW each);
- 1250 kW of wind plants (5 wind turbines with rated power 250 kW each);
- 880 kW of wave energy plants (11 wave converters with rated power 80 kW each);
- one 250 kW geothermal turbine.

In this way, the estimated annual electricity production is equal to 1304.98 MWh/year for solar panels, 5891.8 MWh/year for wind turbines analysed, 1368.9 MWh/year for sea wave energy converters and 16978 MWh/year for geothermal. The investment cost of only the RES is 16,448,818 €.

8.3.3. Inertia Response evaluation

Starting from the above results, the inertia response of Pantelleria power system is evaluated in three cases:

- Case_0: only SGs (the electricity generation profiles of the year 2017 are assumed as a base for the calculation);
- Case_1: a combination of the SGs and the RES mix above calculated.
- Case_2: a combination of the SGs and the RES mix above calculated where the operation of the SG units is managed in order to minimize their production cost.

For Case_1 and Case _2, three conditions are examined: minimum, average and maximum production from RES.

The daily power profile for Case_0 is represented in Figure 8.11.

Figure 8.11 shows that:

- the monthly load trends regularly vary by 20% among every hour;
- the lowest load is in winter, and the highest load is in summer;
- the minimum load peak is 5.9 MVA at 8 pm in January;
- the maximum load peak is 8.5 MVA at 9 pm in August;
- the highest load corresponds to 44.2% of the installed active power.

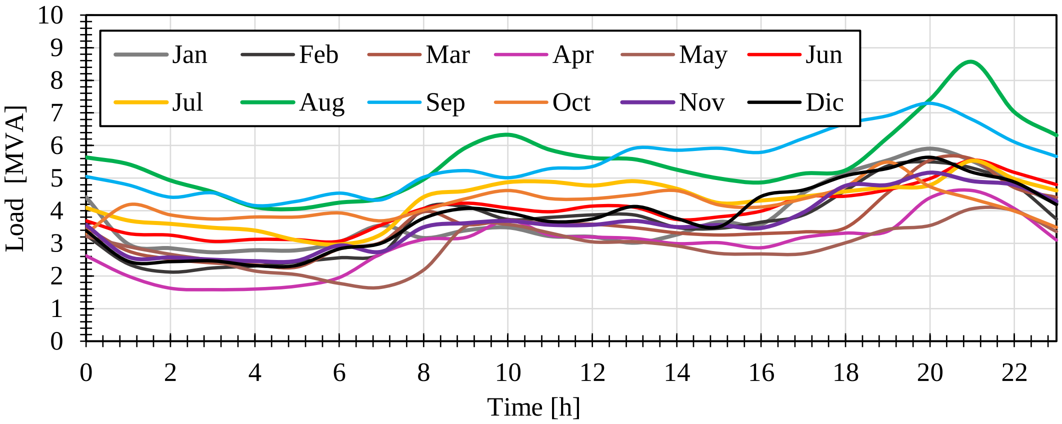

Figure 8.11. Daily power profiles for Case_0.

In Case_1 the RES plants produce at their maximum and the traditional power plants generate the missing electricity production for compensating the load demand. In this context, the RES inclusion automatically causes the disconnection of 2/3 of SG production with respect to Case_0. Figure 8.12 represent the electricity generated by SGs and RES plants in Case_1. The graphs in Figure 8.12 are divided into two groups. The first group refers to the months from January to June. RES production is assumed minimum in Figure 8.12 a), average in Figure 8.12 b) and maximum in Figure 8.12 c). The second group refers to the months from July to December, RES production minimum (d), average (e) and maximum (f).

The comparison of the hourly electricity productions shows that:

- RES trends of both groups present peaks between 6 am to 6 pm due to the presence of the PV plants;
- the decrease in electricity production from SGs is the function of the three levels of electricity production from RES. Therefore, the higher the RES production, the lower the SGs production;
- maximum and average RES levels show a good interaction based on the cost-benefit of the investment of the RES plant.

In Case 2, the SGs are managed to minimize the electricity generation cost from traditional plants. The optimization algorithm used searches hourly the optimal rated power, through the verification of the capacity of each SG from Power Plant. In this way, the algorithm first calculates the value that the power capacity should have, as a result of: S_{SG}= S_{load} - S_{RES}, where S_{RES} represents the electricity production by the RES and S_{load} represents the apparent power required by the demand.

Then, the safety margin of 30% of the hourly power demand is added (internal reserve of SG and FCR-indicated as S_R). Finally, the value of the power capacity is calculated as: SG_1 = S_{SG_0}+ S_R, where SG_1 must be matched by each SG in the exchange, until its value is reached. Firstly, the use of a single SG is considered, while two SGs are regarded as a second option. Furthermore, the condition that each SG group can participate in energy production only for 12 hours a day is considered. In this way, the apparent power of the SGs in service for each hour of each day of the months considered for minimum, average and maximum RES production are assessed.
Using equation 2.2, the system inertia is calculated hourly for the three cases and represented in Figure 8.13. (a: Case_0; b: Case_1 minimum RES production; c: Case_1 average RES production; d: Case_1 maximum RES production; e: Case_2 minimum RES production; f: Case_2 average RES production; g: Case_1 maximum RES production).

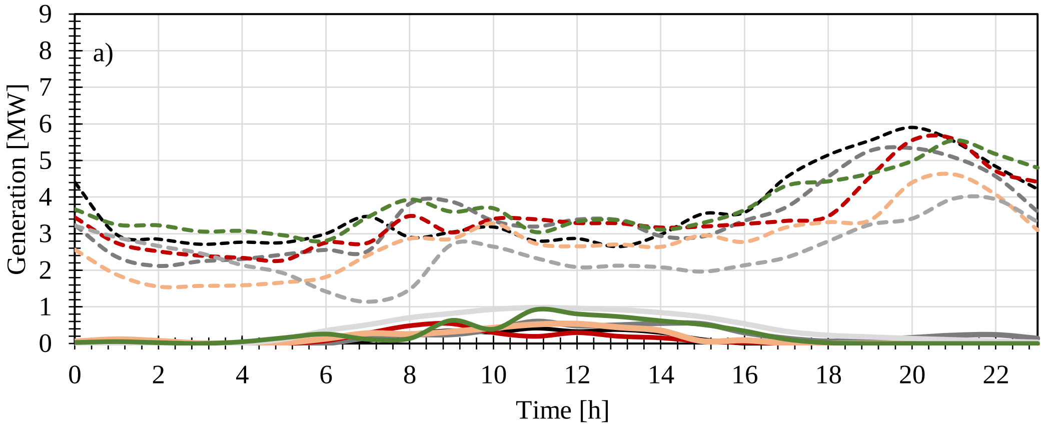

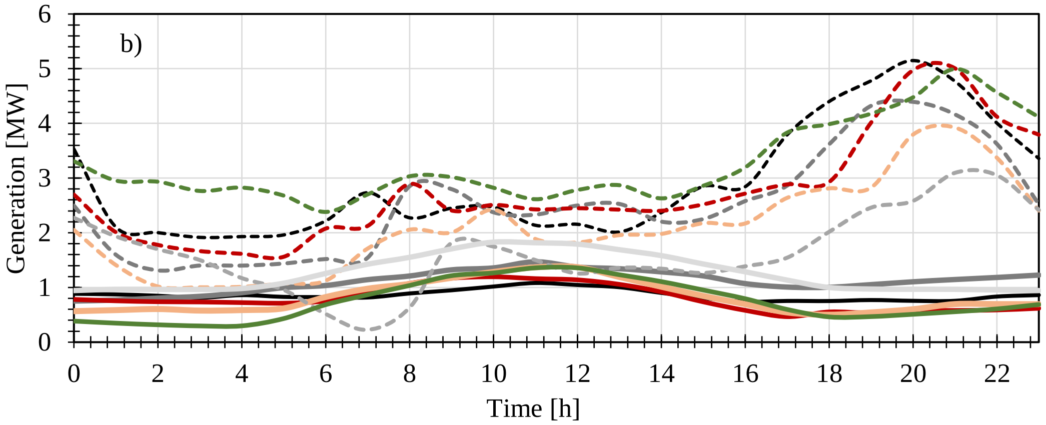

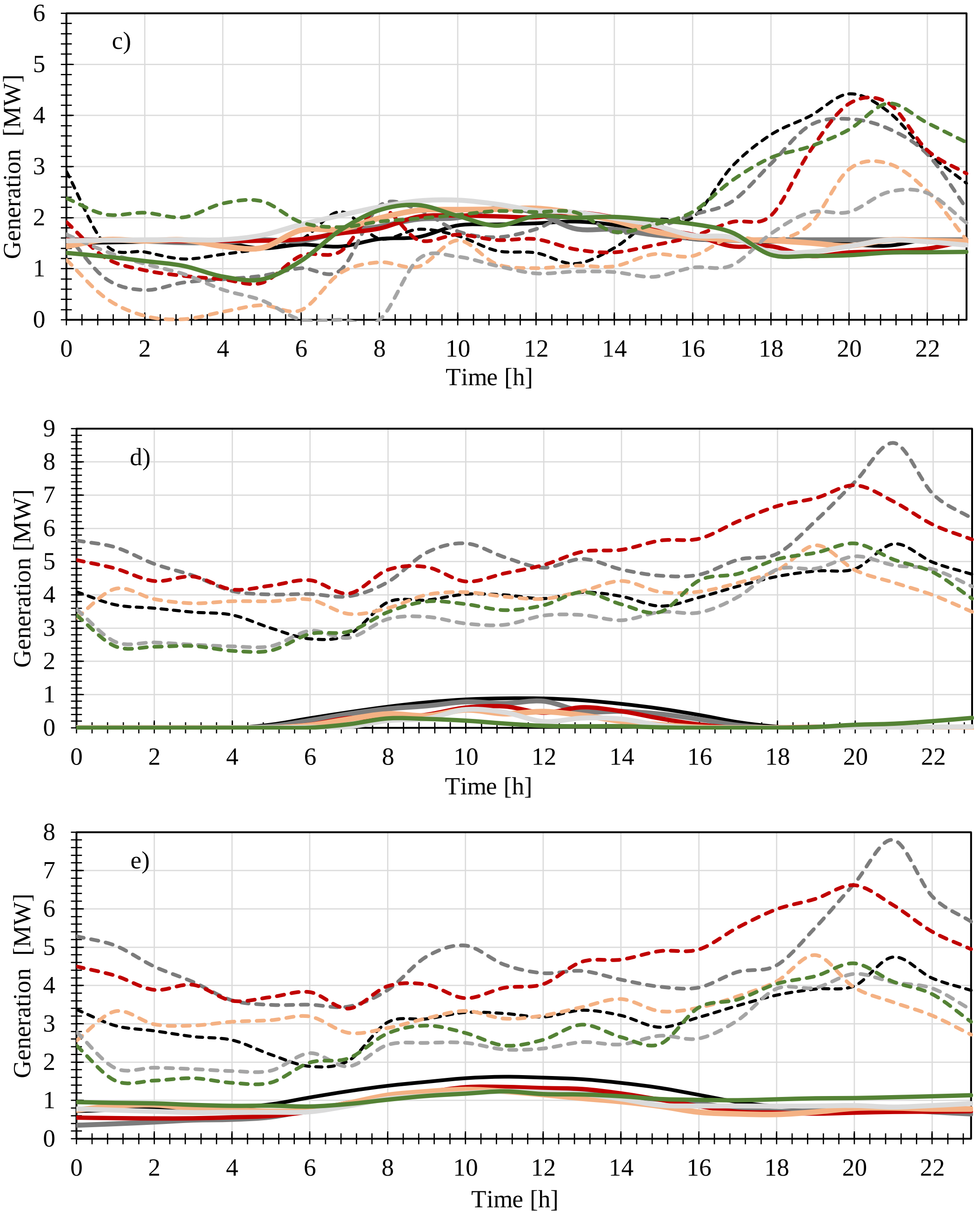
c)
Generation [MW]
0
1
2
3
4
5
6
0
2
4
6
8
10
12
14
16
18
20
22
Time [h]
d)
Generation [MW]
0
1
2
3
4
5
6
7
8
9
0
2
4
6
8
10
12
14
16
18
20
22
Time [h]
e)
Generation [MW]
0
1
2
3
4
5
6
7
8
0
2
4
6
8
10
12
14
16
18
20
22
Time [h]

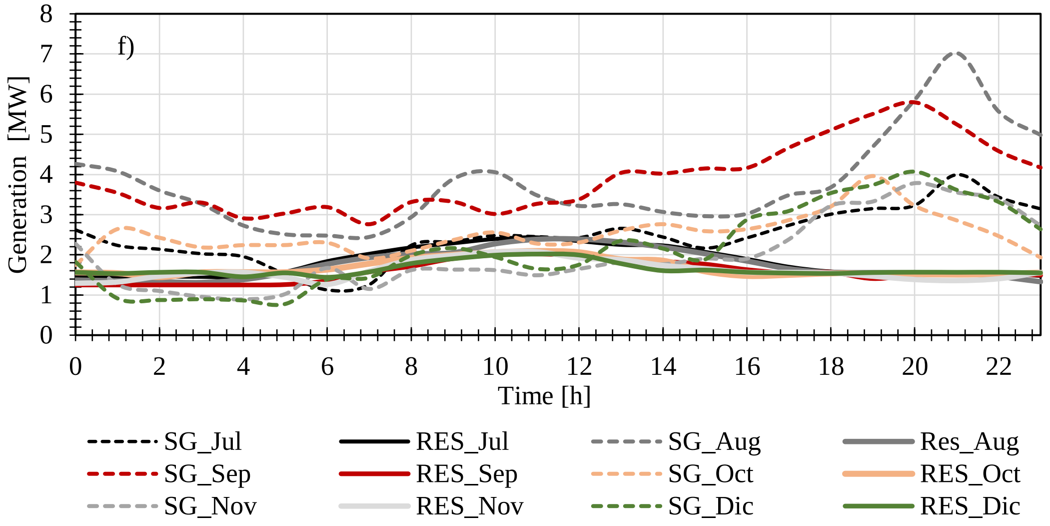

Figure 8.12 Yearly electricity generated by SGs and RES plants from Case_1.

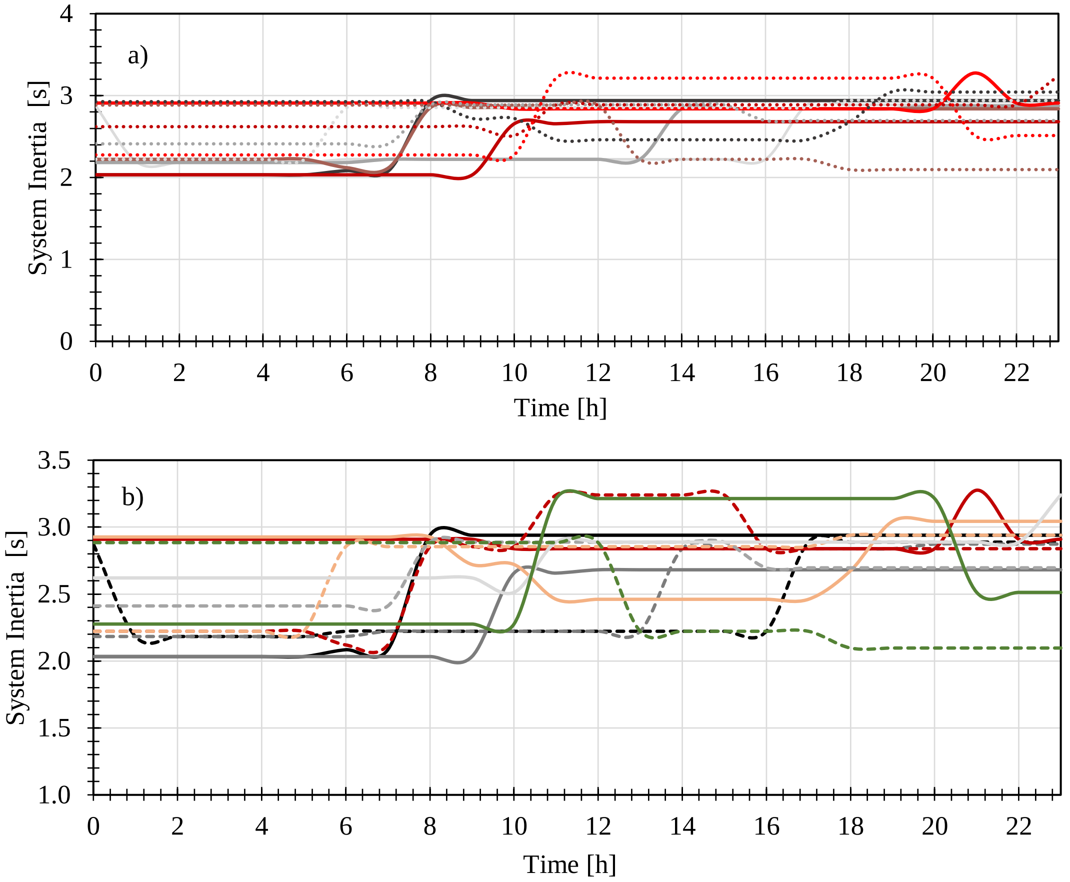

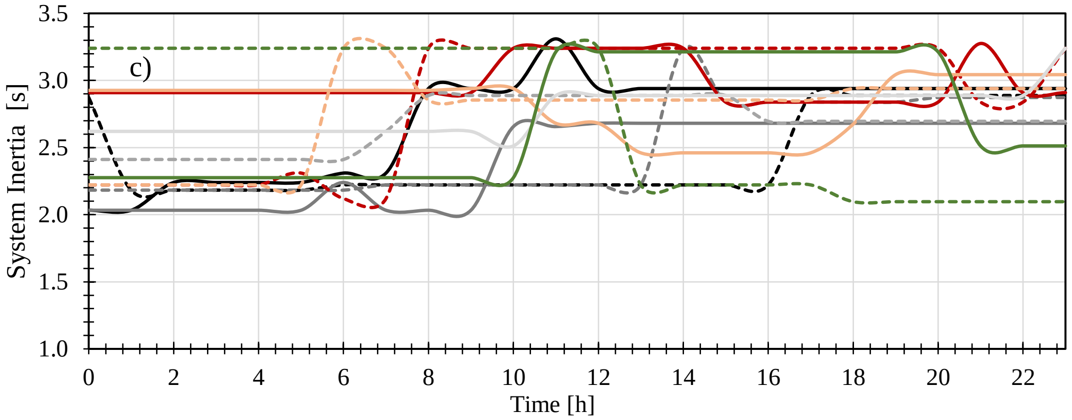
c)
System Inertia [s]
3.5
3.0
2.5
2.0
1.5
1.0
0
2
4
6
8
10
12
14
16
18
20
22
Time [h]

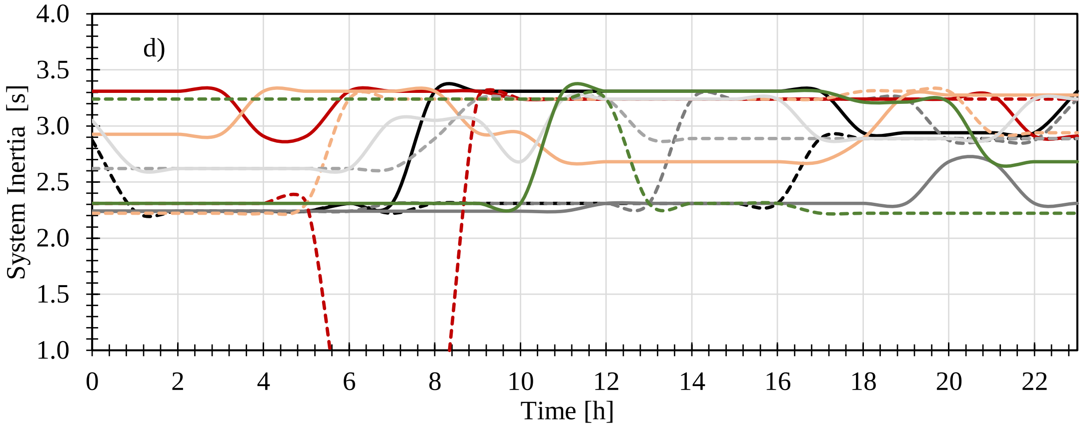
d)
System Inertia [s]
4.0
3.5
3.0
2.5
2.0
1.5
1.0
0
2
4
6
8
10
12
14
16
18
20
22
Time [h]

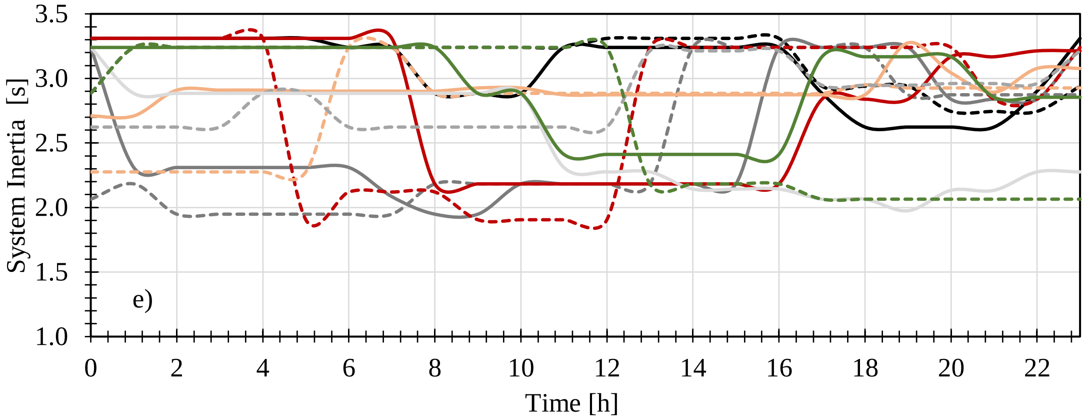
e)
System Inertia [s]
3.5
3.0
2.5
2.0
1.5
1.0
0
2
4
6
8
10
12
14
16
18
20
22
Time [h]

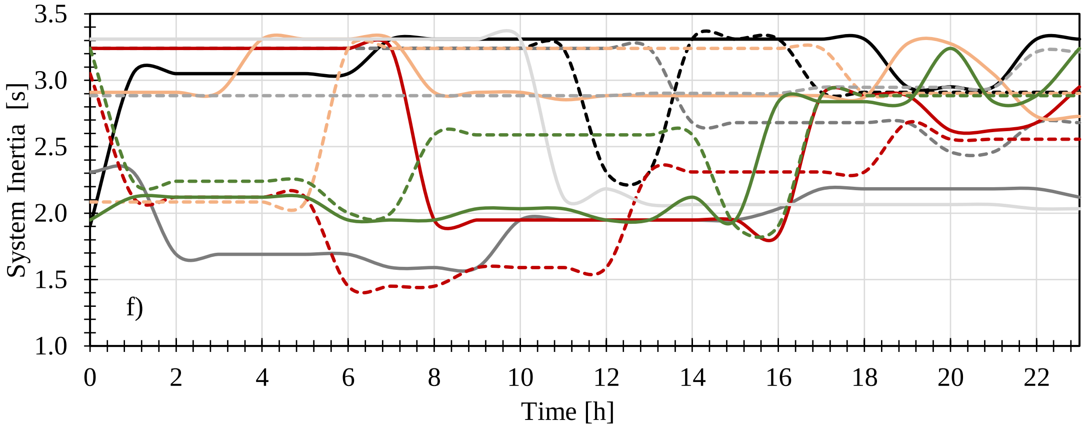
f)
System Inertia [s]
3.5
3.0
2.5
2.0
1.5
1.0
0
2
4
6
8
10
12
14
16
18
20
22
Time [h]

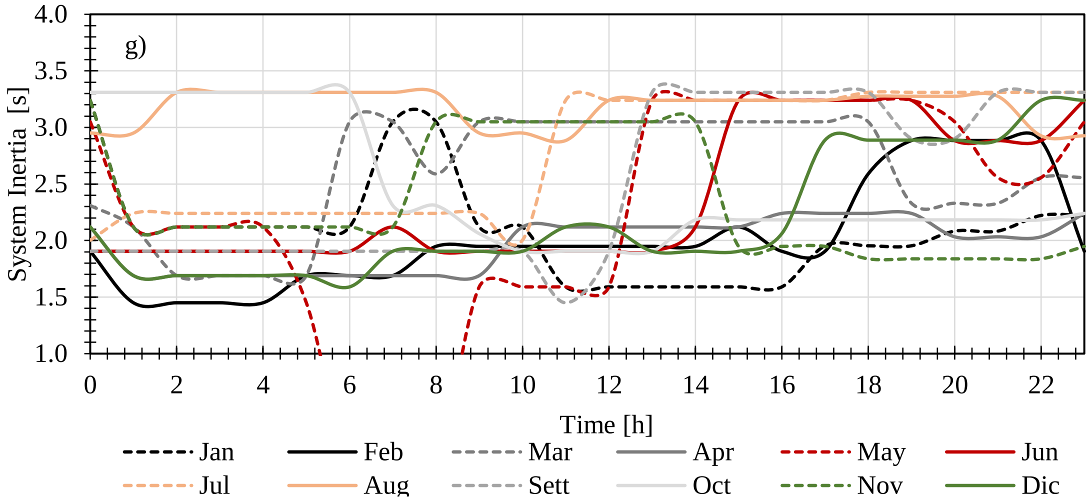

Figure 8.13. Yearly IR for Case_0, Case_1 and Case_2.

Table 8.5 synthetizes the minimum, medium and maximum system inertia for the three cases.

Table 8.5. Summary of IR from Figure 8.

Case	RES production	Minimum	Medium	Maximum
		H_{min}	H_{med}	H_{max}
		[s]	[s]	[s]
0	-	2.00	2.64	3.28
1	Avg	2.00	2.68	2.80
	Max	0	1.45	1.91
2	Avg	1.41	2.70	2.79
	Max	0	2.00	2.03

Starting from the data in Table 8.5, the maximum unbalance allowed for the island is calculated by the following formula derived from Equation 2.8:

$$\Delta P_{imbalance} = \frac{\Delta f_{max} D}{\left(e^{\frac{DT_d}{2H_{sys}}} - 1\right)} \tag{8.2}$$

where, $T_d = 2.7\ s$ is the response time of the DG, $D = 1\%$ represents the load frequency dependence, Δf_{min} is the maximum frequency deviation assumed equal to 2.5 Hz (frequency nadir for the island 47.5 Hz.

Table 8.6. Maximum load imbalance.

Case	RES production	$\Delta P_{imbalance}$		
		For minimum inertia [p.u.]	For average inertia [p.u.]	For maximum inertia [p.u.]
0	-	0.074	0.0995	0.121
1	Avg	0.074	0.0995	0.104
	Max	0.0005	0.054	0.071
2	Avg	0.052	0.0995	0.104
	Max	0.0005	0.074	0.074

The IR can be improved by using BESS suitably interfaced to the grid by static converters controlled as described in the previous chapters. The sizing of the BESS for providing VI can be done according to the following procedure.

Firstly, the target system inertia is evaluated. It can be done using two different approaches:

- assuming the target inertia is equal to the minimum (or average) inertia of the system in the absence of RES-based static generators (values obtained in Case_0);
- as a function of the desired $RoCoF_{max}$ (if RoCoF protection is present) or Δf_{max}.

In the case $RoCoF_{max}$ is used for assessing the target inertia of the small island, the following equation must be used:

$$H_{target} = \frac{\Delta P_{imbalance} \cdot f_0}{2 . P_{load} . RoCoF_{max}} \tag{8.3}$$

In the case Δf_{max} is used, the following equation derived from Equation 8.2 must be adopted:

$$H_{target} = \frac{DT_d}{2ln\left(\frac{\Delta f_{max} D}{\Delta P_{imbalance}} + 1\right)} \tag{8.4}$$

In both cases, it is necessary to define the most critical condition in terms of imbalance in the grid. Then, the VI amount that must be provided by BESS is calculated using the expression:

$$H_{BESS} = \frac{f_0}{2\ RoCoF_{max}} \tag{8.5}$$

As an alternative, it can be imposed that the value of H_{BESS} is giving the best dynamic response of the BESS controlled by a VSM to the grid. For example, in Chapter 6, using a VI of about 8 s an excellent dynamic response of the VSM is obtained.

Finally, the rated power of the BESS is assessed by the following equation considering the worst operating condition in terms of inertia of the isolated power system:

$$H_{BESS} \cdot P_{BESS0,N} + H_{sys,min} \cdot \sum_j A_{nj} = H_{target} \cdot \left(P_{BESS0,N} + \sum_j A_{nj} \right) \tag{8.6}$$

from which it derives:

$$P_{BESS0,N} = \frac{H_{target} - H_{sys,min}}{H_{BESS} - H_{target}} \cdot \sum_j A_{nj} \tag{8.7}$$

To calculate the effective power exchanged by the storage system (P_{eff}), based on the charging efficiency (η_c) and discharging efficiency (η_d), the following equation is used:

$$P_{eff} = \begin{cases} \dfrac{P_{BESS,0}}{\eta_d} \\ P_{BESS,0}\eta_c \end{cases} \tag{8.8}$$

When $P_{eff} > 0$, the storage discharges, vice versa the storage charge. Note that the behaviour of the storage depends on the actual State of Charge (SoC,) given by:

$$SoC = SoC_0 - \frac{\int P_{eff}}{E_{BESS}} \% \tag{8.9}$$

SoC_0 represents the initial state of charge and E_{BESS} represents the capacity of the batteries, calculated assuming that they can provide VI both by charging and by discharging at any time:

$$E_{BESS} = E_{BESS\_UP} + E_{BESS\_DN} \tag{8.10}$$

E_{BESS_UP} represents the capacity needed during the charging process and E_{BESS_DN} represents the capacity needed for the discharging process. As a consequence, the capacity of the batteries is given by:

$$E_{BESS} = 1.25 \cdot \left(\frac{P_{BESS0,N}}{\eta_d} + \eta_c \cdot P_{BESS0,N} \right) \cdot t_{IR} \tag{8.11}$$

where t_{IR} represents the time for the synthetic inertia service. This time can be assumed between 1 and 30 s, according to the pilot project Fast Reserve Units promoted by Terna in Italy. The coefficient 1.25 is considered to consider the rise and decrease the time of the power injection/demand from the BESS.

Following the above procedure, the BESS size is calculated for maximum renewable production in Case_2 (the same value is obtained for Case_1 being in both cases $H_{sys,min}$=0s), assuming H_{target}=2.64s, H_{BESS} variable between 5 and 20s and A_{Ntot}=2.9 MVA (including RES).

Table 8.7. BESS size for various operative hypotheses.

		E_{BESS} [kWh]					
H_{BESS} [s]	$P_{BESS0,N}$ [MW]	t_{IR} [s]					
		1	2	5	10	20	30
5	3.24	2.26	4.51	11.28	22.56	45.12	67.67
7	1.76	1.22	2.44	6.11	12.21	24.42	36.63
10	1.04	0.72	1.45	3.62	7.23	14.47	21.70
12	0.82	0.57	1.14	2.84	5.69	11.38	17.06
15	0.62	0.43	0.86	2.15	4.31	8.61	12.92
18	0.50	0.35	0.69	1.73	3.47	6.93	10.40
20	0.44	0.31	0.61	1.53	3.07	6.13	9.20
25	0.34	0.24	0.48	1.19	2.38	4.76	7.14

The values in Table 8.7 are very low, due to the short time of the VI service.
Another way for calculating the capacity of the BESS unit of Table 8.7 is to refer to the criterion used in the Fast Reserve Unit (FRU) program promoted by Terna.
In this case, the BESS charging/discharging curve must be represented in Figure 8.14 and the capacity, evaluated according to Figure 8.14 and considering about three interventions per day (1000 interventions in one year) must be reported in Table 8.8.

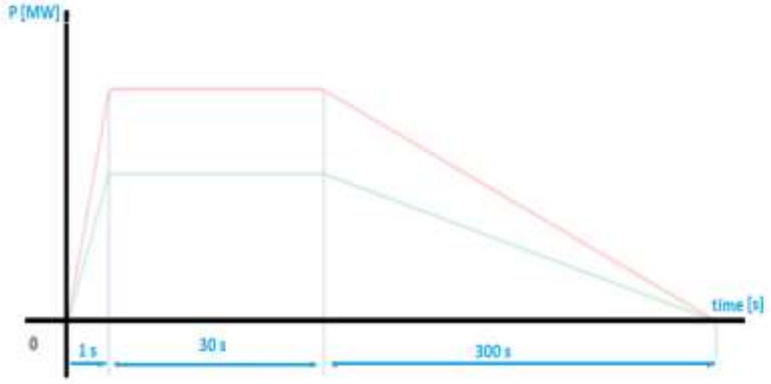

Figure 8.14. Charging/discharging curve of BESS for FCR according to the FRU program.

Table 8.8. BESS size as FRU.

H_{BESS} [s]	$P_{BESS0,N}$ [MW]	E_{BESS} [kWh]
5	3.24	1220
7	1.76	663
10	1.04	392
12	0.82	309
15	0.62	233
18	0.50	188
20	0.44	166
25	0.34	128

The values reported in Table 8.8 show that the BESS capacity is still deficient, assuming the same behaviour of a FRU.

8.3.4. Considerations about sizing and cost of BESS

This section shows a comparison of the results obtained in this chapter, with those obtained in a previous study on Pantelleria [135], with particular reference to the BESS sizing and cost. In [135] the authors carried out a multi-objective optimisation algorithm aiming to minimise the energy losses into the distribution grid of Pantelleria, the total electricity generation cost and the greenhouse gas emissions, for the Pantelleria distribution grid.

In [135], the selection of ESS sizing and the suitable BESS installation nodes was made according to different design strategies, aiming to compensate the variability of power production from PV plants (ST-PV strategy), to improve the voltage profile (ST-PV strategy) and to compensate the variations of large loads (ST-LO strategy). In order to consider realistic conditions, only four batteries were assumed to be installed in four different nodes of the MV grid, for a total capacity of 5.2 MWh and rated power 2.6 MW. Although design strategies are different compared to those considered in this Chapter, the BESS sizing developed in [135] can be used to verify concrete feasibility of BESS installation in Pantelleria island. The BESS capacity values reported in Tables 8.7 and 8.8 are compatible in power with those found in [135] for almost all system inertia values (except 5s) and always compatible in capacity.

Indeed, the capacity necessary for virtual inertia is always very low, considering the short time of the service. In the hypothesis that the service can be required one time per each hour of the day (an hypothesis clearly on the side of safety), the values in Table 8.7 can be increased as reported in Table 8.9. Also, under this hypothesis, the capacity obtained is still compatible with those reported in [135].

This means that the VI service could be provided by BESS installed for other applications without compromising the original function of these systems.

The investment cost for stationary batteries shown in Table 8.3 (200 €/kWh) can be considered a reasonable compromise among the different existing technologies, also taking into account the enormous potential of battery cost reduction according to the International Renewable Energy Agency (IRENA) [136]. Indeed, IRENA confirms that total installed costs for stationary batteries could fall between 50% and 60% by 2030 (the battery cell costs even more), main thanks to manufacturing facilities optimisation efforts, combined with better combinations and reduced use of materials. With specific reference to Lithium-ion batteries, which currently represents the most promising stationary battery technology, IRENA expects that the costs for stationary applications could fall below 200 $/kWh by 2030 for installed systems.

Table 8.9. BESS size for various operative hypothesis (one intervention per hour).

		E_{BESS} [kWh]					
H_{BESS} [s]	$P_{BESS0,N}$ [MW]	t_{IR} [s]					
		1	2	5	10	20	30
5	3.24	54.24	108.24	270.72	541.44	1082.88	1624.08
7	1.76	29.28	58.56	146.64	293.04	586.08	879.12
10	1.04	17.28	34.8	86.88	173.52	347.28	520.8
12	0.82	13.68	27.36	68.16	136.56	273.12	409.44
15	0.62	10.32	20.64	51.6	103.44	206.64	310.08
18	0.50	8.4	16.56	41.52	83.28	166.32	249.6
20	0.44	7.44	14.64	36.72	73.68	147.12	220.8
25	0.34	5.76	11.52	28.56	57.12	114.24	171.36

8.4.Conclusion

A second mathematical model has been introduced in this Chapter to investigate a feasible energy mix to supply small islands, considering BESS for avoiding electricity production curtailment. From the environmental point of view, the installation of RES-based generators produces a total electricity production of 25544 MWh/year, limiting the electricity production from diesel generators to 10924 MWh/y, consequently with a reduction of 70% for fuel consumption and CO_2 emissions in the island.

Nevertheless, the rotational inertia of the system is seriously compromised, and this led to excessive frequency deviations during power imbalances that must be solved using suitable methods like the provision of synthetic inertia by BESS suitably sized to provide, in the worst operative condition, the desired value of VI also more times per day.

The installation cost of such systems is always becoming more and more sustainable and, for this reason, it is realistic foreseeing that, together with RES interfaced by VSC to the grid, they can be used as a solution for allowing a high penetration of RES generators in small islands weak grids.

Chapter 9

Conclusion

The study presented in this thesis demonstrates the importance of facing the issue of the penetration of high shares of renewables in isolated small and weak grids.
Indeed, while on one hand it is universally recognized the need for a transition from fuel-based grids towards smart and green grids, on the other hand, many of the studies in the scientific literature only face classical problems such as minimization of the costs for the transitions and optimal placement of the distributed generation in the grid in order to minimize voltage drops, but they do not deal with the issue of frequency stabilities in such systems.

Focusing on two real case studies (Lampedusa and Pantelleria), in this thesis the risk of blackout (or grid collapse) due to the reduction (or totally loss) of rotational inertia, caused by the introduction of high shares of VSC-based photovoltaic and wind generators, has been shown.

The thesis has also presented suitable solutions to the problem:

- use of two algorithms by LCoE to evaluate sizing of the energy mix:
- use of VSC controlled by VSM+CCC strategies (eventually improved with grid impedance and load impedance estimation methods), able to compensate load/generation variation in a fast and effective way and to maintain the voltage at the PCC during a fault;
- use of BESS sized and controlled to provide virtual inertia.

On the first point, the algorithm of Chapter 5 solicits the need of proposing suitable solutions for supporting the penetration of RES not able to provide a natural inertial response to disturbances of the system. In this context, a second algorithm from Chapter 8 proposes a methodology for sizing battery energy storage systems (BESS) able to provide synthetic inertia in replacement of the missing rotational inertia of the diesel generators.

On the second point, it must be noted how important is a correct tuning process of the control parameters that can be done only simulating the response of the VSC in various conditions and knowing the parameters of the grid at the PCC. In particular, it is possible to implement a suitable algorithm for sizing the damping factor as a function of the other parameters of the controller and the grid. A very influencing parameter is the Short Circuit Ratio at the PCC, from which it depends on the response of the VSC during normal operation and in the case of a fault.
The research on the control of static converter is currently in process and what has been presented in this thesis represents the current state of the art on the topic. Nevertheless, improvements on the control structures can still be done, especially for managing VSC with VSM control in unbalanced load.

On the thrid point, it must be underlined how the most recent trend by Transmission System Operators worldwide is to use storage for providing virtual inertia and fast frequency response.

In this thesis, two strategies have been adopted for sizing the storage capacity to be installed for this purpose. In both cases, the amount of energy for providing the VI service is very low concerning the classical size of a BESS for energy-intensive applications.

It is possible also to use the same storage for FCR, but in this case, the capacity of the storage must be considerably increased, and such an application is not realistic in small islands where utilities always maintain some SG as reserve group in the case the groups in operation experience faults.

In conclusion, the simulation results of the thesis give some precious indications for driving the next moves of the transition of small islands towards smart and renewable islands, and they can be considered as a first step for promoting the research on VSC applications in weak and isolated grids. Indeed, small islands are only an example of such grids that, currently, can be found in many central areas of the mainland (rural areas) and in developing countries where small-sized diesel generator are the standard way for producing electricity for small communities.

References

[1] M. Meleddu and M. Pulina, “Public spending on renewable energy in Italian regions,” *Renew. Energy*, vol. 115, pp. 1086–1098, Jan. 2018.

[2] L. I. Fuldauer, M. C. Ives, D. Adshead, S. Thacker, and J. W. Hall, “Participatory planning of the future of waste management in small island developing states to deliver on the Sustainable Development Goals,” *J. Clean. Prod.*, vol. 223, pp. 147–162, Jun. 2019.

[3] L. P. Joseph and R. Prasad, “Assessing the sustainable municipal solid waste (MSW) to electricity generation potentials in selected Pacific Small Island Developing States (PSIDS),” *J. Clean. Prod.*, vol. 248, p. 119222, Mar. 2020.

[4] “Renewable Power Generation Costs in 2017,” */publications/2018/Jan/Renewable-power-generation-costs-in-2017*, Accessed: Dec. 27, 2020.

[5] A. M. Kutan, S. R. Paramati, M. Ummalla, and A. Zakari, “Financing Renewable Energy Projects in Major Emerging Market Economies: Evidence in the Perspective of Sustainable Economic Development,” *Emerg. Mark. Financ. Trade*, vol. 54, no. 8, pp. 1762–1778, 2018.

[6] G. Cannistraro, M. Cannistraro, and G. Trovato, “Islands ‘Smart Energy’ for eco-sustainable energy a case study ‘Favignana Island,’” *Int. J. Heat Technol.*, vol. 35, no. Special Issue1, pp. S87–S95, Sep. 2017.

[7] J. Liu, C. Mei, H. Wang, W. Shao, and C. Xiang, “Powering an island system by renewable energy—A feasibility analysis in the Maldives,” *Energy*, vol. 227, no. August, pp. 18–27, Oct. 2018.

[8] P. Blechinger, R. Seguin, C. Cader, P. Bertheau, and C. Breyer, “Assessment of the global potential for renewable energy storage systems on small islands,” *Energy Procedia*, vol. 46, pp. 294–300, 2014.

[9] M. Majidi Nezhad, D. Groppi, F. Rosa, G. Piras, F. Cumo, and D. A. Garcia, “Nearshore wave energy converters comparison and Mediterranean small island grid integration,” *Sustain. Energy Technol. Assessments*, vol. 30, no. July, pp. 68–76, 2018.

[10] M. Majidi Nezhad *et al.*, “Wind energy potential analysis using Sentinel-1 satellite: A review and a case study on Mediterranean islands,” *Renew. Sustain. Energy Rev.*, vol. 109, no. December 2018, pp. 499–513, 2019.

[11] E. Zafeiratou and C. Spataru, “Sustainable island power system – Scenario analysis for Crete under the energy trilemma index,” *Sustain. Cities Soc.*, vol. 41, no. April, pp. 378–391, 2018.

[12] H. M. Marczinkowski and P. A. Østergaard, “Evaluation of electricity storage versus thermal storage as part of two different energy planning approaches for the islands Samsø and Orkney,” *Energy*, vol. 175, pp. 505–514, May 2019.

[13] D. Al Katsaprakakis, B. Thomsen, I. Dakanali, and K. Tzirakis, “Faroe Islands: Towards 100% R.E.S. penetration,” *Renew. Energy*, vol. 135, no. 2019, pp. 473–484, May 2019.

[14] J. Mendoza-Vizcaino, A. Sumper, A. Sudria-Andreu, and J. M. Ramirez, “Renewable technologies for generation systems in islands and their application to Cozumel Island, Mexico,” *Renew. Sustain. Energy Rev.*, vol. 64, pp. 348–361, 2016.

[15] H. C. Gils and S. Simon, “Carbon neutral archipelago – 100% renewable energy supply for the Canary Islands,” *Appl. Energy*, vol. 188, pp. 342–355, Feb. 2017.

[16] E. Rusu, “Evaluation of the Wave Energy Conversion Efficiency in Various Coastal Environments,” *Energies*, vol. 7, no. 6, pp. 4002–4018, Jun. 2014.

[17] P. Stenzel, A. Schreiber, J. Marx, C. Wulf, M. Schreieder, and L. Stephan, “Renewable energies for Graciosa Island, Azores-Life Cycle Assessment of electricity generation,” *Energy Procedia*, vol. 135, pp. 62–74, 2017.

[18] M. Alves, R. Segurado, and M. Costa, “Increasing the penetration of renewable energy sources in isolated islands through the interconnection of their power systems. The case of Pico and Faial islands, Azores,” *Energy*, vol. 182, pp. 502–510, Sep. 2019.

[19] S. Selosse, S. Garabedian, O. Ricci, and N. Maïzi, “The renewable energy revolution of

reunion island," *Renew. Sustain. Energy Rev.*, vol. 89, no. March, pp. 99–105, 2018.

[20] G. Notton, "Importance of islands in renewable energy production and storage: The situation of the French islands," *Renew. Sustain. Energy Rev.*, vol. 47, pp. 260–269, 2015.

[21] I. Kougias, S. Szabó, A. Nikitas, and N. Theodossiou, "Sustainable energy modelling of non-interconnected Mediterranean islands," *Renew. Energy*, vol. 133, pp. 930–940, Apr. 2019.

[22] C. Bueno and J. A. Carta, "Wind powered pumped hydro storage systems, a means of increasing the penetration of renewable energy in the Canary Islands," *Renew. Sustain. Energy Rev.*, vol. 10, no. 4, pp. 312–340, Aug. 2006.

[23] S. Bozzi, R. Archetti, and G. Passoni, "Wave electricity production in Italian offshore: A preliminary investigation," *Renew. Energy*, vol. 62, pp. 407–416, 2014.

[24] M. Monteforte, C. Lo Re, and G. B. B. Ferreri, "Wave energy assessment in Sicily (Italy)," *Renew. Energy*, vol. 78, no. August, pp. 276–287, Jun. 2015.

[25] G. Lavidas and V. Venugopal, "A 35 year high-resolution wave atlas for nearshore energy production and economics at the Aegean Sea," *Renew. Energy*, vol. 103, pp. 401–417, Apr. 2017.

[26] J. P. Sierra, C. Mösso, and D. González-Marco, "Wave energy resource assessment in Menorca (Spain)," *Renew. Energy*, vol. 71, pp. 51–60, 2014.

[27] E. Rusu and C. Guedes Soares, "Coastal impact induced by a Pelamis wave farm operating in the Portuguese nearshore," *Renew. Energy*, vol. 58, pp. 34–49, Oct. 2013.

[28] Ministero dello Sviluppo Economico, *Decreto 14 febbraio 2017. Disposizioni per la progressiva copertura del fabbisogno delle isole minori non interconnesse attraverso energia da fonti rinnovabili.* 2017.

[29] Italian Ministry of the Environment and for Protection of the Land and Sea, *Decree n. 340 14/07/2017. Measures of energy efficiency, sustainable mobility and adaptaion to climate changes in small islands (in Italian "Decreto n. 340 del 14 Luglio 2017. Interventi di efficienza energetica, mobilità sostenibile e adattamento agli im*. Italy, 2017.

[30] J. Zhang and Y. Zheng, "The flexibility pathways for integrating renewable energy into China's coal dominated power system: The case of Beijing-Tianjin-Hebei Region," *J. Clean. Prod.*, vol. 245, p. 118925, 2019.

[31] L. de Santoli, F. Mancini, and D. Astiaso Garcia, "A GIS-based model to assess electric energy consumptions and usable renewable energy potential in Lazio region at municipality scale," *Sustain. Cities Soc.*, vol. 46, p. 101413, Apr. 2019.

[32] "Stability definitions and characterization of dynamic behavior in systems with high penetration of power electronic interfaced technologies." https://resourcecenter.ieee-pes.org/publications/technical-reports/PES_TP_TR77_PSDP_stability_051320.html (accessed Dec. 27, 2020).

[33] E. Ørum *et al.*, "Future system inertia" Accessed: Dec. 11, 2020. [Online]. Available: www.entsoe.eu.

[34] D. Stanelyte and V. Radziukynas, "Review of Voltage and Reactive Power Control Algorithms in Electrical Distribution Networks," *Energies*, vol. 13, no. 1, p. 58, Dec. 2019.

[35] "H2020 Migrate." https://www.h2020-migrate.eu/downloads.html (accessed Dec. 27, 2020).

[36] B. M. Favuzza S, Ippolito G, Musca R, Navarro Navia M, Riva Sanseverino E, Zizzo G, "An Analysis of the Inertial Response of Small Isolated Power Systems in the presence of Generation from Renewable Energy Sources," Dec. 11, 2020.

[37] "Limited frequency sensitive mode ENTSO-E guidance document for national implementation for network codes on grid connection," 2017.

[38] R. Bugdal, A. Dysko, G. Burt, and J. Mcdonald, "Performance analysis of the ROCOF and vector shift methods using a dynamic protection modeling approach," *undefined*, 2006.

[39] "Rate of Change of Frequency (RoCoF) withstand capability ENTSO-E guidance document for national implementation for network codes on grid connection," Dec. 11, 2020.

[40] A. Ulbig, T. S. Borsche, and G. Andersson, "Impact of Low Rotational Inertia on Power

System Stability and Operation." *IFAC Proceedings*,2014

[41] S. C. Johnson, D. J. Papageorgiou, D. S. Mallapragada, T. A. Deetjen, J. D. Rhodes, and M. E. Webber, "Evaluating rotational inertia as a component of grid reliability with high penetrations of variable renewable energy," *Energy*, vol. 180, pp. 258–271, Aug. 2019.

[42] J. Schiffer, P. Aristidou, and R. Ortega, "Online Estimation of Power System Inertia Using Dynamic Regressor Extension and Mixing" *IEEE Transactions on Power Systems*, 2019.

[43] M. Persson, Thesis for the Degree of Doctor of Philosophy Frequency Response by Wind Farms in Power Systems with High Wind Power Penetration, 2017.

[44] "IEEE 1547-2018 - IEEE Standard for Interconnection and Interoperability of Distributed Energy Resources with Associated Electric Power Systems Interfaces." .

[45] B. Wen, D. Boroyevich, P. Mattavelli, Z. Shen, and R. Burgos, "Influence of phase-locked loop on input admittance of three-phase voltage-source converters," in *Conference Proceedings - IEEE Applied Power Electronics Conference and Exposition - APEC*, 2013, pp. 897–904.

[46] S. Gao and M. Barnes, "Phase-locked loops for grid-tied inverters: Comparison and testing," in *IET Conference Publications*, 2016, vol. 2016, no. CP684.

[47] Y. Zhou, Z. Miao, Y. Li, and L. Fan, "Design Robust Cascade Control Structure for Voltage Source Converters," Nov. 2017.

[48] J. A. Sa'ed, D. Curto, S. Favuzza, R. Musca, M. N. Navia, and G. Zizzo, "A Simulation Analysis of VSM Control for RES plants in a Small Mediterranean Island," Jun. 2020.

[49] S. D'Arco, J. A. Suul, and O. B. Fosso, "Automatic Tuning of Cascaded Controllers for Power Converters Using Eigenvalue Parametric Sensitivities," *IEEE Trans. Ind. Appl.*, vol. 51, no. 2, pp. 1743–1753, Mar. 2015.

[50] F. B. Del Blanco, M. W. Degner, and R. D. Lorenz, "Dynamic analysis of current regulators for ac motors using complex vectors," *IEEE Trans. Ind. Appl.*, vol. 35, no. 6, p. 14241432, 1999.

[51] C. Arghir, T. Jouini, and F. Dörfler, "Grid-forming control for power converters based on matching of synchronous machines," *Automatica*, vol. 95, pp. 273–282, Sep. 2018.

[52] B. Favuzza S, Bongiorno M, Musca R, Navarro Navia M, Riva Sanseverino E, Zizzo G, "Isolated Power System Dominated by Renewable Energy Sources with VSM-Structure," *ICEEPE 2020*, 2020.

[53] L. Zhang, L. Harnefors, and H. P. Nee, "Power-synchronization control of grid-connected voltage-source converters," *IEEE Trans. Power Syst.*, vol. 25, no. 2, pp. 809–820, May 2010.

[54] B. Bouaziz and F. Bacha, "Direct power control of grid-connected converters using sliding mode controller," 2013, doi: 10.1109/ICEESA.2013.6578497.

[55] N. Muangruk and S. Nungam, "Direct Power Control of Three-phase Voltage Source Converters Using Feedback Linearization Technique," in *Procedia Computer Science*, Jan. 2016, vol. 86, pp. 365–368.

[56] "Renewable Energy Integration | PSCAD." https://www.pscad.com/engineering-services/renewable-energy-integration (accessed Dec. 27, 2020).

[57] Q. C. Zhong and G. Weiss, "Synchronverters: Inverters that mimic synchronous generators," *IEEE Trans. Ind. Electron.*, vol. 58, no. 4, pp. 1259–1267, Apr. 2011.

[58] Y. Chen, R. Hesse, D. Turschner, and H. P. Beck, "Dynamic properties of the virtual synchronous machine (VISMA)," *Renew. Energy Power Qual. J.*, vol. 1, no. 9, pp. 755–759, May 2011.

[59] M. Abdollahi, J. I. Candela, J. Rocabert, R. S. M. Aguilar, and J. R. Hermoso, "Synchronous power controller merits for dynamic stability improvement in long line by renewables," in *2016 IEEE International Conference on Renewable Energy Research and Applications, ICRERA 2016*, Mar. 2017, pp. 760–765.

[60] T. Jouini, E. Tegling, and Z. Sun, "Grid-forming lambda-omega virtual oscillator control in converter-based power systems," Dec. 2020, Accessed: Dec. 27, 2020.

[61] "Norme CEI 0-16 e 0-21." https://www.ceinorme.it/it/norme-cei-0-16-e-0-21.html (accessed Dec. 18, 2020).

[62] "Partecipazione alla Regolazione di Frequenza" 2008. Accessed: Dec. 18, 2020. [Online].

Available: www.ucte.org.

[63] B. Porretta and S. Porretta, “Calculation of power systems inertia and frequency response,” in *2018 IEEE Texas Power and Energy Conference, TPEC 2018*, 2018.

[64] F. L. Heather Wyman-Pain, Yuankai Bian, “Changes in Frequency Events and the Frequency Response Markets in Great Britain,” 2018, Accessed: Dec. 11, 2020.

[65] E. Ørum *et al.*, “Future System Inertia 2” Accessed: Dec. 11, 2020. [Online]. Available: www.entsoe.eu.

[66] T. Kerdphol, F. Saifur Rahman, and Y. Mitani, “Virtual Inertia Control Application to Enhance Frequency Stability of Interconnected Power Systems with High Renewable Energy Penetration,”2016.

[67] T. H. Mohamed, H. Bevrani, A. A. Hassan, and T. Hiyama, “Decentralized model predictive based load frequency control in an interconnected power system,” *Energy Convers. Manag.*, vol. 52, no. 2, pp. 1208–1214, 2011.

[68] Kundur Prabha, *Power System Stability and Control: Kundur, Prabha: 8601400847930: Amazon.com: Books*. .

[69] E. Rakhshani, D. Gusain, V. Sewdien, J. L. Rueda Torres, and M. A. M. M. Van Der Meijden, “A Key Performance Indicator to Assess the Frequency Stability of Wind Generation Dominated Power System,” *IEEE Access*, vol. 7, pp. 130957–130969, 2019.

[70] R. : A. Berizzi, “Analisi della Metodologia per la Remunerazione del Servizio di Regolazione del Servizio di Regolazione Primaria di Frequenza,” Apr. 2015, Accessed: Dec. 11, 2020. [Online]. Available: https://www.politesi.polimi.it/handle/10589/106962.

[71] “Regione Siciliana Assessorato Beni Culturali, Ambientali e Pubblica Istruzione.” http://www.regione.sicilia.it/beniculturali/dirbenicult/bca/ptpr/Piano Pantelleria completo.pdf, accessed on 04th September 2019.

[72] “S.med.e. Pantelleria S.p.A.” https://smedepantelleria.wordpress.com/ (accessed Dec. 11, 2020).

[73] V. Cosentino *et al.*, “Smart renewable generation for an islanded system. Technical and economic issues of future scenarios,” *Energy*, vol. 39, no. 1, pp. 196–204, Mar. 2012.

[74] D. Curto, V. Franzitta, S. Longo, F. Montana, E. R. Sanseverino, and E. Telaretti, “Flexibility Services in a Mediterranean Small Island to Minimize Costs and Emissions Related to Electricity Production from Fossil Fuels,” in *20th IEEE Mediterranean Electrotechnical Conference, MELECON 2020 - Proceedings*, Jun. 2020.

[75] M. Altin, R. Teodorescu, B. B. Jensen, U. D. Annakkage, F. Iov, and P. C. Kjaer, “Methodology for assessment of inertial response from wind power plants,” 2012.

[76] P. Wall, “Smart frequency control for the future Gb power system,” Jul. 2016.

[77] V. Knap, S. K. Chaudhary, D. I. Stroe, M. Swierczynski, B. I. Craciun, and R. Teodorescu, “Sizing of an energy storage system for grid inertial response and primary frequency reserve,” *IEEE Trans. Power Syst.*, vol. 31, no. 5, pp. 3447–3456, 2016.

[78] H. T. Nguyen, G. Yang, A. H. Nielsen, and P. H. Jensen, “Frequency stability enhancement for low inertia systems using synthetic inertia of wind power,” in *IEEE Power and Energy Society General Meeting*, Jan. 2018.

[79] Z. Z. Zhenxiong Wang, Fang Zhuo, Jiaqi Wu, Hao Yi, Hao Zhai, “Inertia time constant design in microgrids with multiple paralleled virtual synchronous generators,” Accessed: Dec. 11, 2020.

[80] K. Branker, M. J. M. Pathak, and J. M. Pearce, “A review of solar photovoltaic levelized cost of electricity,” *Renewable and Sustainable Energy Reviews*, vol. 15, no. 9. Pergamon, pp. 4470–4482, Dec. 01, 2011.

[81] E. González-Roubaud, D. Pérez-Osorio, and C. Prieto, “Review of commercial thermal energy storage in concentrated solar power plants: Steam vs. molten salts,” *Renewable and Sustainable Energy Reviews*, vol. 80. Elsevier Ltd, pp. 133–148, Dec. 01, 2017.

[82] W. Short, D. J. Packey, and T. Holt, “A manual for the economic evaluation of energy efficiency and renewable energy technologies,” Golden, CO, Mar. 1995.

[83] “Renewable Energy and Jobs – Annual Review 2020,” */publications/2020/Sep/Renewable-Energy-and-Jobs-Annual-Review-2020*, Accessed: Dec. 11, 2020. [Online]. Available: /publications/2020/Sep/Renewable-Energy-and-Jobs-

Annual-Review-2020.

[84] "Ministero dello Sviluppo Economico | www.governo.it." http://www.governo.it/it/ministeri/ministero-dello-sviluppo-economico (accessed Dec. 11, 2020).

[85] "Hummer H25.0-60KW - 60,00 kW - Wind turbine." https://en.wind-turbine-models.com/turbines/1683-hummer-h25.0-60kw (accessed Dec. 11, 2020).

[86] G. Emmanouil, G. Galanis, C. Kalogeri, G. Zodiatis, and G. Kallos, "10-year high resolution study of wind, sea waves and wave energy assessment in the Greek offshore areas," *Renew. Energy*, vol. 90, pp. 399–419, May 2016.

[87] L. H. Holthuijsen, "Waves in Oceanic and Coastal Waters."

[88] V. Franzitta, P. Catrini, and D. Curto, "Wave Energy Assessment along Sicilian Coastline, Based on DEIM Point Absorber," *Energies*, vol. 10, no. 3, p. 376, Mar. 2017.

[89] "Climate Palermo - meteoblue."https://www.meteoblue.com/en/weather/historyclimate/climatemodelled/palermo_italy_2523920 (accessed Dec. 11, 2020).

[90] "Photovoltaic Geographical Information System (PVGIS) | EU Science Hub." https://ec.europa.eu/jrc/en/pvgis (accessed Dec. 11, 2020).

[91] "mercato elettrico." http://www.mercatoelettrico.org/It/download/DatiStorici.aspx (accessed 2.20.19). (accessed Dec. 11, 2020).

[92] "ARERA - Determinazione dell'aliquota di integrazione tariffaria, per l'anno 2015, per l'impresa elettrica minore non trasferita all'Enel S.p.a., Selis Lampedusa S.p.a." https://www.arera.it/it/docs/18/508-18.htm (accessed Dec. 11, 2020).

[93] "Renewable Power Generation Costs in 2017," */publications/2018/Jan/Renewable-power-generation-costs-in-2017*, Accessed: Dec. 11, 2020. [Online]. Available: /publications/2018/Jan/Renewable-power-generation-costs-in-2017.

[94] V. Franzitta, D. Curto, and D. Rao, "Energetic Sustainability Using Renewable Energies in the Mediterranean Sea," *Sustainability*, vol. 8, no. 11, p. 1164, Nov. 2016.

[95] G. M. Caporale and L. A. Gil-Alana, "Long-term interest rates in Europe: A fractional cointegration analysis," *Int. Rev. Econ. Financ.*, vol. 61, no. January, pp. 170–178, 2019.

[96] E. Bargiacchi, S. Frigo, and G. Spazzafumo, "Energetic and exergetic analysis of an innovative plant for the production of electricity and substitute natural gas," in *Energy Procedia*, Aug. 2018.

[97] Advanced Flow, "Energy Recovery Device," 2015. .

[98] N. N. M. and Z. G. Curto D, Favuzza S, Musca R, "Control Structures Implementation to Allow High Penetration of a VSC within an Isolated Power System," ICEEPE, 2020.

[99] I. Kaya and M. Nalbantoglu, "Cascade controller design using controller synthesis," in *2015 19th International Conference on System Theory, Control and Computing, ICSTCC 2015 - Joint Conference SINTES 19, SACCS 15, SIMSIS 19*, Nov. 2015, pp. 32–36.

[100] "Process Dynamics and Control, 4th Edition | Wiley." https://www.wiley.com/en-us/Process+Dynamics+and+Control%2C+4th+Edition-p-9781119285915 (accessed Dec. 17, 2020).

[101] A. A. Jamshidifar and D. Jovcic, "3-Level cascaded voltage source converters controller with dispatcher droop feedback for direct current transmission grids," *IET Gener. Transm. Distrib.*, vol. 9, no. 6, pp. 571–579, Apr. 2015.

[102] J. Wei, "Review of Current Control Strategies in Modular Multilevel Converter," *undefined*, 2016.

[103] L. Harnefors, L. Zhang, and M. Bongiorno, "Frequency-domain passivity-based current controller design," *IET Power Electron.*, vol. 1, no. 4, pp. 455–465, 2008.

[104] L. Harnefors and H. P. Nee, "Model-based current control of ac machines using the internal model control method," *IEEE Trans. Ind. Appl.*, vol. 34, no. 1, pp. 133–141, 1998.

[105] F. Guo, T. Zheng, and Z. Wang, "Comparative study of direct power control with vector control for rotor side converter of DFIG," in *IET Conference Publications*, 2012, vol. 2012, no. 616 CP.

[106] E. D. Dinu, D. Ilisiu, I. FĂgĂrĂşan, S. S. Iliescu, and N. Arghira, "Voltage-Reactive power control in renewables power plants: Technical requirements applied in the

Romanian power grid,” Jun. 2016, doi: 10.1109/AQTR.2016.7501330.

[107] J. Ögren, “PLL design for inverter grid connection Simulations for ideal and non-ideal grid conditions.” Accessed: Dec. 17, 2020.

[108] R. Desai, S. Patel, P. Patel, U. student, A. professor, and C. Gopalbhai Patel, “PLL based method for control of grid connected inverter for unbalanced grid frequency Electrical engineering department,” 2017.

[109] “Improved PLL for Power Generation Systems Operating under Real Grid Conditions.” https://www.researchgate.net/publication/259974458_Improved_PLL_for_Power_Generation_Systems_Operating_under_Real_Grid_Conditions, Dec. 17, 2020.

[110] S. D’Arco, J. A. Suul, and O. B. Fosso, “A Virtual Synchronous Machine implementation for distributed control of power converters in SmartGrids,” *Electr. Power Syst. Res.*, vol. 122, pp. 180–197, May 2015.

[111] M. Torres and L. A. C. Lopes, “A Virtual Synchronous Machine to Support Dynamic Frequency Control in a Mini-Grid That Operates in Frequency Droop Mode,” *Energy Power Eng.*, vol. 05, no. 03, pp. 259–265, 2013.

[112] and J. A. S. Olve Mo, Salvatore D’Arco, “Evaluation of Virtual Synchronous Machines With Dynamic or Quasi-Stationary Machine Models,” 2017, Accessed: Dec. 17, 2020.

[113] Q. C. Zhong, Z. Ma, W. L. Ming, and G. C. Konstantopoulos, “Grid-friendly wind power systems based on the synchronverter technology,” *Energy Convers. Manag.*, vol. 89, pp. 719–726, Jan. 2015.

[114] R. Sadikovic, P. Korba, and G. Andersson, “Application of FACTS devices for damping of power system oscillations,” 2005.

[115] “Control and Operation of a Grid with 100 % Converter-Based Devices.” https://www.h2020-migrate.eu/_Resources/Persistent/1bb0f89024e41a85bf94f1ec7ee6f8d7c34bc29a/D3.6 - Requirement guidelines for operating a grid with 100 power electronic devices.pdf, Dec. 17, 2020.

[116] S. D’Arco, J. A. Suul, and O. B. Fosso, “Control system tuning and stability analysis of Virtual Synchronous Machines,” in *2013 IEEE Energy Conversion Congress and Exposition, ECCE 2013*, 2013, pp. 2664–2671.

[117] M. Alexik, “Modelling of process control that have time delay: Verification of algorithms suitable for process control containing time delay by simulation,” in *UKSim2010 - UKSim 12th International Conference on Computer Modelling and Simulation*, 2010, pp. 221–226.

[118] A. Izadian and A. Izadian, “Introduction to Electric Circuits,” in *Fundamentals of Modern Electric Circuit Analysis and Filter Synthesis*, Springer International, 2019.

[119] A. Ghanem, M. Rashed, M. Sumner, M. A. El-Sayes, and I. I. I. Mansy, “Grid impedance estimation for islanding detection and adaptive control of converters,” in *IET Conference Publications*, 2016, vol. 2016, no. CP684.

[120] M. Ciobotaru, R. Teodorescu, P. Rodriguez, A. Timbus, and F. Blaabjerg, “Online grid impedance estimation for single-phase grid-connected systems using PQ variations,” in *PESC Record - IEEE Annual Power Electronics Specialists Conference*, 2007.

[121] B. Arif, L. Tarisciotti, P. Zanchetta, J. C. Clare, and M. Degano, “Grid Parameter Estimation Using Model Predictive Direct Power Control,” *IEEE Trans. Ind. Appl.*, vol. 51, no. 6, pp. 4614–4622, Nov. 2015.

[122] N. Ishigure, K. Matsui, and F. Ueda, “Development of an on-line impedance meter to measure the impedance of a distribution line,” in *IEEE International Symposium on Industrial Electronics*, 2001, vol. 1, pp. 549–554.

[123] D. Gil Rubio, “Utilization of grid information in controllerof grid-connected converters,” *Master Thesis*, 2019.

[124] S. Favuzza *et al.*, “An Analysis of the Intertial Response of Small Isolated Power Systems in Presence of Generation from Renewable Energy Sources,” in *2018 IEEE 4th International Forum on Research and Technology for Society and Industry (RTSI)*, Sep. 2018, vol. 2019, pp. 1–6.

[125] C. Agathokleous and J. Ehnberg, “A quantitative study on the requirement for additional

inertia in the european power system until 2050 and the potential role of wind power," *Energies*, vol. 13, no. 9, 2020.

[126] N. Sharma and S. Sankar, "Modeling and Control of Battery Energy Storage System for Providing Grid Support Services," *Clemson Univ. Power Syst. Conf. PSC 2018*, 2019, doi: 10.1109/PSC.2018.8664018.

[127] D. Curto, R. Musca, S. Favuzza, M. Navia Navarro, and G. Zizzo, "Control Structures Implementation to Allow High Penetration of a VSC within an Isolated Power System," ICEEPE 2020, 2020.

[128] EU SCIENCE HUB, "Photovoltaic Geographical Information System (PVGIS)," 2020. .

[129] International Electrotechnical Commission (IEC), *IEC 61400-1. Wind energy generation systems. Part 1: Design requirements*. 2019.

[130] G. Besio, L. Mentaschi, and A. Mazzino, "Wave energy resource assessment in the Mediterranean Sea on the basis of a 35-year hindcast," *Energy*, vol. 94, pp. 50–63, Jan. 2016.

[131] ISPRA, "Mazara del Vallo Buoy (RON 2009)." .

[132] V. Franzitta and D. Curto, "Sustainability of the Renewable Energy Extraction Close to the Mediterranean Islands," *Energies*, vol. 10, no. 4, p. 283, Feb. 2017.

[133] IEA, "World Energy Investment 2019," 2019.

[134] Italian Ministry of Economic Development, "Monthly fuel prices," 2019. .

[135] M. G. Ippolito, M. L. Di Silvestre, E. Riva Sanseverino, G. Zizzo, and G. Graditi, "Multi-objective optimized management of electrical energy storage systems in an islanded network with renewable energy sources under different design scenarios," *Energy*, vol. 64, pp. 648–662, Jan. 2014.

[136] IRENA, *Electricity storage and renewables: Costs and markets to 2030*, no. October. 2017.

Appendix A

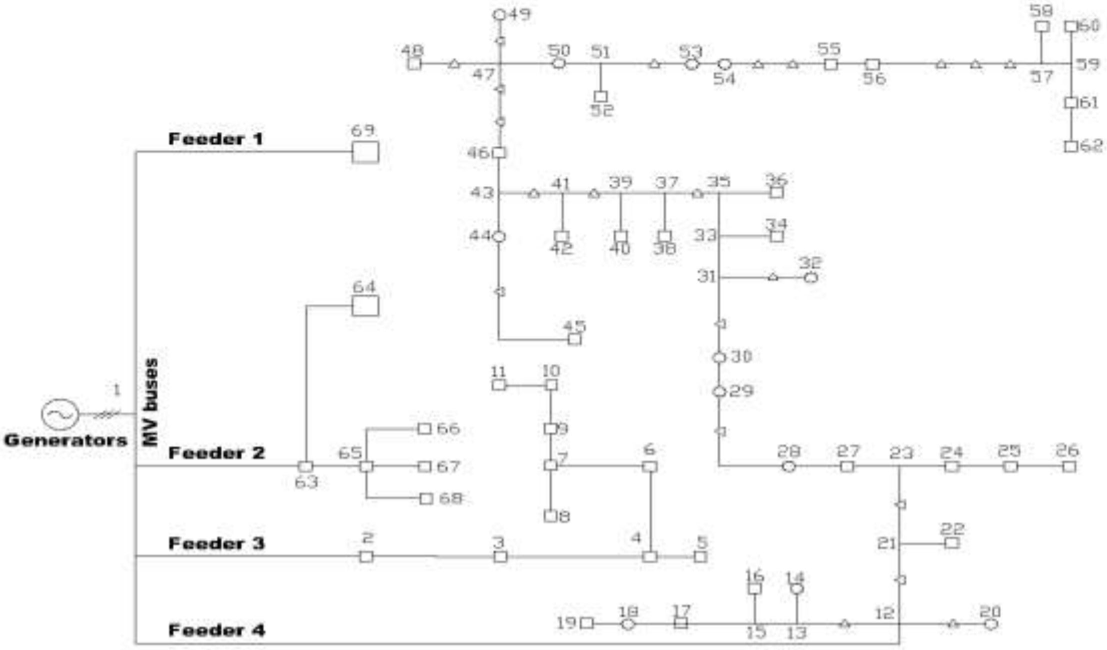

Figure A1: Layout of the medium voltage grid of Lampedusa.

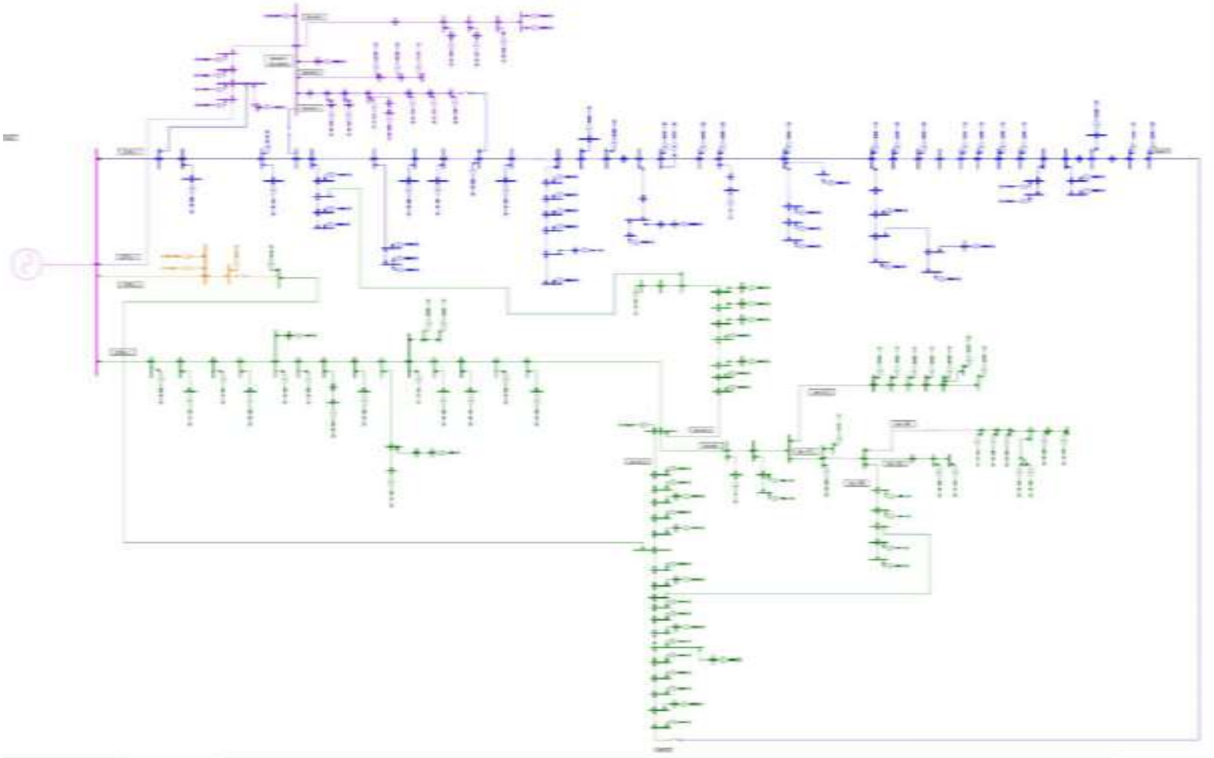

Figure A2: Layout of the medium voltage grid of Pantelleria.

Appendix B

Table B.1. Values of main economic parameters Lampedusa.

Parameters	Symbols	Values
Annual energy demand	E_d	36863 MWh/year
Electricity cost by diesel engines	c_f	0.205 €/kWh
Inflation rate for energy	ε	2.99%
Monetary interest rate	τ	1.14%
Unitary cost to install 1 kW of PVP	$c_{pv,0}$	1231 €/kW
Unitary cost to install 1 kW of wind turbines	$c_{w,0}$	1310 €/kW
Unitary cost to install 1 kW of sea wave	$c_{sw,0}$	5020 €/kW
Unitary O&M cost for 1 kW of PVP	$c_{pv,A}$	18 €/kW-year
Unitary O&M cost for 1 kW of wind turbines	$c_{w,A}$	50 €/kW-year
Unitary O&M cost for 1 kW of WEC	$c_{sw,A}$	75 €/kW-year
Annual O&M cost of diesel engines	$C_{f,A}$	2,830,659 €/year
Equivalent working hours of PVP	$h_{e,pv}$	1953.2 h/year
Equivalent working hours of wind	$h_{e,w}$	4982.6 h/year
Equivalent working hours of sea wave	$h_{e,sw}$	2419.5 h/year